INTERDISCIPLINARY MATERIALS SCIENCE

ABERRATION-CORRECTED ATOMIC NUMBER CONTRAST SCANNING TRANSMISSION ELECTRION MICROSCOPY OF NANOCRYSTALS AND NANOMATERIAL-BASED SYSTEMS FOR USE IN NEXT-GENERATION PHOTOVOLTAIC DEVICES

TONY L. WATT

Thesis under the direction of Professor Sandra J. Rosenthal

To support the world's insatiable desire for energy in the coming century without risking environmental catastrophe, paradigm-shifting research into next-generation photovoltaics and solid-state white lighting is necessary. The Rosenthal group has been pursuing a fully solid-state, inorganic nanostructured photovoltaic featuring pyrolytically synthesized semiconductor nanocrystals deposited within a mesoporous nanocrystalline anatase (meso-nc-TiO_2) framework. The synthesis and characterization of meso-nc-TiO_2 pores and nanotubes with deposited nanocrystals represents a significant milestone in the fabrication of our next-generation photovoltaic devices. Additionally, a variety of nanocrystal systems were imaged using aberration-corrected atomic number contrast scanning transmission electron microscopes (Z-STEM). Most significantly, the first ever Z-STEM images of ultra-small white-light emitting CdSe nanocrystals were collected, which will aid in the development of a solid-state white-light source.

Approved_____Date_____

ABERRATION-CORRECTED ATOMIC NUMBER CONTRAST SCANNING TRANSMISSION ELECTRION MICROSCOPY OF NANOCRYSTALS AND NANOMATERIAL-BASED SYSTEMS FOR USE IN NEXT-GENERATION PHOTOVOLTAIC DEVICES

By

Tony L. Watt

Thesis

Submitted to the Faculty of the

Graduate School of Vanderbilt University

in partial fulfillment of the requirements

for the degree of

MASTER OF SCIENCE

in

Interdisciplinary Materials Science

August, 2008

Nashville, Tennessee

Approved:

Professor Sandra J. Rosenthal

Professor James E. Wittig

TABLE OF CONTENTS

LIST OF FIGURES

ACKNOWLEDGEMENTS

I would like to gratefully acknowledge Professor Sandra J. Rosenthal for providing me the opportunity and flexibility to work on this project, and specifically the guidance towards the exploration of lithographic-based techniques.

I would also like to thank Dr. Stephen J. Pennycook for providing me with the opportunity to work with his group and their world-class microscopes at Oak Ridge National Laboratory (ORNL).

I would like to acknowledge my committee for taking the time to aid me in my graduate school career; specifically, I would like to thank my co-PI within the IGERT program, Professor Leonard Feldman, and the head of my department, Professor Jim Wittig, for their support and direction through the IGERT program, in the classroom, as well as in the laboratory.

This project would have been impossible without the training, support, and general guidance of the members of the Rosenthal group. Specifically, I would like to thank James McBride for TEM training, Danielle Garrett for teaching me the non-crystalline version of the ABC-based meso-TiO_2 synthesis, Nathanael Smith for guiding me towards a more repeatable and better meso-nc-TiO_2 procedure, and Laura Swafford for all things photovoltaic, theoretical, and grammatical. Furthermore, where samples were provided by members of the Rosenthal group, I have acknowledged them in the text.

I would also like to acknowledge the following graduate students: Jonas Perez for helping repeat the synthesis of Honma and coworkers during his rotation in the Rosenthal group, Tripp Morris for SEM and XRD training and technical support, Jared Crochet for AFM training, and Teresa Croce for help with PMMA dissolution.

I cannot begin to thank enough Dr. Pennycook's STEM group at ORNL for their training, help and support. Particularly, Andrew Lupini, Albina Borisevich, and Juan Carlos Idrobo, who spent many long hours helping me along the way.

Outside of this project, I would like to thank Michael Bowers for nanocrystal synthesis training, Tony Hmelo, Sriram Dixit, and Walter Augustyniak within Dr. Feldman's group for RBS training, and the IGERT program and Interdisciplinary Program in Materials Science in general.

Finally, I would like to thank Kristen Brosnan, whose support and encouragement have made this thesis a reality.

This work would not have been possible without the financial support of Vanderbilt University and the Department of Energy (grant # DE-FG0202ER45957). Collaborators within the Rosenthal group were also funded by the National Institutes of Health (grant # 5r03191-161874-02). Furthermore, the author was supported by a National Science Foundation IGERT fellowship (DMR-0333392). The author would like to thank the DOE-TEAM Project for use of the FEI Titan™ 80-300 STEM.

CHAPTER I

INTRODUCTION

Motivation

According to the U.S. Department of Energy, global demand for energy is expected to more than double by 2050 exceeding 30 terawatts (TW) and more than triple by the end of the century to 46 TW.[1] Nonrenewable resources, fossil and fissionable nuclear fuels, are being increasingly depleted and their continued use poses grave environmental threats. Excluding solar energy, the total renewable energy potentially available worldwide from wind, tidal, geothermal, biomass and hydroelectric sources is estimated to be between 12 and 27 TW, of which only a small fraction is currently utilized.[2] Meanwhile, sunlight delivers more energy to the Earth in one hour than all the energy consumed on the planet in a full year; 125,000 TW strike the Earth's surface: 36,000 TW on land, of which 2,200 TW are within the U.S.[2] If utilized, 10% efficient photovoltaics covering 0.16% of land on Earth would provide 20 TW of power, while covering a mere 1.6% of U.S. land would fulfill the entire country's energy needs.[2]

Despite solar energy's enormous potential, it accounted for less than 0.1% of the world's electricity in 2001.[2] The primary reason for this discrepancy is today's photovoltaic-generated electricity's exorbitantly high cost, which is approximately 5 to 10 times greater than fossil or nuclear electricity, and 10 to 20 times greater than primary fossil energy.[3] The cost of solar electricity is dictated by the relatively high fabrication costs and low efficiencies of today's commercial bulk silicon solar cells, which typically

require processing from a silicon melt (above 1414 °C) and have a theoretical efficiency limit of ~30%.[4] To bring the cost of photovoltaics low enough to compete with today's nonrenewable energy sources, paradigm-shifting research into new solar electricity conversion technologies is required.[2] Within the Rosenthal group at Vanderbilt University, we are pursuing one of these technologies: a fully solid-state, inorganic nanomaterial-based photovoltaic ─ an evolution of the electrolyte-based Grätzel cell.[5]

Nanomaterial-Based Photovoltaics

Specifically, we are we are pursuing an ordered bulk heterojunction photovoltaic[6] featuring mesoporous nanocrystalline anatase titania (meso-nc-TiO_2) functionalized with PbS/PbSe[7] inverse core/shell[8] nanocrystals shown in Fig. 1 (left). We seek to achieve efficiencies approaching that of photosynthesis, nature's 99% efficient photon-to-electron conversion system, by designing our photovoltaic biomimetically such that it separates the functions of light harvesting and charge transport, with initial charge separation being ultrafast and unidirectional.[6] Further efficiency gains will be realized by utilizing chemical self-assembly[9] to form an interpenetrating network[10] of functional constituents with an increased photoactive region as compared to bulk thin films.[2,6] Low production costs will be achieved by using semiconductor nanocrystals, which are synthesized pyrolytically at temperatures less than ~300 °C,[11] as the principal light-harvesting agent, while the inorganic framework will consist of nanostructured titania, an inexpensive material used as a pigment in a wide variety of applications, indium tin oxide (a transparent hole conductor), an aluminum electrode, and a small molecule chemical linker connecting the semiconductor nanocrystals to the titania (TiO_2). Figure 1 includes

a theoretical band diagram (right), which highlights that charge separation is primarily driven by enthalpy as charge carriers lower their energy as they travel away from the inverse core/shell.[6] We envision this photovoltaic to be low cost and highly efficienct, as well as highly robust owing to its inorganic make-up.

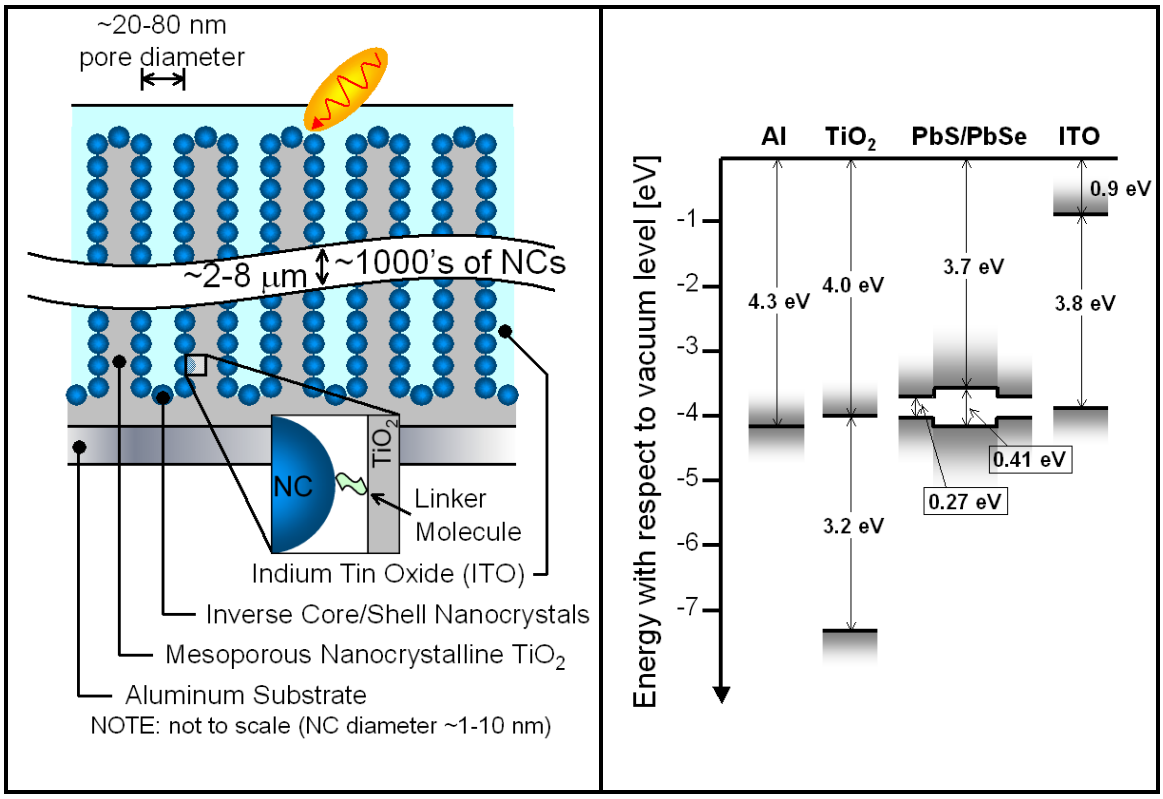

Figure 1: Nanomaterial-based photovoltaic. Left: Idealized graphic representation (not to scale) of a fully solid-state, inorganic nanomaterial-based photovoltaic. Right: Energy band diagram showing work function and band gap (where applicable) of each component; note that the alignment of the bands reduces back-transfer of charge carriers.[2]

The benefits of meso-nc-TiO_2 are three-fold: (1) the vertical orientation of the ~50 nm wide pores will allow the incorporation of both semiconductor nanocrystals, via chemical self-assembly, and the hole-conducting material (ITO in this case); effectively 'stacking' the nanocrystals vertically above the aluminum substrate will increase the

photoactive region, an effect known as the area enhancement factor (AEF),[6] while physically separating the electron and hole conduction materials, TiO_2 and ITO respectively, will reduce the surface area for charge recombination,[2,12,13] (2) the pore walls are comprised of an amorphous network surrounding anatase nanocrystallites, which will likely improve the electron mobility and therefore the device efficiency over a purely amorphous framework,[6,14] with the further advantage of anatase being the allotrope of titania having the highest charge-carrying rate,[15] and (3) the TiO_2 nanocrystallites will also be able to generate charge carrier pairs, albeit relatively few, upon near-UV solar irradiation, typically around 3% of the spectral output of sunlight for anatase TiO_2,[12] with the synergistic benefit of improved performance when functionalized with lead-containing nanocrystals.[16] Ultimately, periodically-arrayed monodisperse nanocrystals in nanostructured TiO_2 could enable preferential attachment of specific crystal facets, resulting in optimal charge separation.[2]

In addition to their photostability (resistance to photodegredation), incorporating semiconductor nanocrystals as the active light-harvesting agent in our proposed photovoltaic will improve photoconversion efficiency for several reasons. The permanent intrinsic dipole present in stoichiometric nanocrystals[17] will act to vectorially separate charge carriers on the ultrafast timescale, potentially reducing the annihilation of charge carriers within the nanocrystal,[13] and meeting the requirements for subsequent separate charge transport and extraction.[18] Furthermore, the quantum confinement effects resulting from the size of the nanocrystals will positively impact efficiency in a number of ways: first, nanocrystals exhibit large extinction coefficients, on the order of $\sim 10^6$-10^7 L/mol-cm at the band gap for CdSe nanocrystals,[6] second, nanocrystals exhibit enhanced

absorption cross sections, for example a 35 Å CdSe nanocrystal has one thousand times the absorption cross section of bulk CdSe,[13] and finally, quantum confinement in nanocrystals allows band gap tunability with size and composition.[19] Engineering the band gap can improve device efficiency because band edge absorption is the most effective light harvesting behavior,[20] and because the band gap can be tuned to capture as much of the solar spectrum as possible.

This desire to maximize the amount of the solar spectrum utilized has led to the inclusion of Pb-containing nanocrystals in our proposed photovoltaic. Nearly half of all solar energy lies beyond 700 nm,[18] which is above the limit of most Cd-containing nanocrystals. Pb-containing nanocrystals, such as PbS and PbSe, have bulk band gaps much smaller than Cd-containing nanocrystals, which means they can absorb into the near-IR portion of the solar spectrum; PbSe for instance, would be able to harvest nearly the entire solar spectrum.[6] An added benefit of using smaller band gap nanocrystals is that of impact ionization,[21,22] also known as inverse Auger scattering. In PbSe nanocrystals it has been shown that a single photon of more than twice the band gap can produce two or more charge carrier pairs, a phenomenon known alternately as carrier multiplication or multiple exciton generation.[7,23] Photons with energy greater than the band gap, which would otherwise be lost as heat, instead add to the photoconversion efficiency of the device. In theory, photovoltaic conversion efficiency could by increased via the effect of impact ionization above ~65%.[2] Additionally, PbS nanocrystal cores will be coated with a narrower band gap shell material, PbSe (0.41 and 0.27 eV respectively). In contrast to the more common core/shell nanocrystals, which localize charge carriers within the core and thereby enhance fluorescence quantum yield, by optimizing the core

to shell, radius to thickness ratio, we hope to localize charge carriers principally in the shell.[8] There they will be more likely to be transported separately along their respective pathways (TiO_2 and ITO), further reducing the probability of electron-hole recombination. Charge-carrier localization in inverse core/shells and carrier multiplication in small band gap semiconductor nanocrystals are illustrated in Fig. 2.

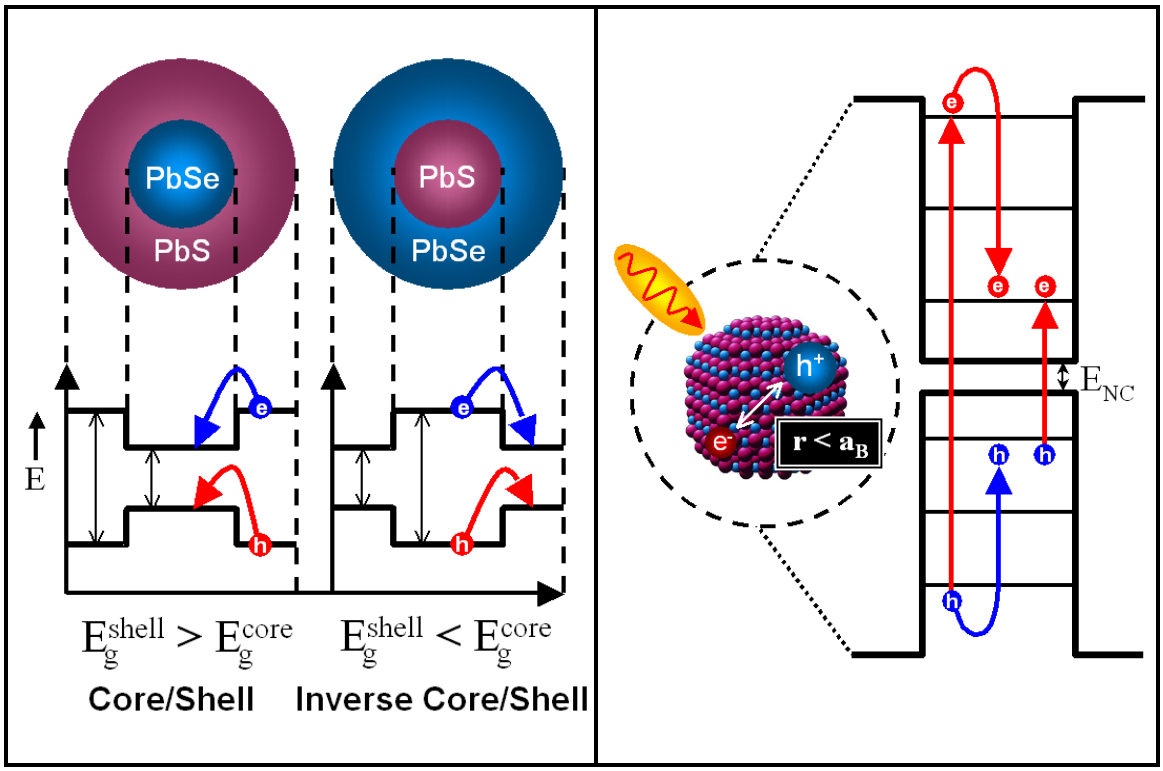

Figure 2: Inverse core/shell and impact ionization. Left: Charge-carrier localization in inverse core/shell nanocrystals. Charge-carriers are theoretically confined to the core in conventional core/shell nanocrystals, and to the shell in inverse core/shell nanocrystals. Right: Impact ionization occurs in semiconductor nanocrystals that experience quantum confinement because their diameter is on the order of their bulk Bohr radius, a_B. In small band gap nanocrystals, a single incident photon of more than twice the band gap can produce two or more electron-hole pairs ─ a process known as multiple exciton generation.

The meso-nc-TiO_2 could be functionalized with PbS/PbSe inverse core/shells via a chemical linker molecule, likely mercaptopropionic acid (MPA).[24-26] MPA can act as a

bifunctional surface modifier because the carboxylate group at one end has a strong affinity for TiO_2, while the Thiol group on the opposite end binds strongly to the nanocrystals.[26] Optimizing the linker molecule, for instance by incorporating a shorter molecule to lower the barrier to charge carrier dissociation,[18] may be critical to final device efficiency.

Conversely, a physical deposition method such as electrophoretic deposition (EPD) could be used.[27] If functionalization via MPA is analogous to chemisorption, whereby an adsorbate adheres to a surface through the formation of a chemical bond, EPD is analogous to physisorption, which works only through weak intermolecular Van der Waals interactions. EPD has already been used to deposit a variety of nanocrystal systems,[28-30] including CdSe nanocrystals.[31-34] EPD employs the internal dipole moment of semiconductor nanocrystals[35] to transport them through a non-polar solvent to a charged anode or cathode. In comparison to attachment via MPA, which can take up to two days, EPD can deposit nanocrystals in 15 to 20 minutes, making it a more attractive process for large-scale production.[27]

Finally, if necessary, a barrier oxide between the ITO and the nanocrystals may be added. This barrier would be incorporated in order to prevent charge carrier back reaction and to self-heal the structure where missing nanocrystals could permit recombination.[13] Although a variety of work has been published on photovoltaic (and photocatalytic) devices that share many of the characteristics of our envisioned nanostructured solar cell, including Pb-containing nanocrystals, meso-nc-TiO_2, and chemical linker molecules connecting the constituents, to the best of our knowledge, we are the only group that has

proposed such an ambitious device that could potentially benefit from the wide variety of phenomenon mentioned above.

Characterization Techniques

Scanning electron microscopy (SEM) works primarily by detecting secondary electrons that are inelastically scattered by atoms within the interaction volume near the surface of the sample. The SEM's minimum probe size is too large to make it suitable for imaging either TiO_2 or semiconductor nanocrystals, as is possible with the transmission electron microscope (TEM, see below). However, because it images with secondary electrons, it is ideal for imaging amorphous TiO_2 nanostructures prior to calcination and for imaging thick TiO_2 films or tall TiO_2 pore walls; conversely TEM predominantly images crystalline materials and cannot be used to image specimens too thick for the electron probe to traverse. Of importance to this work, the SEM is limited in its depth of field, which makes determining pore depth by plan view imaging unworkable, and both oxide and polymer specimens alike experience varying degrees of sample charging, which hinders clear imaging of the final calcined product and makes imaging of the polymer mold nearly impossible.

Both x-ray crystallography (XRD) and transmission electron microscopy (TEM) rely on the crystallinity of the nanostructured material, CdSe or TiO_2 for example, to garner useful information. By measuring the diffraction of an x-ray beam incident on a crystalline sample, XRD allows definitive allotrope assignment by comparison with known diffraction patterns (PDFs). When used to investigate nanocrystallites, peak broadening in the XRD can be used to estimate crystallite size via the Scherrer's

equation. Similarly, the TEM relies on the periodic nature of the crystal lattice to generate a phase contrast image of a nanocrystalline sample. Exact atomic positions can only be discerned from high-resolution TEM images using techniques such as focal series reconstruction or off-axis holography, while lattice fringe spacing can sometimes be used for allotrope determination.

In contrast to TEM images, which can be used to produce data on a nanocrystal by nanocrystal basis, every XRD trace produces data from an enormous number of nanocrystals. Specifically, TEM imaging and XRD can be used to determine nanocrystal structure and size, while TEM alone can be used to determine nanocrystal shape. Another characterization technique that produces data from an ensemble of nanocrystals within a sample is Rutherford backscattering spectroscopy (RBS), which can be used to determine nanocrystal stoichiometry with an accuracy better than a picomol.[36] RBS can be used to measure chemical composition by comparing the proportional energy variation of backscattered ions; heavier elements scatter ions to a greater extent than lighter ones.

While TEM allows the determination of the crystal structure of individual nanocrystals, and can be used to size nanocrystals when many images are used, surface structure and chemical composition are nearly impossible to resolve.[12,31] In order to image individual nanocrystal surfaces, aberration-corrected atomic number contrast scanning transmission electron microscopy (Z-STEM) must be used. Aberration-corrected Z-STEM microscopes can be used to produce atomic resolution images with unprecedented detail. In fact, Z-STEM imaging has been used routinely for the last few years to produce images with resolution below one Ångstrom.[37-41]

CHAPTER II

BACKGROUND

ABC-Based Meso-nc-TiO_2 Background

Two synthetic methods were pursued to produce the mesoporous nanocrystalline anatase titania (meso-nc-TiO_2) framework: the first was a "bottom-up" self-assembly approach based on the incorporation of a large amphiphilic block copolymer (ABC) into a TiO_2 sol-gel, and the second was a "top-down" lithography-like approach that used a polymer mold, patterned by an anodic alumina oxide (AAO) template, to emboss a TiO_2 sol-gel.[42]

The chemical self-assembly approach to mesoporous materials had limited access to the size regime of 2 to 50 nm pores, which the IUPAC defines as mesoporous, until the early 1990's when chemists at the Mobil Corporation discovered that by using large organic amphiphilic surfactant molecules (ABCs) as templates for the final inorganic structure, they could synthesize materials with highly controlled pores in the 2 to 10 nm range.[43,44] The incorporation of nanocrystallites into the pore walls of a wide variety of transition metal oxides, including TiO_2, was first reported in 1998 by Galen D. Stucky's group at the University of California at Santa Barbara,[45] but it was not until 2002 that Stucky and coworkers reported predictably producing materials with nanocrystal-containing pore walls.[46] The difficulty until then had been that the pore walls, pore diameters, and nanocrystallite domains were all approximately the same size; therefore,

during calcination, TiO_2 nanocrystals grew larger than the pore walls, into the pores themselves, thereby reducing or altogether eliminating the mesoporosity.[47,48]

Maintaining the mesostructure during crystallite growth, primarily by improving the thermal stability of the material, became the research focus of the field and in 2003 Crepaldi *et al.*[49] and Li *et al.*[50] both reported thermal stability up to 500 °C. Of greater interest to this work, Ozin and co workers were able, by changing the main solvent from ethanol to 1-butanol and controlling the relative humidity and temperature during aging, to produce thermally stable and crack-free thin films up to 1.5 by 2.3 inches on a glass substrate.[51] Over the same time period Itaru Homma's group at Japan's National Institute of Advanced Industrial Science and Technology was employing mixed-metal oxide frameworks to improve the nanocrystalline character of their materials,[50,52] an idea that was fully realized in 2005 with the publication of their report describing a ternary Li_2O-TiO_2-P_2O_5 mesoporous oxide possessing "almost fully nanocrystalline anatase… made up of nanocrystalline anatase and tiny quantities of amorphous phase".[2]

It should be noted that meso-nc-TiO_2 has already been used as a framework material for nanoscale host/guest structures, including semiconductor nanocrystal photovoltaics arrayed within meso-nc-TiO_2.[6] Meso-nc-TiO_2 is also under investigation for use in organic-inorganic solar cells.[53] Michael D. McGehee at Stanford, a former member of Stucky's group at UCSB, has worked to incorporate aligned conjugated polymers as both electron and hole conductors.[54] Meanwhile, Stucky's group has taken this work in a different direction by infiltrating chalcogenide gases into mixed metal oxide-semiconduction oxide mesoporous hosts, thereby growing semiconducting nanocrystals within the mesopore walls.[55] In fact, the use of meso-nc-TiO_2 in

photovoltaic applications was validated by the long-time leader in the field, Michael Gratzel, who proposed to employ it in dye-sensitized solar cells.[14]

Embossed Sol-Gel TiO_2 Background

Unfortunately, the diameter of pores synthesized in the ABC approach is limited to about 15 nm, so it is not surprising that McGehee's group published a paper in 2005 (Goh *et al.*, Ref. 42) outlining the synthesis of vertically aligned pores with diameters between 30 and 65 nm, including anatase nanocrystals within the pore walls. This meso-nc-TiO_2 was reported to contain ~120 nm deep pores (with aspect ratios of 2 to 3), with defect-free regions as large as 200 μm by 200 μm allowing for large-scale uniformity of replication, and no metal ion contamination, which can introduce trap states or scattering centers, subsequently reducing photoconversion efficiency. This paper is noteworthy in that it addresses a size regime that is rarely tackled within the inorganic sol-gel literature, and according to the authors, their material is the only one to combine feature resolution below 50 nm with a high areal density of features with high aspect ratios. According to Goh *et al.*, their method of embossing a TiO_2 sol-gel with a polymer mold is analogous to the top-down approach of reverse-nanoimprint lithography. McGehee proposes to use this material in a polymer-based photovoltaic,[56] where many of the requirements are the same as the solid-state device described here.

TiO_2 Nanotube Background

Although Goh's embossed TiO_2 represents a significant improvement over the ABC-based synthetic approach, it still may not meet our dimensional requirements.

According to Goh *et al.* the maximum film thickness prior to cracking due to sol-gel condensation is ~150 nm thick, with ~120 nm deep pores. Even assuming idealized sol-gel condensation, a stiffer polymer would be required to produce deeper pores, and this method is potentially limited to pore depths in the hundreds of nanometers. However, according to our envisioned photovoltaic architecture, pore depths of 5 to 10 μm will be necessary.[6] Although it may be possible to stack TiO_2 layers, this would be added complexity that could possibly be avoided. Conversely, high-aspect ratio TiO_2 nanotubes could meet our dimensional requirements; in fact, TiO_2 nanotubes have previously been functionalized with CdS[57,58] and used in dye-sensitized solar cells.[59-62]

Craig A. Grimes' group at Penn State has exhaustively pursued one approach to produce up to ~134 μm deep TiO_2 pores with suitable diameter and wall thickness.[63] Their material is produced in a similar fashion to the anodic alumina oxide template used in the Goh *et al.* synthesis of embossed TiO_2. A thin Ti foil is anodized in an acid bath with specific parameters, causing it to develop an oxide of hexagonally packed parallel nanotubes, as opposed to the Al oxide which forms a continuous structure. Grimes and coworkers have applied their titania nanotubes to solar cells[10,64,65] and as photocatalysts,[66] including functionalizing their material with CdS nanocrystals.[67]

Electron Microscopy Background

High-resolution transmission electron microscopy (HRTEM), in which lattice planes are visible, is the most commonly used technique for characterizing the structure of semiconductor nanocrystals.[39] There are a wide variety of resources available which cover it in depth; in particular, the fundamentals of the TEM are well covered in the text

by Williams and Carter,[68] while the specifics of imaging CdSe nanocrystals are contained in James McBride's Ph.D. dissertation.[39]

Unfortunately, even with HRTEM, surface and compositional information cannot be determined. Conversely, aberration-corrected atomic number contrast scanning transmission microscopy (Z-STEM), which uses a high-angle annular dark field (HAADF) detector to produce an incoherent - and therefore direct - image,[68] can be used to garner atomic-level structural and compositional information at the same time[69] without extensive post-imaging simulation.[70] Despite the enormous potential, the imaging of pyrolytically-synthesized semiconductor nanocrystals via Z-STEM has been limited to very few publications to date, including a report by Silcox and coworkers[71] and works by the Rosenthal group.[39-41,72,73]

In the Z-STEM, elastically scattered electrons are typically scattered coherently at low angles (forward); they can be used to form phase contrast images, just like in a conventional TEM, known as a bright field images.[68] Inelastically scattered electrons on the other hand, almost always scatter incoherently, some to high angles.[68] If the incoherently scattered electrons that are scattered to high angles are collected by an HAADF, without diffraction and phase contrast overwhelming the signal, they can be used to form images with atomic number (Z) contrast.[74] This incoherent scattering of electrons is proportional to the atomic number to the power of ~1.7,[75] therefore more electrons will scatter off a heavier atom, causing it to appear brighter in the final image.[72] Consequently, Z-contrast images contain both chemical information as well as spatial information from the direct interpretation of the incoherently formed images.[76] These Z-

contrast images are alternatively known as dark field images, annular dark field images or HAADF images.

Unlike in the conventional TEM, the Z-STEM's objective lens is located before the specimen; therefore the microscope's peak resolution is directly proportional to the size of the electron probe, and is in turn limited only by the beam energy and by aberrations in the post-specimen lenses.[77] Ultimately, the resolution in an electron microscope is limited by aberrations resulting from imperfections in the electron lenses. Beyond astigmatism, which can be easily corrected with a pair of octupoles, spherical aberration (C_s), due to the over focusing of off-axis electrons by the electron lenses, and chromatic aberration (C_c), due to the varying energies of electrons within the beam, are more difficult to correct. [68] The development of ever more sophisticated aberration correctors for use in Z-STEM microscopes has allowed for the correction of third-order C_s,[77-79] and hopefully fifth-order C_c in the near future.[80,81]

In this work two 300 kV aberration-corrected Z-STEM microscopes were used within Steve Pennycook's STEM group at Oak Ridge National Laboratory (ORNL). The first was a VG Microscopes HB603U with a Nion quadrupole-octupole C_s corrector[77,78,82-84] (known simply as the VG603) that has been producing images with 0.78 Å resolution since 2004.[38] More recently, an FEI Titan™ 80-300 STEM with a CEOS hexapole C_s corrector,[85,86] has been installed as part of the DOE's TEAM project, a joint effort between ANL, BNL, LBNL, ORNL and the Frederick Seitz Materials Research Laboratory at UIUC.

CHAPTER III

EXPERIMENTAL METHODS

ABC-Based Meso-nc-TiO_2 Synthesis

Mesoporous nanocrystalline anatase titania (meso-nc-TiO_2) was prepared via sol-gel self-assembly resulting from the use of a long-chain amphiphilic block copolymer (ABC); in this case, Pluronic P123 from BASF corporation, a triblock copolymer of poly(ethylene oxide)-poly(propylene oxide)-poly(ethylene oxide) with the chemical formula $HO(CH_2CH_2O)_{20}(CH_2CH(CH_3)O)_{70}(CH_2CH_2O)_{20}H$ (designated $EO_{20}PO_{70}EO_{20}$) was used. In a typical synthesis,[52] 1 g of Pluronic P123 was dissolved in 10 g of ethanol (C_2H_5OH), to which was added a solution of 2.6 mL titanium (IV) isopropoxide ($Ti(OC_2H_7)_3$) in 0.3 g of 2 M HCl while stirring. The solution was allowed to stir overnight (20 hours total), and subsequently spin coated for ~30 seconds at 2500 r.p.m. onto glass or silicon substrates. The thin films were allowed to air dry at room temperature for 5 days, followed by 7 days in an oven (in air) at 80 °C. The samples were heat-treated at 400 °C for 6 hours in air to remove the organic species, followed by calcination at 650 °C for 1.5 hours in air to produce the desired nanocrystallinity.

Embossed Sol-Gel TiO_2 Synthesis

Nanostructured TiO_2 samples with vertically-aligned pores in the meso- to macroporous size range were synthesized by embossing TiO_2 sol-gels with polymer molds patterned from anodic alumina oxide (AAO) templates.[42] Double-sided AAO templates were purchased from Synkera Technologies of Longmont, CO, with nominal

dimensions of 55 nm diameter and 1 μm depth. A ~250 nm thick layer of 2.5% polymethyl methacrylate (PMMA, $(C_5O_2H_8)_n$, M_w=350 kg/mol) dissolved in chlorobenzene (C_6H_5Cl) was spin coated at 2000 r.p.m. for 30 seconds onto the AAO template. The PMMA was infiltrated into the AAO pores by heating in air for 5 minutes at just below 200 °C, well above its glass transition temperature of 120 °C. A macroscopically thick (>1 mm) layer of polydimethylsiloxane (PDMS, $(CH_3)_3SiO[SiO(CH_3)_2]_nSi(CH_3)_3$, Dow Corning Sylgard® 184 Silicone Elastomer) was coated over the PMMA infiltrated into the AAO and cured. The polymer mold was retrieved by wet chemical etching: a combined 3 hours in 10 wt % NaOH was usually enough time to remove the alumina on both surfaces of the Al foil substrate, while 1.5 hours in 1.4 wt % $FeCl_3$ in 4 M HCl was typically sufficient to dissolve the Al. A TiO_2 sol-gel had been previously prepared by mixing 1 g of titanium (IV) ethoxide ($Ti(OCH_2CH_3)_4$), 0.15 g of HCl, and 8 g of isopropanol ($(CH_3)_2CHOH$). After template removal, the free-standing PMMA rods with PDMS backing were spin coated with a TiO_2 sol-gel at 1500 r.p.m. for 30 seconds. The polymer mold coated with TiO_2 was immediately embossed onto a substrate, typically Si, and the solution was allowed to dry at room temperature for a minimum of one day. After drying, the PDMS backing was removed and any residual PMMA within the pores was dissolved by sonication in acetonitrile (CH_3CN) for 1 to 2 hours. The mesoporous TiO_2 samples were calcined at 450 °C for 6 hours in air to form nanocrystalline anatase TiO_2.

Characterization Methods

X-ray diffraction (XRD) scans were obtained using a Scintag X_1 θ/θ automated powder X-ray diffractometer with a Cu target (λ = 1.54056 Å), a Peltier-cooled solid-state detector, and either a zero-background, Si(510) sample support, or as prepared on a silicon wafer. The average TiO_2 nanocrystallite size, d, was calculated from a form of the Scherrer's equation modified for spherical particles,[87] $d=(4/3)K\lambda/(\beta\cos\theta_b)$, assuming that peak broadening arises from size effects only, and individual nanocrystals are not multi-domain. For a given peak, β is the full-width at half-maximum intensity in radians on the 2θ scale, λ is the wavelength of X-rays used (1.54056 Å), θ_b is the Bragg angle for the measured hkl peak, and K is a primarily shape-related coefficient[87] equal to 0.9 for d taken as the volume-averaged crystallite dimension perpendicular to the hkl diffraction plane.

A Hitachi S-4200 scanning electron microscope operating at nominally 15 kV was used to collect SEM images. The meso-nc-TiO_2 samples were imaged either as prepared, or after sputter coating with a thin layer of gold or platinum (Pelco model 3 Sputtering Instrument) to avoid charging. Film thickness was primarily determined by imaging small fragments of film standing on edge. These fragments were produced by scoring the film with a clean razor blade, which produces a macroscopic channel with nanoscale fragments at its edges. A Philips CM 20T transmission electron microscope (TEM) with a LaB_6 emission source operating at 200 kV was used to collect images of the calcined meso-nc-TiO_2. Samples were prepared by scraping the TiO_2 films off of the

substrate, sonicating in isopropanol for 30 minutes, and pipetting onto holey carbon grids, followed immediately by wicking away excess solvent with a Kimwipe™.

Z-STEM Experimental

Embossed TiO_2 samples, with and without nanocrystals, were prepared in the same way for Z-STEM imaging as they were for TEM imaging: by scraping the films off their substrate, sonicating in isopropanol for 30 minutes, and pipetting onto holey carbon grids, followed immediately by wicking with a Kimwipe™. Nanocrystal samples however were cleaner and more dilute when prepared for Z-STEM as opposed to TEM; additionally, ultra-thin carbon on lacey support TEM grids were used instead of ultra-thin carbon on Formvar (both purchased from Ted Pella, Inc.).

Samples imaged in the VG603 were sometimes heated with a light bulb in air for 10-15 minutes or plasma cleaned for 5-10 seconds prior to insertion into the air lock. While under vacuum they were heated again with a light bulb for 10-15 minutes, allowed to cool for 15-20 minutes, and then inserted into the column, where they were often allowed to cool down overnight. These steps were taken to reduce excess organics, which often polymerized and agglomerated under beam irradiation, obscuring the images. A complete explanation of the operation of the VG603 can be found in the aforementioned thesis.[39] In the case of samples imaged in the Titan, where no light bulb treatment under vacuum was available, nanocrystal samples were plasma cleaned for 5-10 seconds immediately prior to insertion into the column.

Unlike the VG603, where the vacuum is controlled manually during specimen exchange, the Titan has a computer-controlled routine. An external turbo pump was used

as a roughing pump before the microscope took control in the ultra-high vacuum range. Because the column of the Titan is based on that of the Technai™ and earlier Philips microscopes, sample insertion was quite similar to that of the Philips CM 20T located at Vanderbilt. After sample insertion, the roughing pump was shut down, and the beam was allowed down the column by opening the column valves.

In contrast to the VG603, which is a dedicated STEM, the Titan can operate in both STEM and conventional TEM modes. In fact, the manufacturer (FEI) offers Titans with aberration correctors before the specimen (for conventional TEM), after the specimen (for STEM), and both before and after the specimen. After confirming the Titan was in STEM mode, the condenser aperture was set to 150 μm and the spot size was set to 8. The DOE-TEAM Project's Titan is outfitted with a monochromator; although it is not typically used in STEM imaging, it is paired with an ultra-stable power supply, critical for atomic-resolution imaging.

The monochromator tended to drift, particularly when the microscope was not in use for an extended period of time, such as overnight, and therefore had to be adjusted at the beginning of each session. Coarse alignments and aberration corrector settings were also prone to drift overnight, and were often adjusted every morning. Prior to initial imaging, the eucentric height of the specimen was found, all lenses were normalized, and the beam was reset. The beam was then aligned using a combination of the microscope's console controls and the aberration corrector software.

After the electron beam had been optimized (i.e. monochromator adjusted, beam aligned, etc.) there were two options for further tuning. While the aberration corrector software could have been used from this point onwards, it was customary to optimize the

Ronchigram in a fashion similar to tuning the VG603.[39] As in the VG603, optimizing the Ronchigram was easiest when nanocrystals were visible in the field of view at magnifications below 500 kX. When optimizing the Ronchigram, wobbling the defocus was used to locate the center of symmetry. Generally speaking, if the center of focus was not centered within the field of view then coma needed to be reduced; if the center of focus was not round, or the features within the center of focus were elongated, then the beam was astigmated.

After optimizing the Ronchigram, the condenser aperture was set to 70 μm, the camera length was set for imaging, the specimen was returned to the eucentric height, and the HAADF detector was inserted into the column. After a dark field image was brought into focus, the aberration corrector software was used to fine-tune the corrector. First and second order aberrations were coarse-tuned using the continuous defocus feature. After multiple iterations using the continuous defocus function, A1 and C1, also known as two-fold astigmatism and defocus respectively, could be held below 1 nm each. The tableau function could then be used to tune the higher-order aberrations.

In addition to correcting A1 and C1, the initial iterations of the tableau feature were used to correct A2 and B2, also know as three-fold astigmatism and axial coma respectively. After each iteration, the corrector software suggested an aberration to correct for; while this was not always the best choice, it often was, and almost always was correct for lower order aberrations, such as A2 and B2. After three to four iterations of the tableau feature, it was usually prudent to check for specimen drift, followed by coarse tuning the coma and astigmatism using the continuous defocus feature. It is noted

that a slight misalignment between the hexapoles in the corrector appear as astigmatism in the images.[75]

Finally, third order aberrations were corrected using the enhanced tableau feature. Specifically, A3, S3 and C3, known as four-fold astigmatism, star aberration and spherical aberration (C_s) respectively, were corrected by increasing the tilt to 24-28 milliradians (mrad), setting the probe semi-aperture to 24.7 mrad (for the 70 μm aperture), and adjusting for the measurements of the enhanced tableau. Any adjustment of the higher order aberrations required a re-calibration of the lower order aberrations, as focused imaging ultimately depended on reducing coma and astigmatism.

CHAPTER IV

CHARACTERIZATION OF MESOPOROUS OXIDES WITH AND WITHOUT DEPOSITED NANOCRYSTALS

ABC-Based Meso-nc-TiO_2

The amphiphilic block copolymer (ABC) self-assembly approach was first used to synthesize material by following the literature preparation of Homma and coworkers.[52] While they typically synthesized a mixed-metal oxide, the focus of this project remained on a purely TiO_2 framework. Complications arose during the gelation step, and it became apparent that their quantity of catalyst (HCl) would not be appropriate given our specific conditions, which included unknown variables such as age of chemicals, relative humidity, etc. Ultimately, the correct quantity of HCl was empirically determined such that the sol-gel product matched their results. Figure 3 contains two TEM images taken from separate trials that show mesoporosity, nanocrystallinity, and reproducibility.

Small-angle and wide-angle XRD characterization of the ABC-synthesized meso-nc-TiO_2 was attempted using multiple specimen preparation techniques. Scans were performed on the material as-synthesized on a Si substrate, scraped off the substrate and sonicated in isopropanol for 30 minutes, and scraped off the substrate as powder. In each case the background overwhelmed the nanocrystalline TiO_2 peaks. This low signal to noise ratio was likely due to the small fraction of crystallized TiO_2 within the amorphous framework,[45] or due to contamination by the Si substrate, either directly in the case of the samples analyzed as-synthesized, or via Si chips accidentally introduced during scraping.

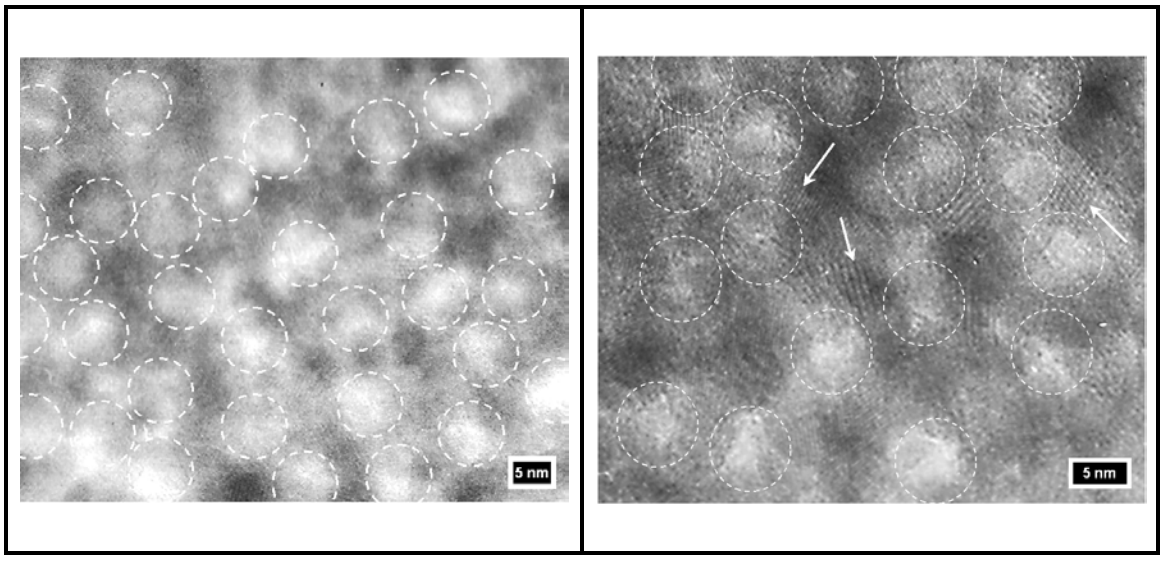

Figure 3: TEM of meso-nc-TiO_2 via ABC self-assembly. Left: TEM image of mesoporous nanocrystalline TiO_2 prepared similarly to the method of Honma and coworkers[52] (dashed white circles denote mesopores). Right: TEM image highlighting nanocrystallinity of TiO_2 (arrows point to lattice fringes or moiré patterns). These images are from separate trials, highlighting the reproducibility of this synthetic technique.

As noted above, the aging and drying times required to produce high-quality meso-nc-TiO_2 are not consistent with low-cost processing. This limitation however, pales in comparison to the inherent shortcomings of all current ABC-based TiO_2 syntheses. The three primary technical requirements of the nanostructured TiO_2 for use in our proposed photovoltaic device are: (1) nanocrystallinity for improved charge carrier transport, (2) pore diameters greater than the sum of three nanocrystal diameters plus linker molecules (to allow self-assembly of nanocrystals and subsequent infiltration of ITO),[88] and (3) vertically aligned pores (again to allow self-assembly and infiltration of ITO). Only the first requirement can be met by ABC-based TiO_2 syntheses, therefore after demonstrating a repeatable process for synthesizing meso-nc-TiO_2 via the ABC approach, and acknowledging its limitations, this bottom-up method was set aside for a

top-down approach, embossing of sol-gel TiO_2 with polymer molds,[42] that would satisfy all three primary technical requirements outlined above.

Embossed Sol-Gel TiO_2

Following the general dimensional requirements outlined in Goh *et al.*, a suitable anodic alumina oxide (AAO) template was located commercially from Synkera Technologies. For comparison, SEM images of four different AAOs are included below in Fig. 4: (a) AAO used by Goh *et al.*, (b) AAO purchased from Synkera Technologies and employed in the present work, (c) AAO reported by Masuda *el at.*[89] as-fabricated (left) and 'ideally ordered' (right) via pretexturing by a SiC master patterned with electron beam lithography, and (d) 'ideally ordered' AAO synthesized by Dr. Deyu Li and coworkers at Vanderbilt University according to the re-anodization process of Masuda and coworkers.[90,91] Of note is the packing efficiency, a consequence of the degree of hexagonal ordering and pore wall thickness, which is seen to increase from the Goh *et al.* AAO to the Synkera AAO, and is maximized in both of the 'ideally ordered' AAOs.

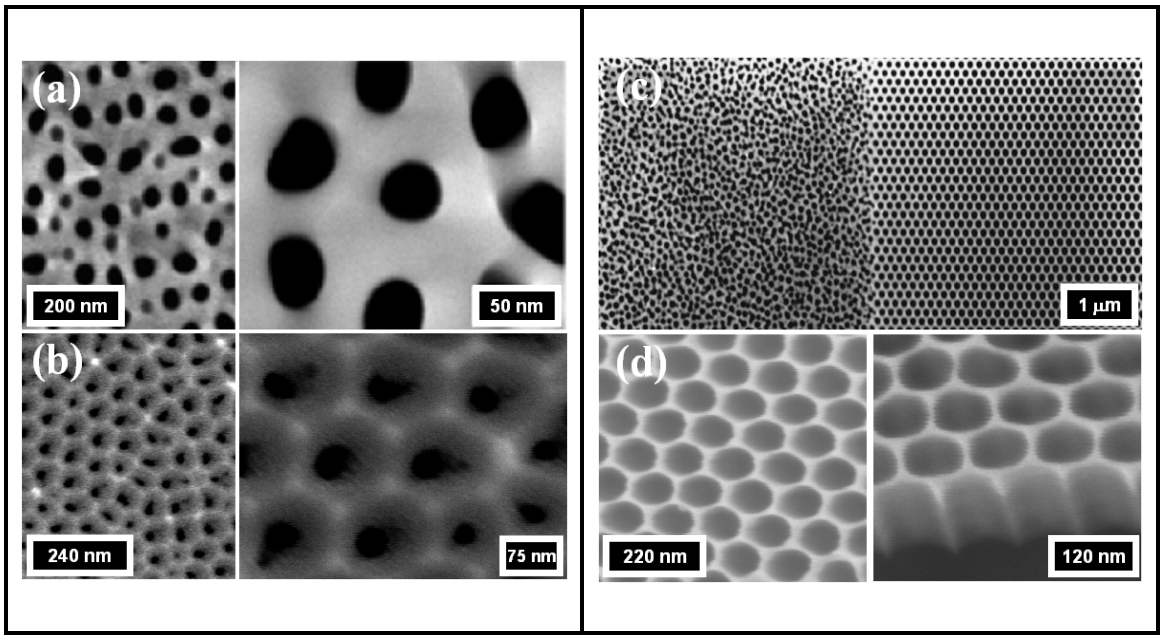

Figure 4: SEM of different AAO templates. SEM images of four different anodic alumina oxide (AAO) materials for use as meso-nc-TiO_2 templates: (a) AAO used by Goh *et al.*, (b) AAO purchased from Synkera Technologies, (c) AAO produced by Masuda el at. as-fabricated (left) and 'ideally ordered' (right) via pretexturing, and (d) 'ideally ordered' AAO synthesized by Dr. Deyu Li and coworkers at Vanderbilt University.

Given that the AAO was purchased commercially, the initial transition from AAO template to final meso-nc-TiO_2 material required minimal modifications to the published synthesis. SEM images representative of more than 50 samples are included in Fig. 5 with the exception of the inset on the right, which is a side-view of the TiO_2 pores as reported by Goh *et al.* Unfortunately, as seen in the image of the film standing on its edge (right), two deficiencies are apparent. First and foremost, the pores do not appear to extend down into the sample more than 25 to 50 nm, which limits the AEF and correspondingly decrease the final device efficiency. Secondly, the TiO_2 film beneath the shallow pores was often in the range of 100 to 1000 nm; TiO_2 films thicker than ~150 nm crack due to tensile stress induced during condensation,[42] and would lower final device

efficiency due to increased resistance, charge recombination, etc.[88] It is noted that TEM imaging of thick films is impossible because the electron beam cannot pass through them.

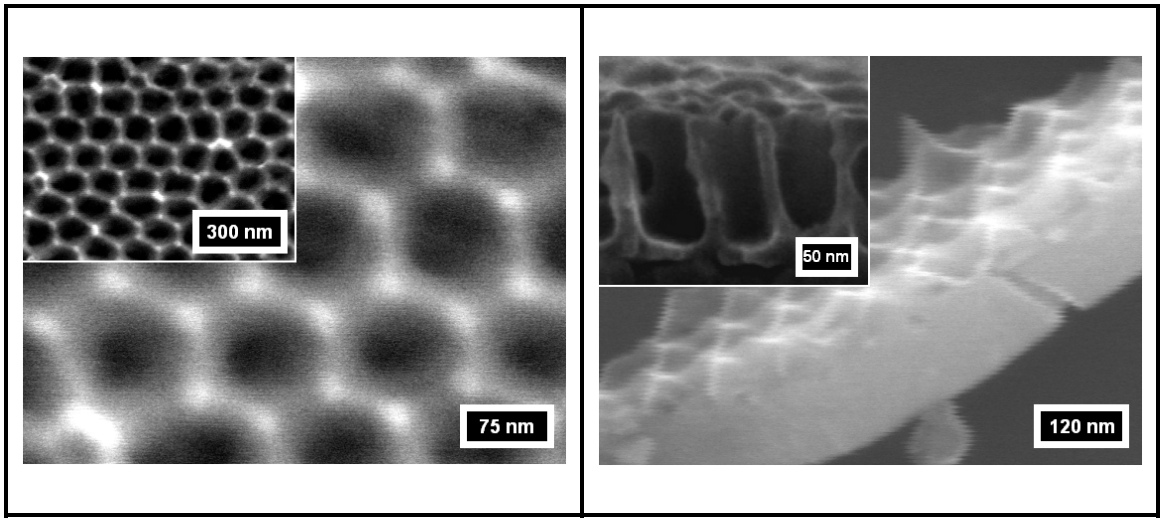

Figure 5: SEM of meso-nc-TiO_2 via embossed sol-gel. SEM images of typical mseo-nc-TiO_2 synthesized according to the procedure of Goh *et al.* representative of more than 50 samples, except for the inset on the right which is an image of Goh *et al.*'s material.[42] In the plan view (left), the final TiO_2 nanostructure closely matches the AAO template (seen in Fig. 4), while when imaged standing on edge (right), the film is greater than 100 nm thick with pores less than 50 nm deep (in contrast to the ~120 nm deep pores visible in the inset at right).

Therefore, replicating McGehee and coworker's ~120 nm deep pores was considered a top priority. The possibility that the imaging capabilities of the SEM did not allow for accurate determination of pore depths was ruled out by viewing a sectioned substrate, coated with Pt to prevent charging. This left two alternatives as the likely culprits: either the PMMA in chlorobenzene was not infiltrating the AAO pores deep enough, or the TiO_2 sol-gel was not penetrating the PMMA positive (i.e. rods). Initial trials focused on sonication as a means to facilitate liquid penetration, however, after many attempts (5 trials composed of 20 samples) no improvement was observed.

Lack of PMMA infiltration into the AAO is more probable when viewed in light of results reported by Goh *et al.* They attempted different stiffness polymers and AAO pore diameters before finding a suitable combination. For instance, a low stiffness polymer (h-PDMS) or a smaller diameter AAO (resulting in 25 nm diameter PMMA rods), they produced rods did not have the stiffness to withstand the van der Waals interaction between them, and collapsed into aggregates of ~500 nm and ~200 nm respectively.[42] Because Synkera's AAO pore depth is nominally 1000 nm, it is highly unlikely that the PMMA in chlorobenzene is in fact infiltrating the pores, but never much more than ~150 nm. If it were reaching that depth or more, then we would have seen an agglomeration of pores in the final product, which was not observed. Therefore, it is quite likely that the PMMA is not penetrating down into the AAO pores.

Beyond sonication, a variety of approaches for guaranteeing PMMA infiltration were devised. Increasing the time at temperature of the infiltration and counter intuitively, lowering the temperature of infiltration, allowing for a decrease in the outward pressure exerted on the incoming PMMA by gas trapped in the pores, were both tested multiple times, however neither produced the desired effect. Similarly, attempting to drive off solvent trapped within the pores after PMMA spin coating but prior to infiltration by heating to below PMMA's glass-transition temperature (~120 °C) was considered. Wetting the AAO with pure chlorobenzene prior to PMMA/chlorobenzene infiltration was also considered, given the possibility that 350 kg/mol PMMA aggregates might be sticking at the top of the nominally 55 nm diameter pores. Finally, increasing (or decreasing) the concentration of PMMA in chlorobenzene was not attempted for two reasons unrelated to its likelihood of solving the problem: first the Goh *et al.* paper calls

for no more than 250 nm of PMMA solution after spin coating, which required referring to electronic device fabrication documentation to determine adequate concentration and spin coating speed, and second, 350 kg/mol PMMA has very low solubility in typical solvents; only two solvents are usually employed (chlorobenzene and THF, tetrahydrofuran), and dissolution is very slow even in these.

Although TiO_2 penetration between the polymer rods was not likely the problem, a few ideas were developed to ensure that it was not inhibiting the formation of deep pores. Because the polymer rods are hydrophobic, and would therefore resist the adsorption of the TiO_2 sol-gel, it was thought that introducing a surface layer of water onto the polymer rods would enhance TiO_2 penetration. Two methods were devised to attempt this approach: (1) immediately prior to TiO_2 sol-gel spin coating, removing the chilled polymer mold from a refrigerator, causing the condensation of water vapor on the rods, and (2) covering the polymer rods with ethyl ether (boiling point of 34.6 °C) and breathing on them while the liquid evaporates, producing the same condensation effect. Chilling the polymer rods would also cause them to contract thereby enlarging the openings available for TiO_2 infiltration.

Ultimately, this overall effort to increase pore depths was limited by two factors. First, there is no currently available technique for determining the height of the PMMA rods. SEM is not suitable because the electron beam damages the polymer mold, while AFM cannot resolve the rod heights due to their high aspect ratios and the minimal space between rods.[42] The only characterization possible is of the final embossed TiO_2 from which we can infer the polymer rod heights. Without the ability to characterize polymer

rod height, it was impossible to determine which step was not working (if not both), and a solution to one but not the other, would have gone unnoticed.

After repeated unsuccessful attempts to resolve the two liquid infiltration problems, a wholly different strategy was developed which removed the PMMA, and its infiltration, entirely. Instead, the TiO_2 sol-gel was spin cast directly onto the AAO template, resulting in the formation of a TiO_2 positive (i.e. rods instead of pores). These rods however, appeared shorter than the depth of the shallow pores, as no surface roughness was visible in sections of film standing on edge. Although a strategy for fabricating taller rods was devised, it was not implemented because of the dimensions of the final product. Given the Synkera Tech. AAO, which possesses thin pore walls and relatively high packing efficiency, the negative of the structure, with TiO_2 rods in place of the pores, leaves very little space for light-harvesting nanocrystals and ITO. Representative SEM images of these TiO_2 rods are shown in Fig. 6.

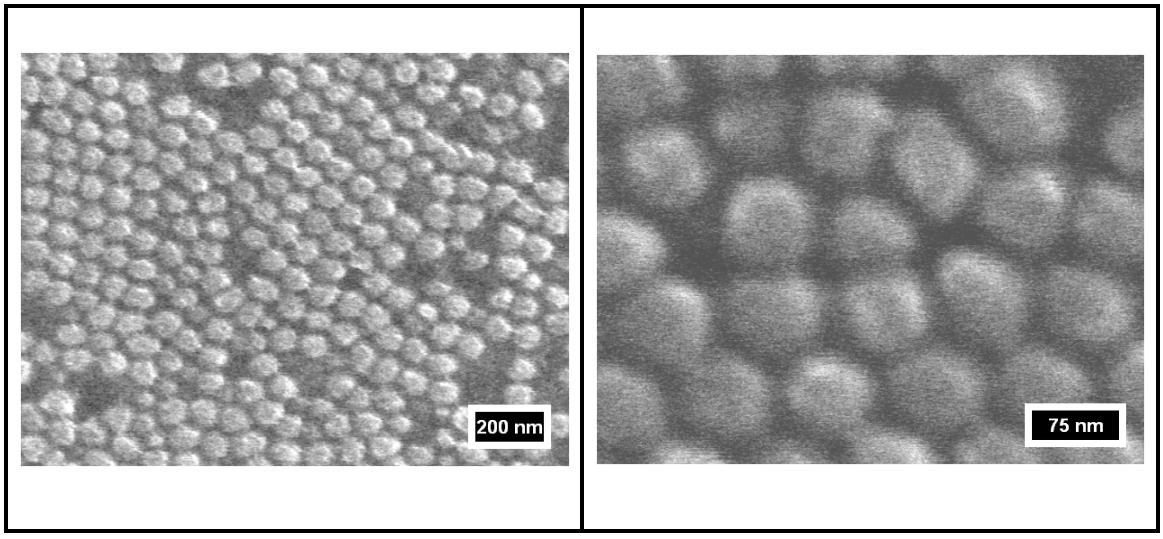

Figure 6: SEM of TiO_2 positive rods. Typical plan-view SEM of TiO_2 rods synthesized by spin casting the TiO_2 sol-gel directly onto the AAO template. When viewed from the side (not pictured) these rods were less than 25 to 50 nm in height.

XRD characterization of the embossed TiO_2 was performed on both the as-synthesized film on the Si substrate, and after being scraped off the substrate as powder. In agreement with the report of Goh *et al.*, the (101) peak of anatase TiO_2 was repeatedly observed at ~25.3° 2θ in the powder samples. Given the thermal treatment of the sol-gel TiO_2 embossed film, the presence of anatase was to be expected. The anatase nanocrystallite domain size was calculated according to the modified Scherrer's equation, $d=(4/3)K\lambda/(\beta\cos\theta_b)$,[87] to be 31.8 nm. XRD traces from two successful samples are shown in Fig. 7 above the powder diffraction file (PDF) peaks associated with pure anatase and pure rutile TiO_2. It is noted that the relatively weak signal of the anatase peak above the background is consistent with the small fraction of crystalline material present in the powder; in fact, early reports of semicrystalline meso-nc-TiO_2, while visible with HRTEM were not initially verified with XRD.[45,92]

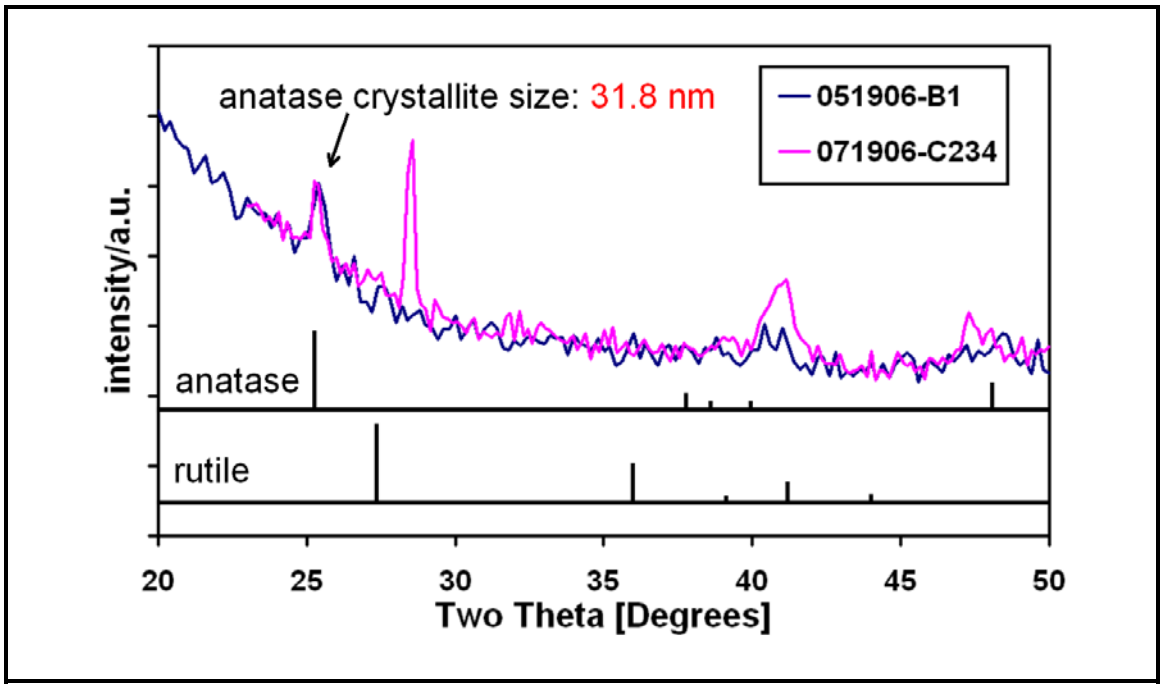

Figure 7: XRD of embossed TiO_2. XRD traces of embossed TiO_2 samples scraped off their substrates as powder. Bulk anatase and rutile TiO_2 diffraction peak locations and relative intensities are shown as well. The anatase crystallite size was calculated according to the modified Scherrer's equation to be 31.8 nm.

Although the Goh *et al.* synthesis of ~120 nm deep pores was ultimately unsuccessful, the fabrication of shallow pores serendipitously had a significant impact. Because TEM and Z-STEM require sample thicknesses in the tens of nanometers range, a thin film with shallow pores proved very useful. Transverse TEM sample preparation can be fairly tedious, and permits imaging of the film's cross-section only. Plan view imaging is only possible if the entire thickness of the sample (pore wall height plus the film beneath) is kept below ~50 nm.[93] Additionally, as the embossed TiO_2 was functionalized with light harvesting nanocrystals, plan view imaging of unsectioned samples helped with the chemical self-assembly fabrication effort.

Sixteen trials were run in order to reproducibly fabricate thin films with shallow pores. Returning to the original process, TiO_2 film thickness is determined during the

spin coating of the TiO_2 sol-gel onto the polymer mold. Although a variety of experimental variables were considered, variation of spin coating speed was ultimately chosen as the most effective and repeatable. Unfortunately, if the spin coating speed was above ~3500 r.p.m., not enough liquid sol-gel remained on the polymer mold to adhere it to the substrate (typically silicon); ultimately, a spin coating speed of 3000 r.p.m. produced the best films. As noted above, according to Goh *et al.* TiO_2 films thicker than ~150 nm cracked due to tensile stress induced during condensation,[42] as seen from early examples of our material in Fig. 8 (left) which were sometimes as thick as 0.5 to 1 μm. However, spin coating at 3000 r.p.m. reduced the film thickness to ~100 nm, and produced areas of crack-free films as large as ~100 μm^2, as seen in Fig. 8 (right).

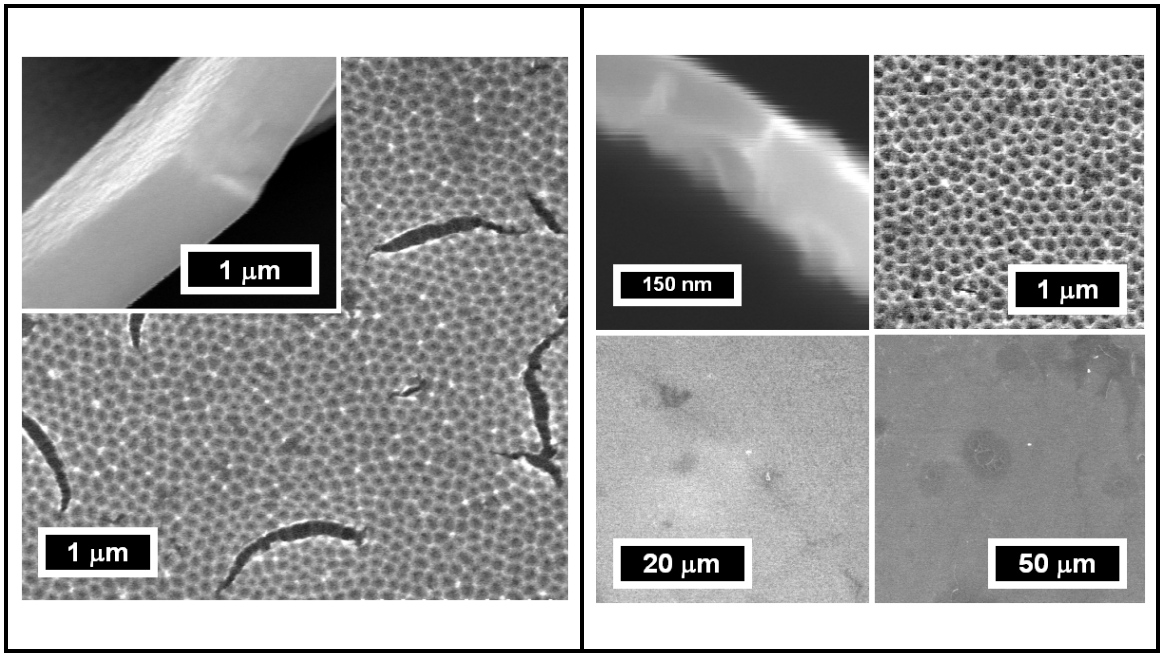

Figure 8: SEM of cracked and crack-free embossed TiO_2. Left: Early example of embossed TiO_2 film with cracks produced during condensation due to the film thickness exceeding ~150 nm, as seen from the inset. Right: Embossed TiO_2 films ~100 nm thick (upper left) had many large crack-free regions.

Embossed Sol-Gel TiO_2 with Electrophoretically Deposited CdSe

Nathanael Smith and Kevin Emmett were responsible for developing the procedure for electrophoretic deposition (EPD) of nanocrystals onto the embossed TiO_2 films, and performed many of the depositions used in this work. Initially, embossed TiO_2 films with electrophoretically deposited CdSe were examined in the SEM to determine if the depositions had been successful. Although individual CdSe nanocrystals are too small to be imaged using the SEM, it was immediately apparent that something had been deposited onto the TiO_2. Comparing the embossed TiO_2 seen above in Fig. 5 to that seen in Fig. 9 (after EPD), once can clearly discern the presence of a layer above the embossed TiO_2 substrate. The composition of this layer is likely a mixture of CdSe nanocrystals and the organic surfactants in which they are synthesized. The electron beam, when focused on these samples, produced a residual dark region as seen in the center of Fig. 9 (lower right). This was likely evidence of charging, as the beam interacted with deposited organic surfactants, an effect that was never seen in the as-synthesized embossed TiO_2 films. Ultimately, the deposition of CdSe nanocrystals by EPD was confirmed by Nathanael Smith who performed RBS on various samples; however deposition was not always successful and was found to depend on nanocrystal cleanliness.[94]

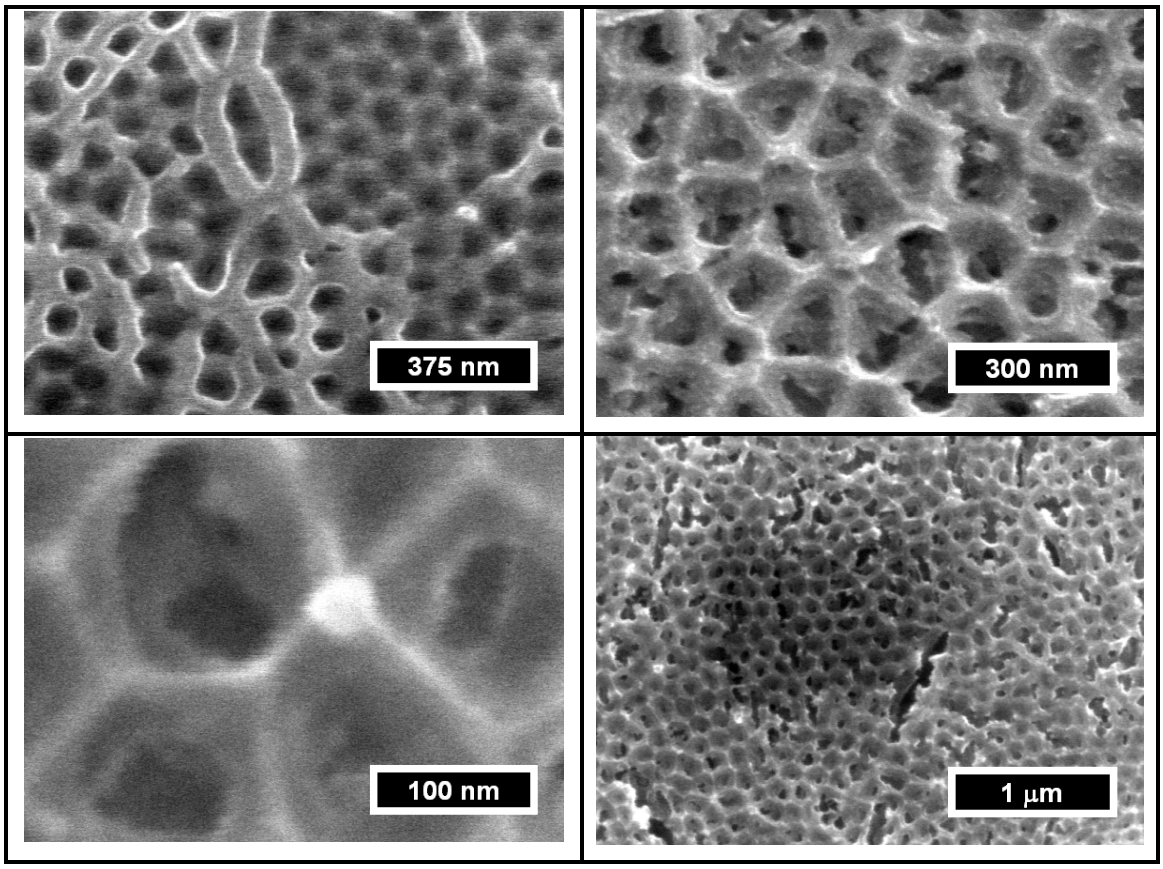

Figure 9: SEM of embossed TiO_2 with electrophoretically deposited CdSe. Upper Left and Right: Representative embossed TiO_2 films after EPD of CdSe nanocrystals. Lower Left: High magnification of embossed TiO_2 pores after EPD. Lower Right: Embossed TiO_2 film after EPD showing a residual dark region in the center of the image, which is likely charging due to the presence of deposited organic surfactants.

Some embossed TiO_2 films after EPD were scraped off their substrates for imaging in the VG603 STEM. Representative low magnification annular dark field (ADF) images are shown in Fig. 10; on the left, three complete pores (dark circles) and one incomplete pore are decorated with CdSe nanocrystals (bright white spots), and on the right, one individual pore (large dark circle) is filled with a handful of nanocrystals. Figure 10 (right) highlights one of the primary difficulties in imaging CdSe nanocrystals in TiO_2 pores; excess organic surfactants from the CdSe synthesis, which are deposited along with the nanocrystals during EPD, build up under illumination by the electron

beam, blurring the final image. In pure nanocrystal samples, this contamination can sometimes be removed by heating in air and under vacuum, allowing for atomic resolution, while in the composite material this organic contamination is likely fixed in place.

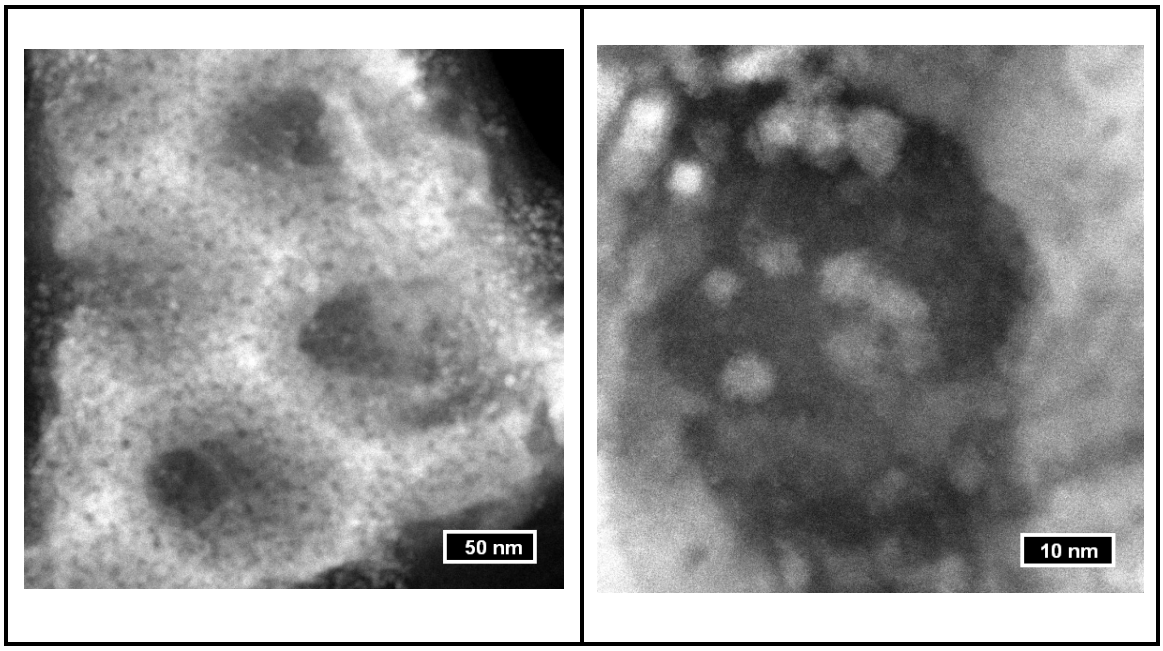

Figure 10: Z-STEM of embossed TiO_2 with electrophoretically deposited CdSe. Left: Complete pores (dark circles) are decorated with CdSe nanocrystals (bright white spots). Right: One individual pore (large dark circle) is filled with a handful of nanocrystals. Contamination from excess organic surfactants obscures the nanocrystal atomic columns.

Another source of difficulty in imaging with Z-STEM is the competing effects of atomic number contrast and thickness contrast. Atomic number contrast, which is a result of collecting the widely scattered electrons using a high-angle annular dark field (HAADF) detector, causes heavier atoms (and atomic columns) to appear brighter in the ADF images. In our samples the Cd and Se atoms within the CdSe nanocrystals should appear roughly twice as bright as the Ti atoms of the TiO_2 substrate.[75] Thickness contrast,

which is a result of increased interaction (scattering) through thicker regions, causes those thicker regions to appear brighter in the ADF images.

The competing effects of these two sources of contrast are shown in the ADF and bright field (BF) images in Fig. 11. In the ADF image the large dark circular region is the pore itself (where the beam has to pass through less TiO_2), and the "halo" surrounding the pore is the thicker pore wall, which is brighter due to thickness contrast. The two small bright spots within the pore are almost certainly CdSe nanocrystals considering that they are almost as bright as the pore walls. In the simultaneously collected BF image, moiré patterns (produced as the electron beam travels through multiple misoriented anatase nanocrystallites) are visible throughout the pore wall region. Within the pore itself, both lattice fringes and moiré patterns result from the CdSe nanocrystals and the anatase nanocrystallites. Recall that meso-nc-TiO_2 is comprised of anatase TiO_2 nanocrystallites in an amorphous TiO_2 matrix; the latter is detectable in the pore itself by the absence of fringes in some areas. It is noted that the BF image is a phase contrast image; therefore nanocrystals at different heights show up in the image, as opposed to the ADF image in which only nanocrystals at the defocus height (i.e. in focus) appear.

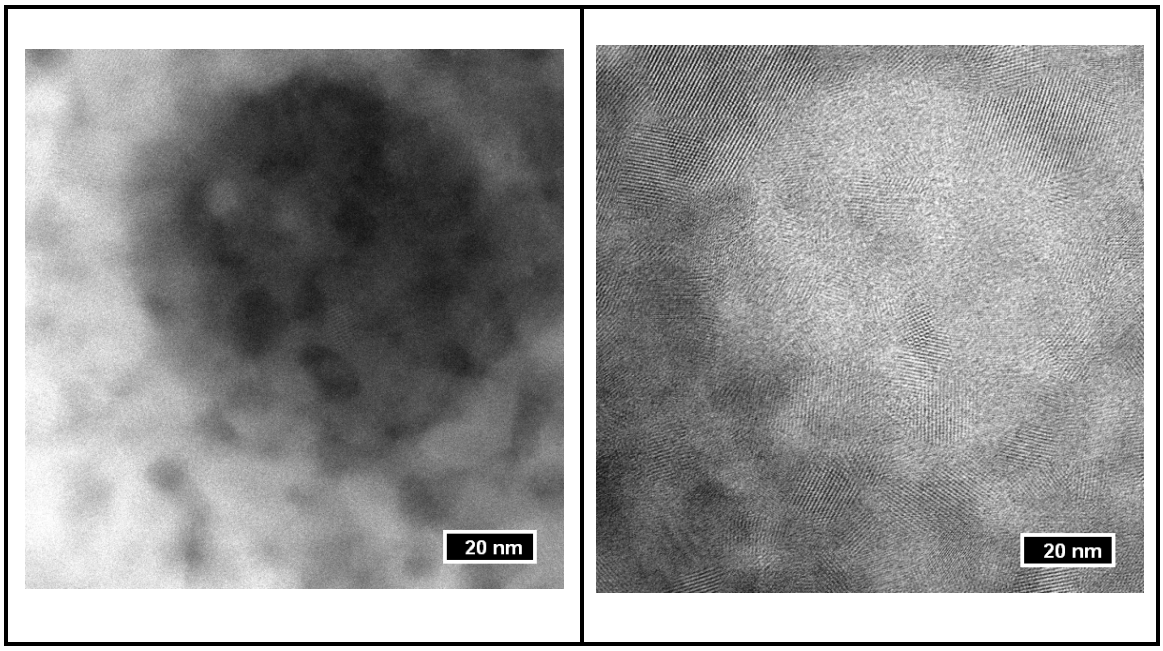

Figure 11: Competing contrast from ADF and BF imaging. Left: Z-STEM annular dark field (ADF) image. Right: Simultaneously collected bright field (BF) image. See text for a description of the competing effects of atomic number contrast and thickness contrast.

In addition to the aforementioned difficulties in imaging, depositing too many CdSe nanocrystals during EPD resulted in poorly resolved images. The ADF images in Fig. 12 show excess CdSe nanocrystals both within the pore as wall as on top of the pore wall. Depositing this many CdSe nanocrystals also introduced further excess organic surfactants, obscuring the images further.

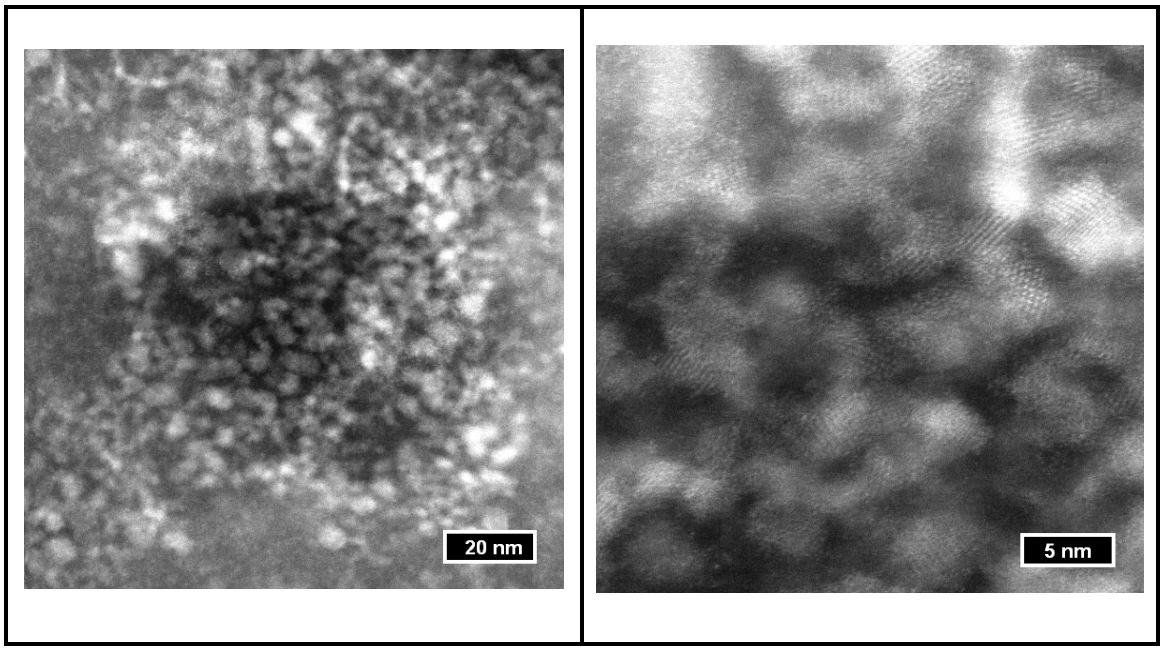

Figure 12: Z-STEM of excess deposited CdSe nanocrystals. Representative images of embossed TiO_2 pores with too many CdSe nanocrystals deposited via EPD.

At the boundary of the pore and pore wall, Fig. 13 shows a large nanocrystal, which is possibly anatase TiO_2. The lattice fringes (possibly moiré patterns) cannot be unambiguously assigned to anatase TiO_2, however the relative similarity in brightness between the nanocrystal and the crystalline matrix surrounding it support this contention. In contrast, the large nanocrystal shown in Fig. 14 is more likely CdSe. In this case, the nanocrystal appears significantly brighter than the pore in which it resides. Furthermore, the tiny bright spots near the nanocrystal in Fig. 14 (right) are almost certainly Cd or Se single atoms; these single atoms are probably unreacted precursors bound up in the organic surfactants covering the nanocrystal surface. It should be noted however, that if the nanocrystal in Fig. 14 is in fact CdSe, it is an outlier - much larger than the average CdSe nanocrystals deposited in this sample (typically 2-3 nm).

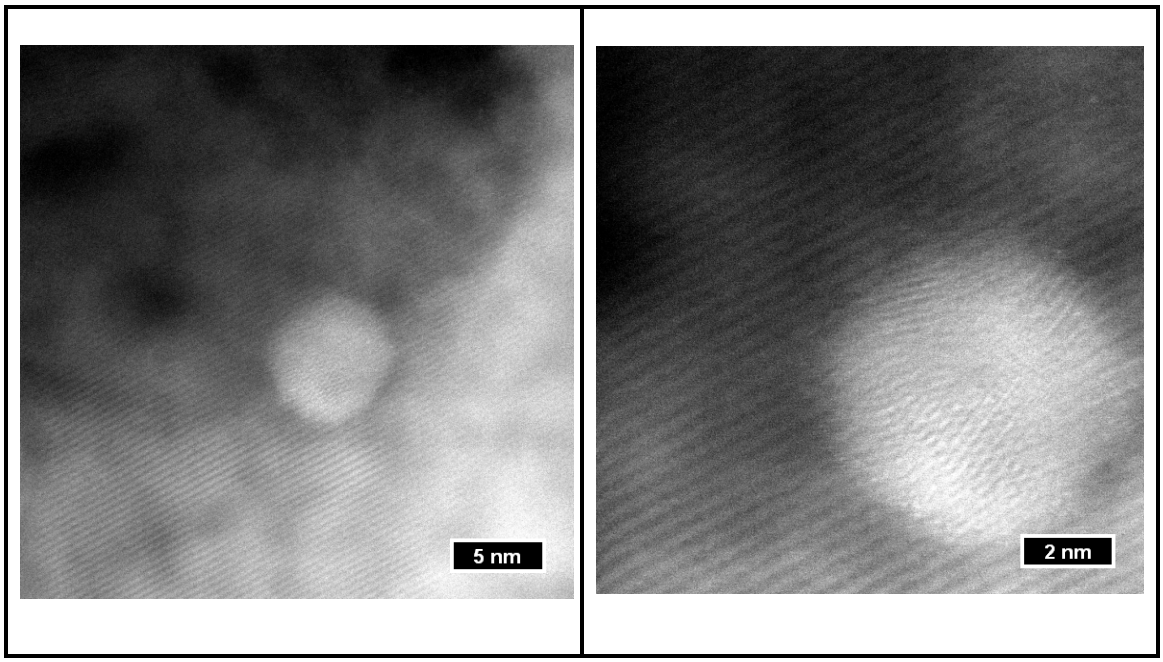

Figure 13: Z-STEM of possible TiO_2 nanocrystal.

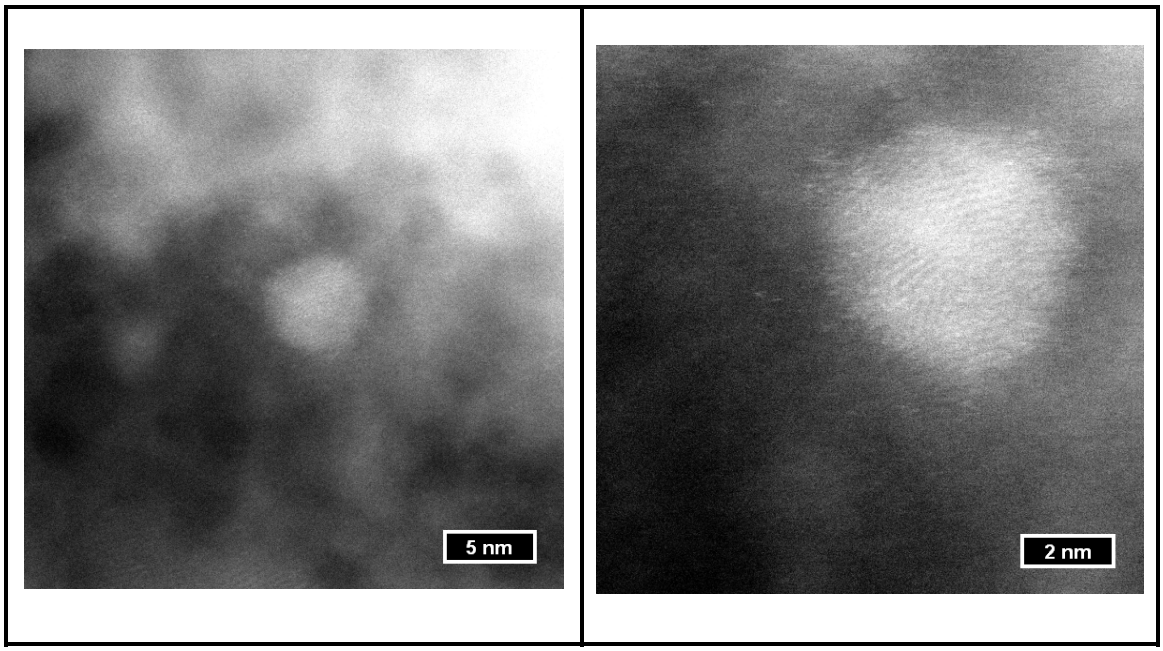

Figure 14: Z-STEM of probable CdSe nanocrystal.

Z-STEM of TiO_2 Nanotubes

Nathanael Smith and Kevin Emmett were also responsible for developing the procedure for anodizing Ti foils to form TiO_2 nanotubes, and produced all of the TiO_2 nanotubes used in this work. TiO_2 nanotube arrays were scraped from their substrates and imaged using the VG603 STEM, as seen in Fig. 15. At the nanotube ends, where the tubes are broken unevenly, the beam passes through only one side of the nanotube wall (instead of both walls of the intact tube), and examples of these regions are shown at higher magnification in Fig. 16. As in Fig. 15, the dark spots are thinner regions of the nanotube walls. Although an attempt was made to deposit CdSe nanocrystals via EPD into these nanotubes, these images show that it was unsuccessful. This ineffectiveness can be accounted for by the lack of cleanliness of the CdSe nanocrystals, as well as the length of these nanotubes in comparison to the shallow pores of the embossed TiO_2.

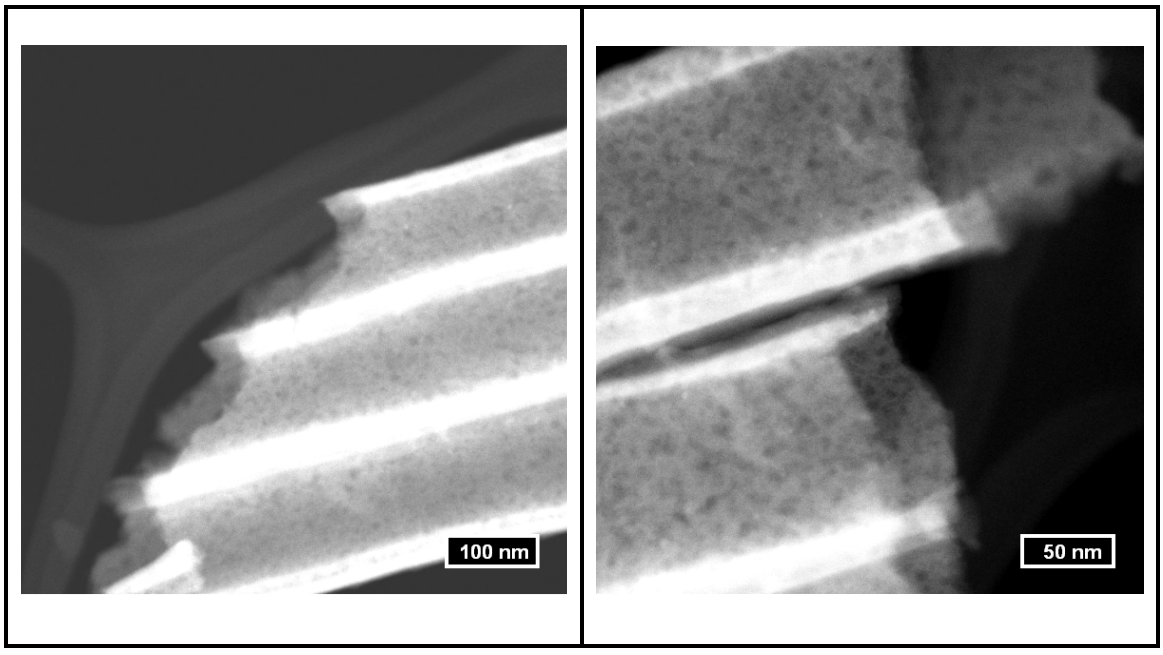

Figure 15: Z-STEM of TiO_2 nanotubes.

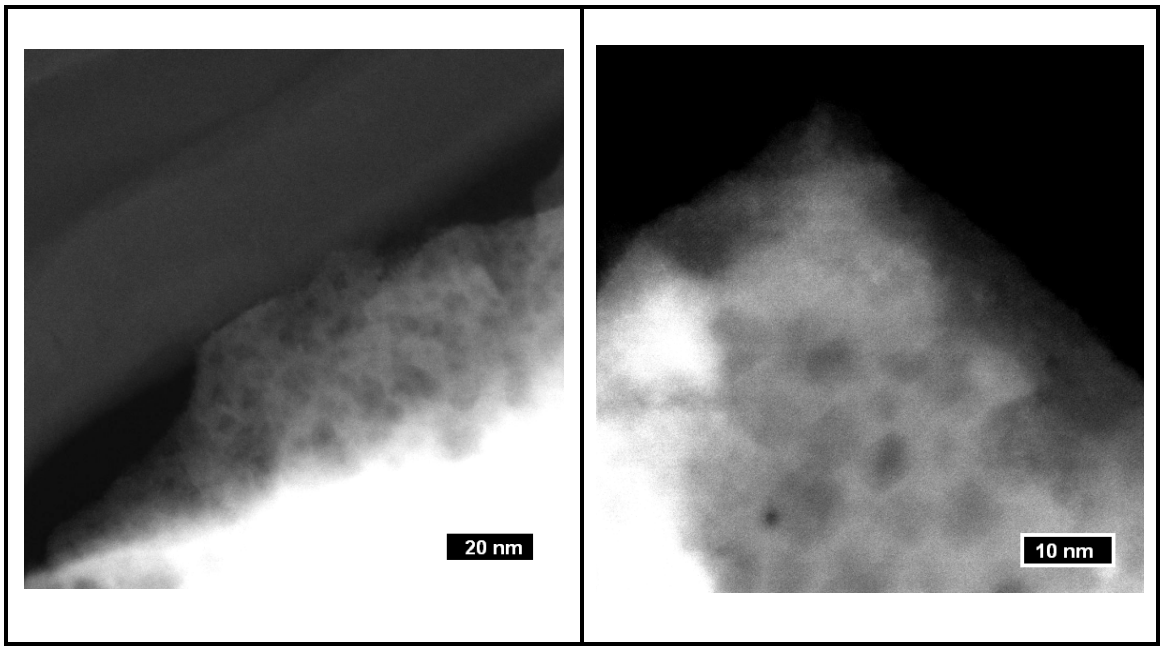

Figure 16: Z-STEM of TiO_2 nanotube walls.

Z-STEM of TiO_2 Nanotubes with Electrophoretically Deposited CdSe

Cleaner CdSe nanocrystals were successfully deposited in TiO_2 nanotubes, as confirmed by Nathanael Smith via RBS. Transverse samples were etched with HF and thinned with an ion mill by Julia Luck of Steve Pennycook's STEM group at ORNL. A low magnification BF image of an array of TiO_2 nanotubes is shown in Fig. 17 (left); BF thickness contrast is the inverse of ADF thickness contrast, therefore the darker regions are the thicker (taller) sections of nanotubes. An ADF image of a thin portion of a nanotube wall is shown in Fig. 17 (right); the brighter band is the thicker (taller) portion of the nanotube wall, while the darker band is likely the base of the nanotube.

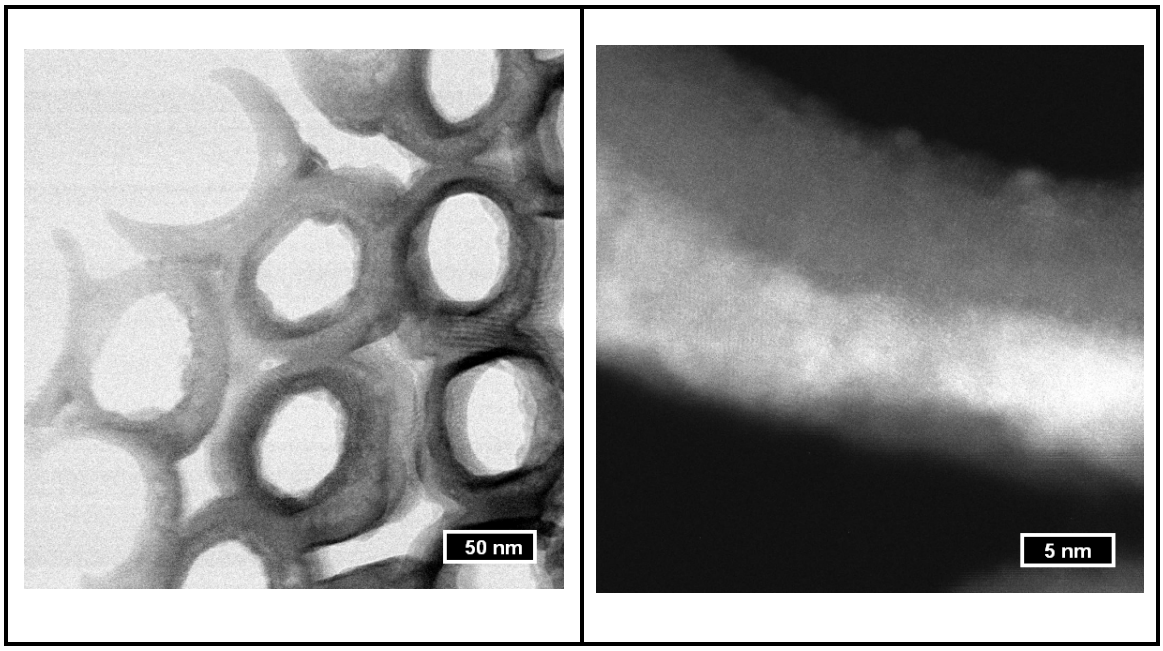

Figure 17: BF and ADF plan-view images of TiO_2 nanotubes. Left: Transverse BF image of thinned TiO_2 nanotube array. Darker nanotubes (lower right) are thicker than lighter nanotubes (center); partial nanotubes (upper left) are thinned completely. Right: Transverse ADF image of completely thinned (partial) TiO_2 nanotube. Brighter band is the nanotube wall, while the darker band is likely the base of the nanotube.

Transverse ADF and BF images of a completely thinned (partial) TiO_2 nanotube are shown in Fig. 18. In the ADF image (left), the bright regions are possibly CdSe nanocrystals, particularly those with clear fringes. Lattice fringes in the BF image (right) are also visible and correspond well with the bright regions in the ADF image. Unfortunately, a more convincing image showing a probable CdSe nanocrystal on a thinned nanotube was lost due to a computer crash. In this image, a very thin partial nanotube contained a quite bright nanocrystal, whose brightness could not be accounted by thickness contrast alone, given the thinness of the nanotube wall.

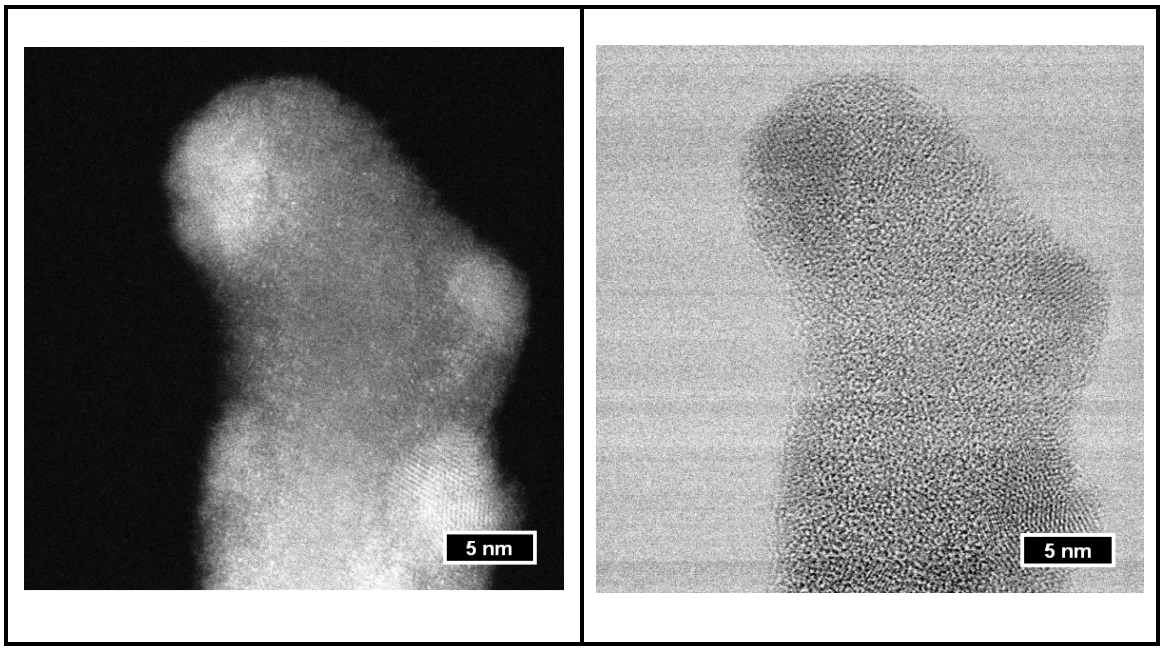

Figure 18: ADF and BF of thinned TiO_2 nanotube wall. Left: Transverse ADF image of completely thinned (partial) TiO_2 nanotube showing possible CdSe nanocrystals (bright regions) Right: Corresponding transverse BF image showing lattice fringes. An image of a thinner partial nanotube with a brighter nanocrystal, almost certainly CdSe, was lost due to a computer crash.

CHAPTER V

Z-STEM IMAGING OF VARIOUS NANOCRYSTAL SYSTEMS

Ultra-small White-light Emitting CdSe Nanocrystals

Recently within the Rosenthal group, we have synthesized monodisperse, ultra-small CdSe nanocrystals. Contrary to predicted behavior, these ~1.5 nm diameter nanocrystals emit very pure, broad-spectrum white light.[95] These nanocrystals offer an exciting new possibility for white-light emitting diodes (LEDs) in energy efficient solid-state lighting. Preliminary results using these nanocrystals as nanophosphors have yielded devices exhibiting near pure white CIE coordinates of 0.324, 0.322 and an extraordinary color rendering index of 93, which already exceeds the Department of Energy's 2025 goal.[96] In order to realize the potential of ultra-small CdSe for white solid-state lighting, a thorough understanding of the fundamental structure of these ultra-small nanocrystals is needed.

In contrast to large CdSe nanocrystals (2-8 nm in diameter), which have been extensively studied and are well understood, there has been little research to date on the properties of ultra-small nanocrystals (1-2 nm in diameter) due to the lack of a reliable synthetic method to produce high quality nanocrystals in large quantities in this size regime. Due to their small size, however, conventional TEM cannot resolve these ultra-small nanocrystals, and both the Titan and the VG603 were used in attempts to image them. Since the emission spectrum of this material has never been seen before, it was not clear that they would be similar in structure to larger, monochromatic nanocrystals.

Theoretical work in the literature has predicted several different structures for CdSe in this size regime, ranging from planar structures of 15 atoms to cage structures of 62 atoms.[97,98]

Roughly half a dozen attempts to image these ultra-small nanocrystals were made, only one of which was successful. Obviously then, there were a variety of difficulties in imaging these nanocrystals. One possibility was that the ultra-small nanocrystals were not comprised of a regular crystalline lattice, or that there were not enough atoms to form a recognizable structure. Another possibility was that the nanocrystals were rotating under the electron beam, or being damaged or even destroyed when illuminated. Thus it was not clear if the nanocrystals were suitable for high-resolution imaging, or if the microscopes themselves were capable of imaging them.

Ultimately, we were able to collect the first lattice-resolved images of nanocrystals in this size regime using the Titan, the best of which is shown in Fig. 19 (left). Two nanocrystals in particular are blown up in the inset and in Fig. 19A. Although it is difficult to discern the lattice planes in these images, they were unmistakable when viewed in the microscope, where one can move the field of view around and any regular pattern (in this case lattice fringes) stands out against the amorphous background. This suggests that the nanocrystals have reasonably defined lattice planes, which appear to be wurtzite in structure, with a diameter of approximately 1.5 nm; a theoretical ball and stick model is shown in Fig. 19B. These nanocrystals are composed almost exclusively of surface atoms and their irregular lattice spacing suggests the presence of defects, both of which provide sites for charge trapping to occur. The existence of a wide variety of trap sites leads to the possibility of many energetically different states from which

recombination can occur, giving rise to the broad-spectrum white-light emission.[95] It is noted, that the surface of these nanocrystals appear to be lacking an oxide coating, which is almost always found on larger nanocrystals.[37,39-41]

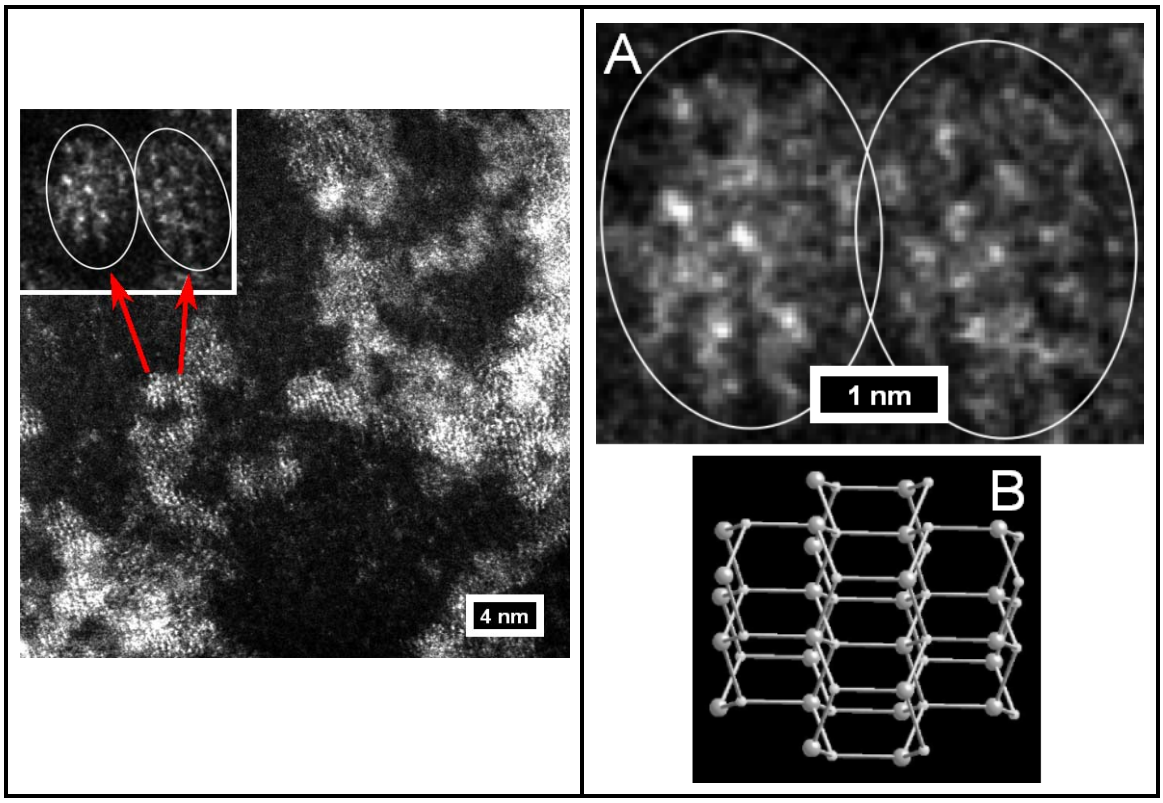

Figure 19: Z-STEM of ultra-small CdSe nanocrystals. Left: Lattice-resolved image of ultra-small white-light emitting CdSe nanocrystals. Red arrows point to a magnification of two nanocrystals in particular shown in the inset. A: Further magnification of two nanocrystals showing four lattice planes each. B: Theoretical ball and stick model of a four lattice plane wurtzite nanocrystal (courtesy of James McBride).

XRD traces of six small (1-2 nm in diameter) nanocrystal samples, ranging from 415 nm-absorbing to 450 nm-absorbing CdSe, are shown in Fig. 20 along with the PDF peaks for wurtzite CdSe. These XRD traces are consistent with earlier reports of nanocrystal XRD spectra, such as that from Murray *et al*.[11] The nanocrystallite domain size could not be calculated with the modified Scherrer's equation due to the extensive

peak broadening resulting from the small size of these nanocrystals. Traces A and B, 417 nm-absorbing and 415 nm-absorbing CdSe respectively, are from two samples of functionally equivalent ultra-small white-light emitting nanocrystals. Trace A was restricted to the range of 35 to 60° 2θ in an effort to capture the three strong peaks at 42.0°, 45.8° and 49.7° 2θ in the wurtzite CdSe PDF. The XRD traces in Fig. 20, along with the magnification of Trace A in Fig. 21, highlight how significantly the PDF peaks broaden for the smallest nanocrystals. Unfortunately, increasing the duration of the scan or the concentration the nanocrystals in the sample will not produce more distinguishable peaks.

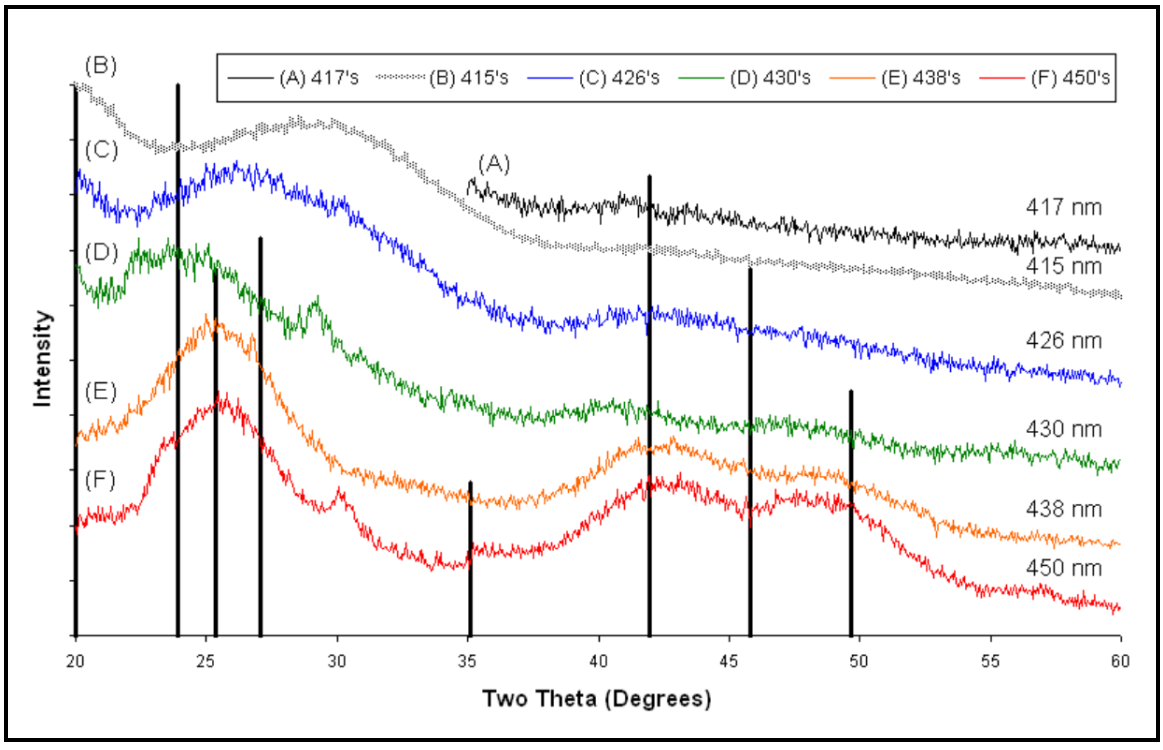

Figure 20: XRD of small CdSe nanocrystals. XRD traces of small CdSe nanocrystals ranging from ~1.5 to ~2 nm in diameter. Bulk wurtzite CdSe diffraction peak locations and relative intensities are shown as well. The modified Scherrer's equation could not be used to calculate the various crystallite sizes due to extensive peak broadening.

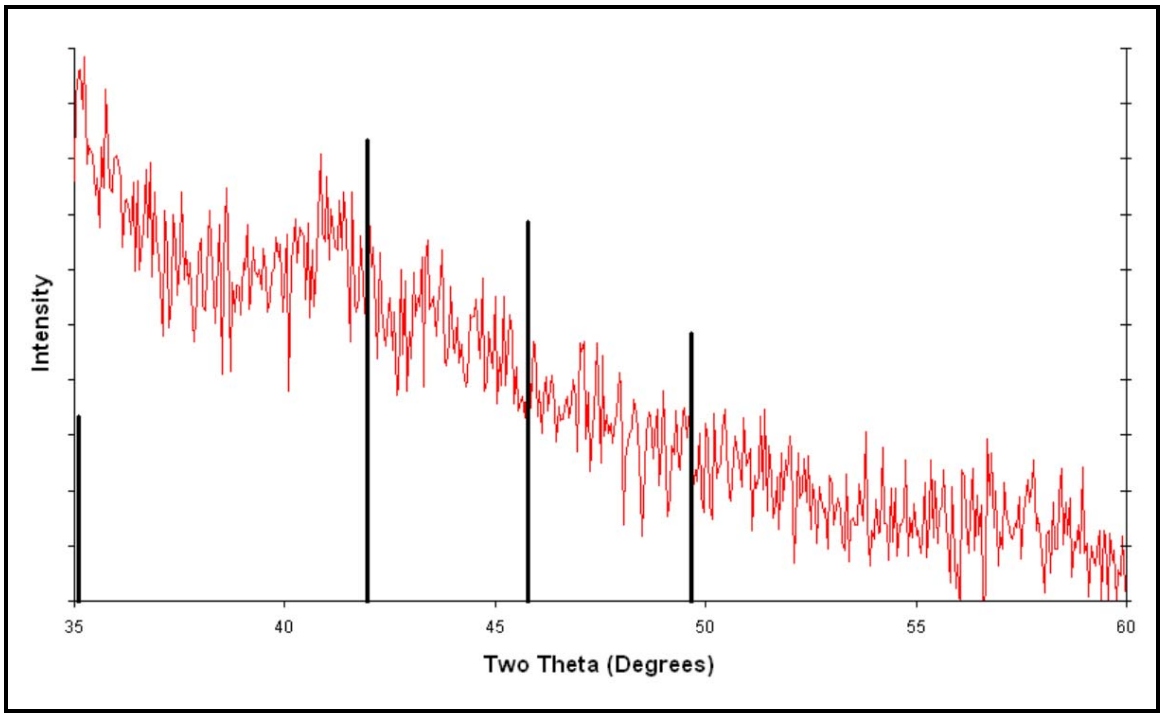

Figure 21: XRD of ultra-small CdSe nanocrystals. XRD trace of 417 nm-absorbing ultra-small white-light emitting CdSe nanocrystals. Bulk wurtzite CdSe diffraction peak locations and relative intensities are shown as well.

CdSe Nanocrystals of Various Sizes

Along with the effort to image ultra-small nanocrystals, CdSe nanocrystals in a variety of sizes were imaged using both the VG603 and the Titan. Nanocrystals in these sizes have been imaged previously, primarily with the TEM, and some of these images have been used to produce sizing curves relating absorption wavelength to nanocrystal diameter.[99] The primary drawback in sizing with the TEM however is that coherent, phase contrast imaging does not give actual atomic positions and therefore can only give an approximation of the surface. In the case of the small nanocrystals (below ~2 nm in diameter), TEM sizing becomes increasingly unreliable as fewer lattice planes are involved in forming the image. In contrast, incoherent imaging in the Z-STEM,

particularly with aberration-corrected atomic-scale resolution, can be used to measure exact nanocrystal dimensions.

Figures 22, 23 and 24 are the highest quality images from various samples of 486 nm-, 530 nm- and 581 nm-absorbing CdSe nanocrystals respectively. According to Yu *et al.*, these first absorption peak positions correspond to nanocrystal diameters of ~2 nm, ~2.5 nm and ~3.8 nm respectively.[99] These nanocrystals were synthesized at Vanderbilt by James McBride and Albert Dukes. Unfortunately, due to a variety of difficulties, primarily sample cleanliness, only a statistically insignificant number of nanocrystals were imaged in each size regime.

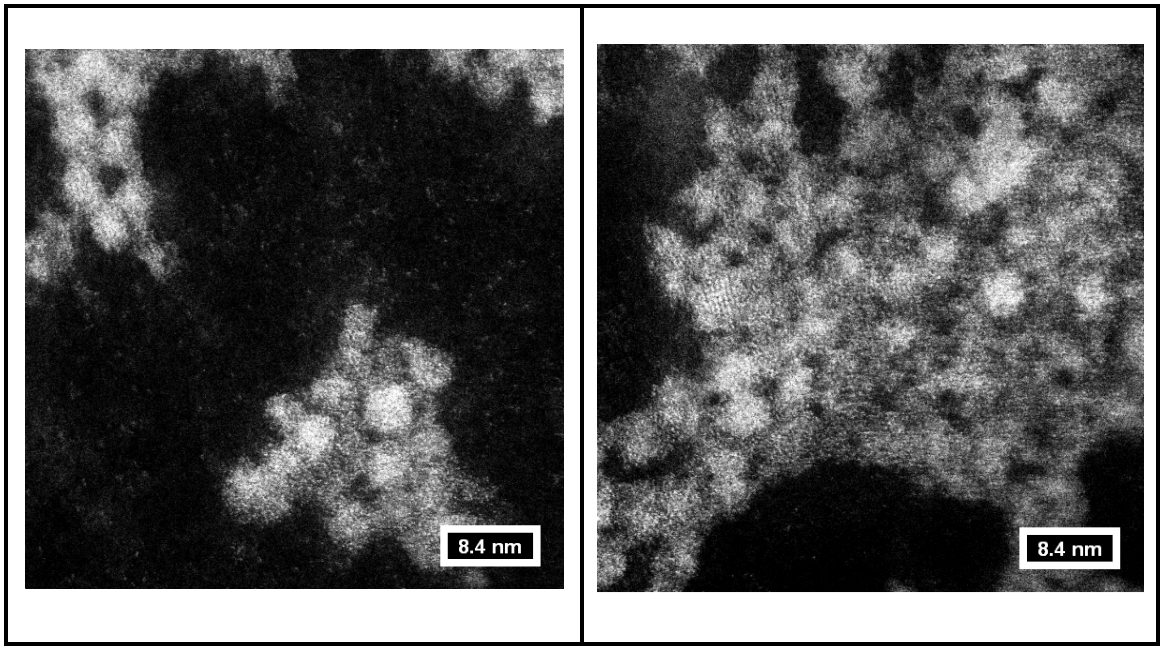

Figure 22: Z-STEM of 486 nm-absorbing CdSe nanocrystals. Lattice fringes are barely visible in these images; from their shape, size can be estimated, but not their structure.

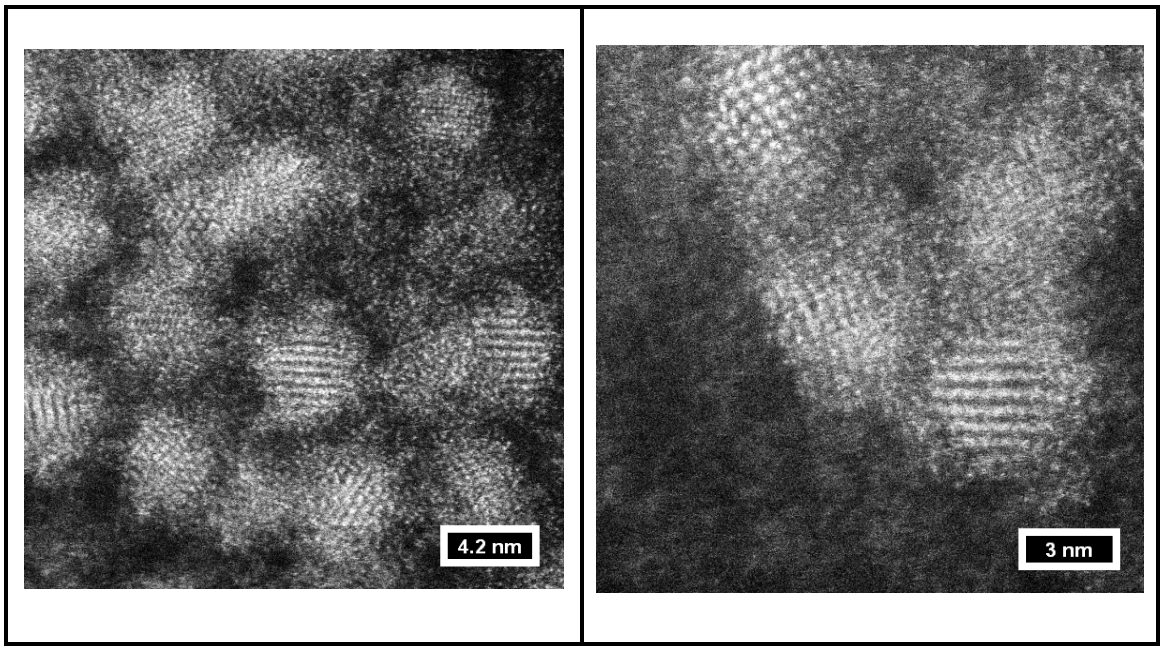

Figure 23: Z-STEM of 530 nm-absorbing CdSe nanocrystals. Lattice fringes are clearly discernable in these images, and even atomic-resolution dumbbells (atomic columns of Cd and Se atoms) are visible in the uppermost nanocrystal in Fig. 23 (right).

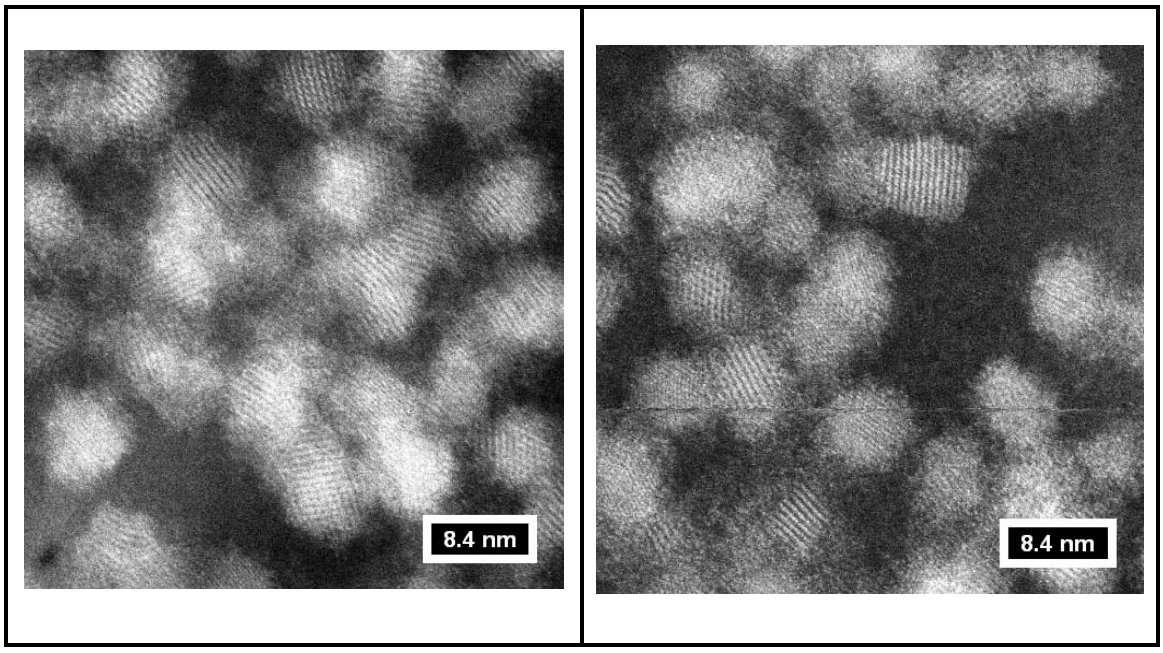

Figure 24: Z-STEM of 581 nm-absorbing CdSe nanocrystals. Lattice fringes and nanocrystal surfaces are clearly visible, however no atomic-resolution dumbbells are discernable.

XRD traces of four large nanocrystal samples, ranging from 595 nm-absorbing to 660 nm-absorbing CdSe, are shown in Fig. 25 along with the PDF peaks for wurtzite CdSe. According to Yu *et al.*, the first absorption peak positions of 595 nm, 610 nm, 645 nm and 660 nm, correspond to nanocrystal diameters of ~4.5 nm, ~5.0 nm, ~7.8 nm and ~8.3 nm respectively.[99] Again, these XRD traces are consistent with Murray *et al.*'s report of nanocrystal XRD spectra,[11] and the nanocrystallite domain size could not be calculated due to peak broadening.

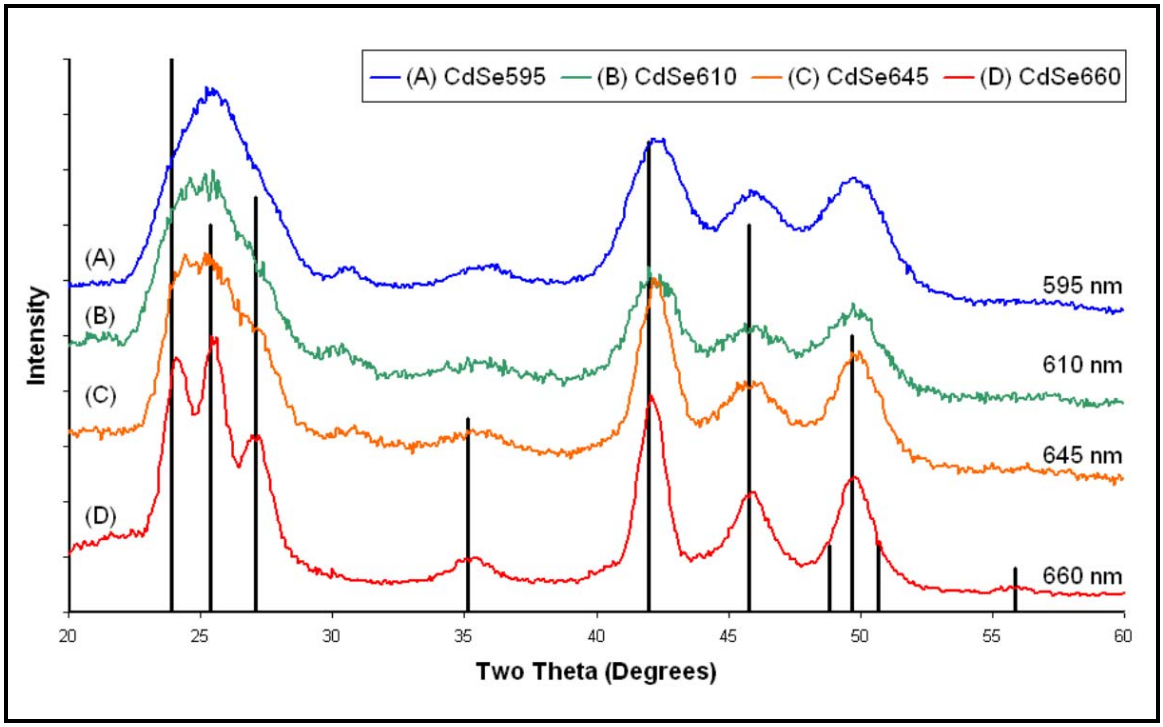

Figure 25: XRD of large CdSe nanocrystals. XRD traces of large CdSe nanocrystals (~4.5 nm to ~8.3 nm in diameter). Bulk wurtzite CdSe diffraction peak locations and relative intensities are shown as well. The modified Scherrer's equation could not be used to calculate the various crystallite sizes due to peak broadening.

Inverse Core/Shell PbS/PbSe Nanocrystals

As mentioned above, Pb-containing nanocrystals have been envisioned for inclusion in our photovoltaic devices. In addition to harvesting nearly the entire solar spectrum,[6] they may benefit from the potentially paradigm-shifting impact of carrier multiplication.[21,22] An inverse core/shell architecture of PbS/PbSe will further localize charge carriers in the shell, where they are less likely to recombine.[8] Danielle Garrett has successfully synthesized these inverse core/shell PbS/PbSe nanocrystals, and the best representative Z-STEM images (taken with the Titan) are shown in Fig. 26. Although atomic-resolution dumbbells are barely visible in the central nanocrystal in Fig. 26 (right), there is no discernable indication of a separate core and shell, as seen in CdSe/ZnS core/shell nanocrystals.[41]

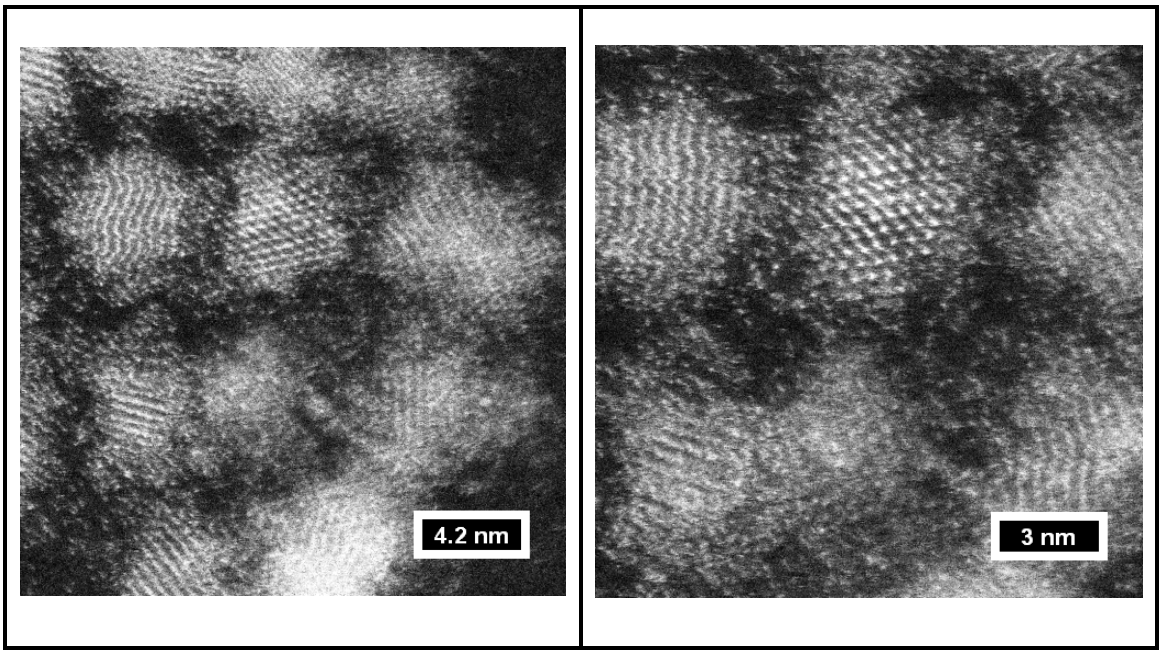

Figure 26: Z-STEM of inverse core/shell PbS/PbSe nanocrystals. Lattice fringes are clearly discernable in these images, however even though atomic-resolution dumbbells are visible in the central nanocrystal in Fig. 26 (right), there is no clear demarcation between core and shell, as seen in CdSe/ZnS core/shell nanocrystals.

CHAPTER VI

CONCLUSION

The Rosenthal group has been researching a next-generation photovoltaic device that relies on a nanocrystalline anatase framework, ideally with vertically aligned mesopores. This framework was initially produced via an ABC-based synthesis, followed by embossing of TiO_2 sol-gels, and finally by anodization of Ti foils into arrays of TiO_2 nanotubes. CdSe nanocrystals were deposited via EPD on to the latter two materials, with the TiO_2 nanotube arrays ultimately preferred. A variety of TiO_2 samples, including those with deposited CdSe nanocrystals, were characterized using SEM, TEM, XRD, RBS and Z-STEM; much of this characterization is the first of its kind for these materials. The synthesis and characterization of these materials represents a significant milestone in the fabrication of our next-generation photovoltaic devices.

Furthermore, Z-STEM was used to image a variety of nanocrystal systems, producing the first images of ultra-small white-light emitting CdSe nanocrystals. Although the diameter of the ultra-small CdSe nanocrystals could not be confirmed, the imaging of these novel white-light emitting nanocrystals is fundamental transformational research. Knowing the structure will aid in our understanding of the origin of these nanocrystals' broad emission and also further our understanding of the early stages of nanocrystal growth. In addition to opening new avenues for fundamental research, understanding these white-light emitting nanocrystals will aid in the development of a solid-state white-light source suitable for commercial and residential use.

CHAPTER VII

FUTURE WORK

Z-STEM with Electron Energy Loss Spectrometry

Z-STEM imaging measures only the portion of the transmitted electron beam that is scattered to high angles, via the HAADF detector, therefore the remaining low-angle (forward) scattered electrons can be simultaneously employed for high resolution electron energy loss spectrometry (EELS).[100-102] An EELS spectrum results from the energy loss associated with the inelastic scattering of the transmitted beam by plasmons, valence electrons, and inner-shell electrons (in order of increasing energy loss) and can therefore be used to determine chemical composition, significantly of elements lighter than oxygen, atomic arrangement, chemical bonding and electronic structure,[68,70,93] including possible quantification of charge carriers.[103] The combination of Z-STEM with EELS, when combined with analysis of the fine-detail intensity variations within the energy-loss near-edge structure (ELNES),[70,93,104-108] has been characterized as "arguably the most powerful analytical technique for atomic characterization".[68]

Utilizing the Z-STEM microscopes within Dr. Stephen J. Pennycook's group at ORNL, EELS analysis will be performed on meso-nc-TiO_2, Pb-containing nanocrystals, and meso-nc-TiO_2 functionalized with Pb-containing nanocrystals. Z-STEM with EELS will be used to verify TiO_2 allotrope,[70,105] to compare the nanocrystalline TiO_2 at the pore wall edges with the bulk TiO_2, to determine if there is any stoichiometric

difference,[70,104,107] and to search for the possibility of electronic (trap) states within the band gap, which "would appear as a pre-edge shoulder to the main edge".[13]

Pb-containing nanocrystals may also be suited to Z-STEM with EELS. In the case of PbSe, the presence of lead-rich facets and facet-junctions will be explored; this will help to understand nanocrystal growth and attempt to answer the lingering issue of inverse proportionality of quantum yield to PbSe nanocrystal size.[109] The light-harvesting nanocrystal/TiO_2 interface is known to be a critical factor in overall photovoltaic efficiency; the incorporation of a linker molecule will introduce additional areas for investigation by Z-STEM with EELS. Specifically, the coverage of pore walls with nanocrystals, and corresponding location of linker molecules, the bonding between the constituents, and the resulting electronic structure of the assembled nanostructure will be examined. Successful Z-STEM imaging with simultaneous EELS analysis would be a significant achievement and add to the knowledge base required to fully realize low-cost, high efficiency next generation photovoltaics.

Electron-Beam Induced Current Studies of Nanostructured Photovoltaics

For our nanostructured photovoltaics, the local characterization of charge-collection properties can provide critical information for device optimization. The electron beam in an SEM or TEM can be used to induce charge generation, while simultaneously producing an image; a technique know as electron-beam induced current, or EBIC. SEM-EBIC is one of the standard techniques of mapping local carrier generation efficiency,[110,111] which has been extensively applied to semiconductor solar cells.[112-114] To our knowledge, however, this technique has never been utilized for studies

of photovoltaic materials of more complex architecture, such as our nanostructured photovoltaics. In collaboration with ORNL, we plan to develop the capabilities for SEM-EBIC characterization of complex photovoltaics in order to map local charge collection efficiency in our devices. Simultaneously, we plan to develop the capacity to perform remote EBIC (or REBIC) measurements, described below. Following development of SEM-EBIC (and REBIC), will be the development of TEM-EBIC, ultimately leading to atomic-scale resolution Z-STEM with EBIC.

S. Jesse *et al.* have previously utilized EBIC and related techniques for the characterization of electrical transport properties of nanotube networks with nm-scale resolution.[115] They were able to determine the quality of individual junctions and utilize this information for device development. In collaboration with Stephen Jesse and Sergei Kalinin at ORNL's Center for Nanophase Materials Sciences (CNMS), we propose to build on this expertise and adapt the methods and hardware for studies of our photovoltaics. Initially the contacts will be deposited using optical lithography equipment at the Nanofabrication Research Facility at CNMS. Different contact configurations will be investigated and the optimal sample architecture will be chosen. The Focused Ion Beam instrument at CNMS may also be utilized for precision contact placement. The SEM-EBIC sample holder (for the Hitachi 4700 SEM at ORNL) will be adapted to accommodate the optimized sample geometry. The nanocomposite samples will be investigated by ambient scanning probe microscopy, including topographic measurements and Kelvin probe (Asylum Research MFP-3D) under different illumination conditions to establish photosensitivity.

Mapping of the charge collection efficiency in our nanostructured photovoltaics is to be completed in collaboration with Albina Borisevich (of Steve Pennycook's STEM group at ORNL), Sergei Kalinin and Stephen Jesse on ORNL's Hitachi 4700 SEM. The geometry of SEM-EBIC for conventional solar cells is given in Fig. 27 (left). The contrast arises from the variations in carrier recombination properties. For example, in polycrystalline silicon, the electroactive defects, grain boundaries, and p-n junctions are manifested by the decrease in EBIC signal. In our nanostructured photovoltaics we expect to image a variety of nanostructural elements, as well as compare charge carrier activity between samples. We project that the region immediately within the pore walls should contribute the most charge carriers to the EBIC signal, as this is where the nanocrystal density will be the greatest.

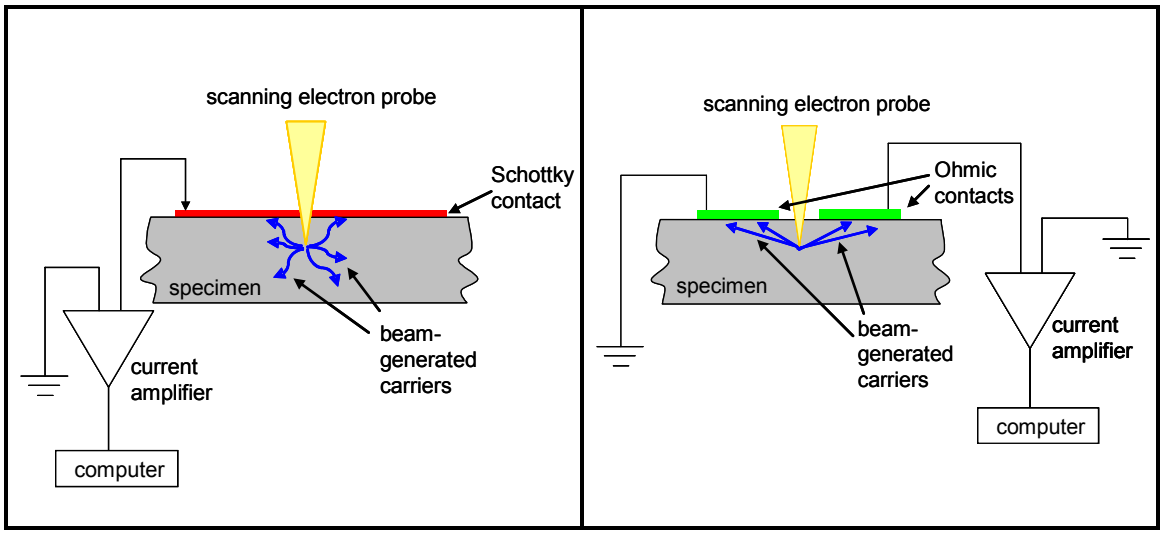

Figure 27: SEM-EBIC and REBIC. Schematic of SEM-EBIC (left) and SEM-REBIC (right) experimental setups.

SEM-REBIC employs slightly different sample geometry than EBIC, as shown below in Fig. 27 (right). The contrast in this case is believed to be related to transport properties and internal fields in the sample. We envision that highly resistive features, such as poorly attached nanocrystals or matrix defects, will produce features on the REBIC images. When bias is applied from the top to the bottom of the sample, we expect that changes in REBIC contrast for different bias values will give us information on the distribution of the effective electric fields of the nanocrystals-matrix junctions. The results will complement our EBIC studies and give critical information on the influence of specific structural features on the performance of these photovoltaics.

APPENDIX A

HOMOGENEOUSLY ALLOYED CDS_XSE_{1-X} NANOCRYSTALS: SYNTHESIS, CHARACTERIZATION, AND COMPOSITION/SIZE-DEPENDENT BAND GAP

Laura A. Swafford,[1] Lauren A. Weigand,[1] Michael J. Bowers II,[1] James R. McBride,[1] Jason L. Rapaport,[1] Tony L. Watt,[2] Sriram K. Dixit,[2] Leonard C. Feldman,[2,3] and Sandra J. Rosenthal,1-3*

[1]Department of Chemistry, Vanderbilt University, 7330 Stevenson Center, Station B 351822, Nashville, TN 37235-1822

[2]Vanderbilt Interdisciplinary Program in Materials Science, 2301 Vanderbilt Place, VU Station B 350106, Nashville, TN 37235-0106

[3]Department of Physics and Astronomy, Vanderbilt University, 6301 Stevenson Center, 1807 Station B, Nashville, TN 37235-1807

Email: sandra.j.rosenthal@vanderbilt.edu

Phone: 615-322-2633

Received June 14, 2006

J|A|C|S
ARTICLES
Published on Web 08/29/2006

Homogeneously Alloyed CdS_xSe_{1-x} Nanocrystals: Synthesis, Characterization, and Composition/Size-Dependent Band Gap

Laura A. Swafford,[†] Lauren A. Weigand,[†] Michael J. Bowers II,[†] James R. McBride,[†] Jason L. Rapaport,[†] Tony L. Watt,[‡] Sriram K. Dixit,[‡] Leonard C. Feldman,[‡,§] and Sandra J. Rosenthal*[,†,‡,§]

Contributions from the Department of Chemistry, Vanderbilt University, 7330 Stevenson Center, Station B 351822, Nashville, Tennessee 37235-1822, Vanderbilt Interdisciplinary Program in Materials Science, 2301 Vanderbilt Place, VU Station B 350106, Nashville, Tennessee 37235-0106, and Department of Physics and Astronomy, Vanderbilt University, 6301 Stevenson Center, 1807 Station B, Nashville, Tennessee 37235-1807

Received June 14, 2006; E-mail: sandra.j.rosenthal@vanderbilt.edu

Abstract: Alloy nanocrystals provide an additional degree of freedom in selecting desirable properties for nanoscale engineering because their physical and optical properties depend on both size and composition. We report the pyrolytic synthesis of homogeneously alloyed CdS_xSe_{1-x} nanocrystals in all proportions. The nanocrystals are characterized using UV−visible absorption spectroscopy, transmission electron microscopy, X-ray diffractrometry, and Rutherford backscattering spectrometry to determine precisely structure, size, and composition. The dependence of band gap on nanocrystal size and composition is elucidated, yielding a bowing constant of 0.29, in agreement with bulk values. In addition, the morphology of the resultant nanocrystals can be altered by changing the reaction conditions, generating structures ranging from homogeneous, spherical nanocrystals to one-dimensional gradient nanorods.

Introduction

Semiconductor nanocrystals are of primary interest to several fields of research because of their unique optical properties. They exhibit quantum confinement effects such as size-dependent optical and electronic properties for applications in photovoltaics,[1−6] light-emitting diodes,[7−9] photocatalysis,[10−13] bioassays,[14−20] and electronics.[21−23] Specific applications, however, require multiple characteristics in a single system. For example, very small nanocrystals are desirable for in vivo imaging,[14] yet multiplexing experiments require a range of sizes in order to achieve a range of fluorescence colors. Size also plays a role when nanocrystals must be incorporated into larger superstructures such as mesoporous materials in photovoltaics.[4,24] One solution to the problem of dual requirements is to employ alloy nanocrystals. Since the optical properties of alloys vary with composition, it is possible to tune the spectrum while maintaining a small size. Thus, by varying composition, we gain a second tool for altering physical and optical properties. Both size and composition may be tuned to select multiple desirable qualities simultaneously.

To date, research into pseudobinary (AB_xC_{1-x}) semiconductor alloy nanocrystals has been limited.[25−33] In some cases, alloys

† Department of Chemistry, Vanderbilt University.
‡ Vanderbilt Interdisciplinary Program in Materials Science.
§ Department of Physics and Astronomy, Vanderbilt University.

(1) Swafford, L. A.; Rosenthal, S. J. In *Molecular Nanoelectronics*; Reed, E. M. A., Lee, T., Eds.; American Scientific Publishers: Stevenson Ranch, CA, 2003.
(2) Greenham, N. C.; Peng, X.; Alivisatos, A. P. *Phys. Rev. B* **1996**, *54*, 17628−17637.
(3) Huynh, W. U.; Dittmer, J. J.; Alivisatos, A. P. *Science* **2002**, *295*, 2425−2427.
(4) Robel, I.; Subramanian, V.; Kuno, M.; Kamat, P. V. *J. Am. Chem. Soc.* **2006**, *128*, 2385−2393.
(5) Schaller, R. D.; Klimov, V. I. *Phys. Rev. Lett.* **2004**, *92*, 186601.
(6) Mueller, A. H.; Petruska, M. A.; Achermann, M.; Werder, D. J.; Akhadov, E. A.; Koleske, D. D.; Hoffbauer, M. A.; Klimov, V. I. *Nano Lett.* **2005**, *5*, 1039−1044.
(7) Erwin, M. M.; Kadavanich, A. V.; McBride, J.; Kippeny, T.; Pennycook, S.; Rosenthal, S. J. *Eur. Phys. J. D* **2001**, *16*, 275−277.
(8) Bowers, M. J.; McBride, J. R.; Rosenthal, S. J. *J. Am. Chem. Soc.* **2005**, *127*, 15378−15379.
(9) Gao, M. Y.; Lesser, C.; Kirstein, S.; Mohwald, H.; Rogach, A. L.; Weller, H. *J. Appl. Phys.* **2000**, *87*, 2297−2302.
(10) Wang, L. G.; Pennycook, S. J.; Pantelides, S. T. *Phys. Rev. Lett.* **2002**, *89*, 075506.
(11) Henglein, A. *Pure Appl. Chem.* **1984**, *56*, 1215−1224.
(12) Henglein, A. *Ber. Bunsen-Ges. Phys. Chem. Chem. Phys.* **1997**, *101*, 1562−1572.
(13) Kho, R.; Nguyen, L.; Torres-Martinez, C. L.; Mehra, R. K. *Biochem. Biophys. Res. Commun.* **2000**, *272*, 29−35.
(14) Zimmer, J. P.; Kim, S. W.; Ohnishi, S.; Tanaka, E.; Frangioni, J. V.; Bawendi, M. G. *J. Am. Chem. Soc.* **2006**, *128*, 2526−2527.
(15) Bentzen, E. L.; House, F.; Utley, T. J.; Crowe, J. E.; Wright, D. W. *Nano Lett.* **2005**, *5*, 591−595.
(16) Dubertret, B.; Skourides, P.; Norris, D. J.; Noireaux, V.; Brivanlou, A. H.; Libchaber, A. *Science* **2002**, *298*, 1759−1762.
(17) Gerion, D.; Parak, W. J.; Williams, S. C.; Zanchet, D.; Micheel, C. M.; Alivisatos, A. P. *J. Am. Chem. Soc.* **2002**, *124*, 7070−7074.
(18) Rosenthal, S. J.; Tomlinson, I.; Adkins, E. M.; Schroeter, S.; Adams, S.; Swafford, L.; McBride, J.; Wang, Y. Q.; DeFelice, L. J.; Blakely, R. D. *J. Am. Chem. Soc.* **2002**, *124*, 4586−4594.
(19) Wu, X. Y.; Liu, H. J.; Liu, J. Q.; Haley, K. N.; Treadway, J. A.; Larson, J. P.; Ge, N. F.; Peale, F.; Bruchez, M. P. *Nat. Biotechnol.* **2003**, *21*, 41−46.
(20) Dahan, M.; Levi, S.; Luccardini, C.; Rostaing, P.; Riveau, B.; and Triller, A. *Science* **2003**, *302*, 442−445.
(21) Klein, D. L.; Roth, R.; Lim, A. K. L.; Alivisatos, A. P.; McEuen, P. L. *Nature* **1997**, *389*, 699−701.
(22) Konenkamp, R.; Hoyer, P.; Wahi, A. *J. Appl. Phys.* **1996**, *79*, 7029−7035.
(23) Vlasov, Y. A.; Yao, N.; Norris, D. J. *Adv. Mater.* **1999**, *11*, 165−169.
(24) Peter, L. M.; Riley, D. J.; Tull, E. J.; Wijayantha, K. G. U. *Chem. Commun.* **2002**, 1030−1031.

10.1021/ja063939e CCC: $33.50

have been the unintentional result of an attempt to synthesize a different crystal structure.[25,26] They have also been successfully employed as shell materials for binary nanocrystals;[26−28] a shell that combines the core semiconductor with a higher-band-gap semiconductor generates increased fluorescence due to confinement of the electron and hole to the core while simultaneously ameliorating undesirable interface effects, such as lattice mismatch leading to incomplete shell growth.[26] A number of studies have examined the optical properties of alloy nanocrystals, but either the alloys are shown to have a gradient structure,[25,29] in which the composition of the alloy is different in different parts of the nanocrystal, or no analysis into the homogeneity of the alloy is provided.[30,31] The distinction between a gradient alloy and a homogeneous one is critical because, as we and others show, gradient alloy nanocrystals show optical properties that are significantly different than homogeneous alloys.[32] Kuno and co-workers' study of $HgSe_{1-x}S_x$ nanocrystals presents a highly detailed examination of the optical properties of homogeneous nanocrystals, but for a single size.[33] To our knowledge, only Bailey and Nie's study of $CdSe_xTe_{1-x}$ nanocrystals has explored the effect of alloy composition on the optical properties of homogeneous nanocrystals of several different sizes.[32]

Much of the difficulty in alloy nanocrystal research lies in devising a synthetic scheme to produce the desired alloy structure, be it homogeneous or gradient. To achieve homogeneous alloys, the growth rates of the two constituent materials must be equal[29,32] and the conditions necessary for the growth of one constituent cannot impede the growth of the other. In addition, the structure and bonding of the two materials must be sufficiently similar to allow their facile mixing, otherwise the formation of segregated structures such as core/shells or two different binary nanocrystals may result. In this work, we report the synthesis of homogeneous CdS_xSe_{1-x} nanocrystals over the range $x = 0-1$ using a single synthetic method. The nanocrystals are characterized with respect to structure, composition, size, and optical band gap, and on the basis of these, the dependence of band gap on size and composition is extracted. In addition, by varying the concentration of one of the ligands in the synthesis, we show that we can alter the morphology of the nanocrystals from homogeneous nanocrystals to highly fluorescent, gradient nanocrystals to nanorods with a strong gradient occurring in a single direction, which could be very useful for unidirectional charge transport in nanoelectronic devices.

Experimental Section

Materials. Cadmium oxide (CdO, 99.99%), oleic acid (OA, 90%), tri-*n*-butylphosphine (TBP, 93%), and octadecene (ODE, 90%) were purchased from Aldrich. Selenium shot (Se, 99.99%) was purchased from Strem. Sulfur powder (S, USP sublimed) was purchased from Fisher Scientific. A concentrated selenium stock solution (4 M) was prepared by dissolving 0.79 g of Se in 2.5 mL of TBP and sonicating to achieve complete dissolution. This solution was either used as prepared in growth solutions for larger nanocrystals or was diluted to 100 mL in ODE to produce a 0.1 M Se stock solution. A sulfur stock solution (0.1 M) was prepared by adding 0.32 g of S to 100 mL of ODE and heating to 50−100 °C for several hours until all sulfur had dissolved.

Nanocrystal Synthesis. The synthesis of the alloy nanocrystals was based on the syntheses of CdS and CdSe by Yu and Peng.[34] Typically, 256 mg of CdO, 2.4 mL of OA, and 10 mL of ODE were heated to 315 °C in a 100 mL three-neck round-bottom flask under argon. At 275−280 °C, the solution turned colorless, indicating the formation of cadmium oleate. To produce nanocrystals of composition CdS_xSe_{1-x}, a solution composed of $10x$ mL of S stock solution and $10(1 - x)$ mL of 0.1 M Se stock solution was swiftly injected into the flask via a large-bore needle once it had reached 315 °C. The temperature was then lowered to 275 °C, and the nanocrystals were allowed to grow until the desired size had been achieved (<15 min).

For nanocrystals larger than ~40 Å, addition of a growth solution was required. 0.76 g of CdO, 6 mL of OA, and 25 mL of ODE were heated to 290 °C under argon until the solution turned colorless. The solution was then cooled to 50−100 °C, and $0.16x$ g of S powder was added, stirring until dissolved. Finally, the solution was removed from heat, and $1.25(1 - x)$ mL of 4 M Se stock solution was added once the Cd/S solution had cooled to 30 °C. This growth solution was added dropwise to the nanocrystal reaction vessel at the rate of 3 mL/min, beginning just after the initial S/Se injection. It is noted that this reaction can be scaled up.

Once synthesized, the nanocrystals were isolated by precipitation with a mixture of butanol and ethanol, then centrifuged, and the resulting nanocrystal pellet was resuspended in a small amount of hexane (~3 mL). We found that ODE and excess OA adhered strongly to the nanocrystals, so samples were washed eight times prior to characterization. Rutherford backscattering spectrometry of the waste from the washes confirmed that this amount of washing was sufficient to remove any remaining precursor material; in addition, with eight washes, we observed no contamination from excess organic molecules in the Rutherford backscattering and transmission electron microscopy data.

Characterization. UV−visible absorption spectra were obtained with a Varian Cary 50 UV−vis spectrophotometer. Clean nanocrystals were suspended in hexanes and diluted to an optical density of 0.6−0.8 at the lowest energy peak. The optical band gap was taken as the wavelength at the maximum of this peak. Photoluminescence (PL) and photoluminescent excitation (PLE) spectra were taken on an ISS PC1 photon counting spectrofluorometer. Sample preparation for PL and PLE spectra was identical to that for absorption spectra. High-resolution transmission electron microscopy (TEM) images were taken on a Phillips CM20 200 kV TEM. Samples were prepared by placing a drop of nanocrystals diluted in hexanes to an optical density of <0.1 onto an ultrathin carbon-on-Formvar TEM grid (Ted Pella, Inc.), wicking away any excess solvent. Images were obtained at a calibrated magnification of 420 k×. To determine the average diameter of a sample of nanocrystals, 200−300 of the imaged nanocrystals were measured along the C_3 axis. X-ray diffraction (XRD) scans were obtained using a Scintag X_1 $\theta/2\theta$ automated powder X-ray diffractometer with a Cu target ($\lambda = 1.54056$ Å), a Peltier-cooled solid-state detector, and a zero-background, Si(510) sample support. Rutherford backscattering spectrometry (RBS) was performed using a custom-built setup.[35] Samples were prepared by coating the surface of a pyrolytic graphite substrate (Carbone of America) with nanocrystals diluted in hexanes to an optical density of 0.4−0.6, wicking to remove excess solvent. Experiments were performed in a high vacuum chamber (<10^{-6}

(25) Qian, H. F.; Qiu, X.; Li, L.; Ren, J. C. *J. Phys. Chem. B* **2006**, *110*, 9034−9040.
(26) McBride, J.; Treadway, J.; Feldman, L. C.; Pennycook, S. J.; Rosenthal, S. J. *Nano Lett.* **2006**, *6*, 1496−1501.
(27) Qian, H. F.; Li, L.; Ren, J. C. *Mater. Res. Bull.* **2005**, *40*, 1726−1736.
(28) Zhong, X. H.; Han, M. Y.; Dong, Z. L.; White, T. J.; Knoll, W. *J. Am. Chem. Soc.* **2003**, *125*, 8589−8594.
(29) Jang, E.; Jun, S.; Pu, L. *Chem. Commun.* **2003**, 2964−2965.
(30) Zhong, X. H.; Feng, Y. Y.; Knoll, W.; Han, M. Y. *J. Am. Chem. Soc.* **2003**, *125*, 13559−13563.
(31) Tian, Y. C.; Newton, T.; Kotov, N. A.; Guldi, D. M.; Fendler, J. H. *J. Phys. Chem.* **1996**, *100*, 8927−8939.
(32) Bailey, R. E.; Nie, S. M. *J. Am. Chem. Soc.* **2003**, *125*, 7100−7106.
(33) Kuno, M.; Higginson, K. A.; Qadri, S. B.; Yousuf, M.; Lee, S. H.; Davis, B. L.; Mattoussi, H. *J. Phys. Chem. B* **2003**, *107*, 5758−5767.
(34) Yu, W. W.; Peng, X. G. *Angew. Chem., Int. Ed.* **2002**, *41*, 2368−2371.
(35) Taylor, J.; Kippeny, T.; Rosenthal, S. J. *J. Cluster Sci.* **2001**, *12*, 571−582.

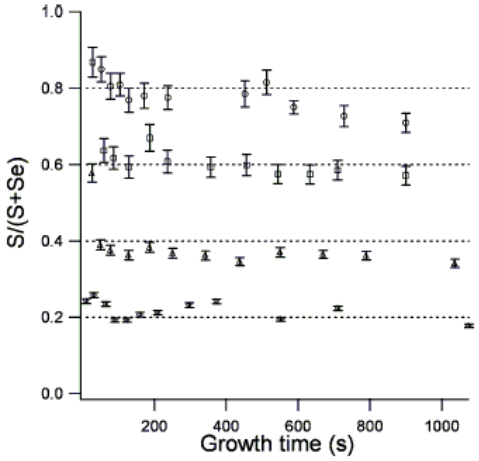

Figure 1. Alloy composition as a function of growth time for $CdS_{0.8}Se_{0.2}$ (○), $CdS_{0.6}Se_{0.4}$ (□), $CdS_{0.4}Se_{0.6}$ (Δ), and $CdS_{0.2}Se_{0.8}$ (◇). RBS analysis of aliquots of nanocrystals pulled from single batches of nanocrystals during growth reveals that the composition of the nanocrystals remains reasonably constant over the growth period, an indication of alloy homogeneity.

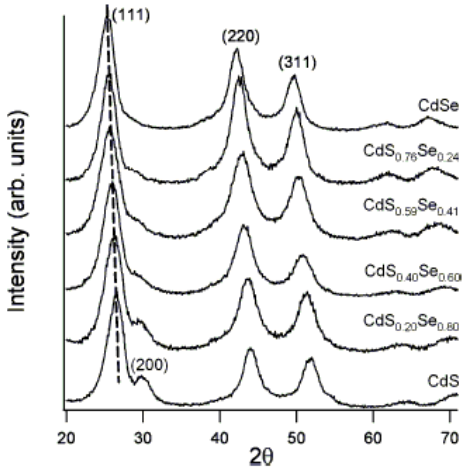

Figure 2. XRD spectra of CdS_xSe_{1-x} nanocrystals. Spectra have been normalized to the height of the (111) peak and offset vertically. The spectra characterize a zinc-blende structure,[42,43] with a linear change in lattice spacing from $x = 0$ to 1 (e.g., see dashed line) and a gradual subsidence of the (200) peak, indicating the formation of alloy nanocrystals rather than a mixture of CdS and CdSe particles.

Torr) with a 1.8 MeV ^{4}He ion beam at normal incidence. Backscattered ions were collected at an angle of 176° with a solid-state detector. Spectra were analyzed according to Feldman et al.,[36] yielding the elemental composition of the nanocrystals.

Results and Discussion

Homogeneity and Structure. In order to confirm that the nanocrystals were indeed homogeneous, batches of nanocrystals were grown to large size, with the periodic removal of aliquots of the growing nanocrystals. The aliquots were then washed and analyzed by RBS to determine composition. As demonstrated in Figure 1, except very early in nanocrystal growth, the composition remained nearly constant over the growth period, indicating that the alloys were homogeneous, rather than gradient or core/shell in nature. It should be noted that at the very smallest sizes, all nanocrystals were shown to be sulfur-rich by RBS. There are two possible explanations for this observation. The first is simply that it is very difficult to clean the smallest nanocrystals, so RBS may be detecting unreacted sulfur precursor. The second explanation is that the kinetics of nucleation are different than the kinetics of growth, resulting in sulfur enrichment at the smallest sizes. Indeed, the smallest sizes are most likely magic-number nanocrystals, composed of only a few atoms.[8,37−41] CdSe nanocrystals halted at the same stage of growth displayed the same absorption and emission characteristics as magic-number nanocrystals produced previously by a different synthesis.[8] If it is true that the nucleation kinetics in this reaction favor the formation of sulfur-rich seeds, these seeds are very small. As seen in Figure 1, the nanocrystals achieve the expected composition within 30 s, suggesting that the sulfur-rich seeds are so small that they constitute a nearly negligible portion of larger nanocrystals. As we shall see later, the sulfur-rich seeds do not seem to affect the dependence of band gap on size and composition; therefore, we consider the nanocrystals larger than the seeds to be essentially homogeneous.

This conclusion is supported by XRD spectra of the nanocrystals (Figure 2), which show a linear change in lattice spacing as composition changes from CdS to CdSe (e.g., dashed line). If the nanocrystals were a mixture of CdS nanocrystals and CdSe nanocrystals instead of alloys, the resultant XRD spectra would exhibit a superposition of the spectra of pure CdS and pure CdSe. It is noted that core/shell nanocrystals also show spectra that are intermediate between the spectra of the core and the shell.[44,45] However, since the RBS data show little change in composition with size, core/shell structures are unlikely; to maintain a core/shell structure throughout nanocrystal growth would necessitate constant rearrangement of interior atoms, which is highly unlikely. The spectra also show a zinc-blende conformation throughout the range of compositions, in contrast to Yu and Peng's synthesis,[34] which shows a mix of zinc-blende and wurtzite structures. The zinc-blende structure is likely due to the surfactant system used;[43,46,47] that there are fewer wurtzite stacking faults may reflect the higher temperatures at which the synthesis was conducted or the lower amount of tributylphosphine used (1:1 Se/TBP molar ratio).

High-resolution TEM images confirm the zinc-blende structure and appear spherical with a few aberrant pyramids (Figure 3). An indication of the narrow size distribution is that these nanocrystals readily form arrays on the carbon film support.[48]

(36) Feldman, L. C.; Mayer, J. W. *Fundamentals of Surface and Thin Film Analysis*; North Holland-Elsevier: New York, 1986.
(37) Peng, Z. A.; Peng, X. G. *J. Am. Chem. Soc.* **2002**, *124*, 3343−3353.
(38) Qu, L.; Yu, W. W.; Peng, X. G. *Nano Lett.* **2004**, *4*, 465−469.
(39) Landes, C.; Braun, M.; Burda, C.; El-Sayed, M. A. *Nano Lett.* **2001**, *1*, 667−670.
(40) Landes, C.; El-Sayed, M. A. *J. Phys. Chem. A* **2002**, *106*, 7621−7627.
(41) Chen, X. B.; Samia, A. C. S.; Lou, Y. B.; Burda, C. *J. Am. Chem. Soc.* **2005**, *127*, 4372−4375.
(42) Urbieta, A.; Fernández, P.; Piqueras, J. *J. Appl. Phys.* **2004**, *96*, 2210−2213.
(43) Mohamed, M. B.; Tonti, D.; Al-Salman, A.; Chemseddine, A.; Chergui, M. *J. Phys. Chem. B* **2005**, *109*, 10533−10537.
(44) Li, J. J.; Wang, Y. A.; Guo, W. Z.; Keay, J. C.; Mishima, T. D.; Johnson, M. B.; Peng, X. G. *J. Am. Chem. Soc.* **2003**, *125*, 12567−12575.
(45) Peng, X. G.; Schlamp, M. C.; Kadavanich, A. V.; Alivisatos, A. P. *J. Am. Chem. Soc.* **1997**, *119*, 7019−7029.
(46) Jasieniak, J.; Bullen, C.; van Embden, J.; Mulvaney, P. *J. Phys. Chem. B* **2005**, *109*, 20665−20668.
(47) Yu, W. W.; Wang, Y. A.; Peng, X. G. *Chem. Mater.* **2003**, *15*, 4300−4308.

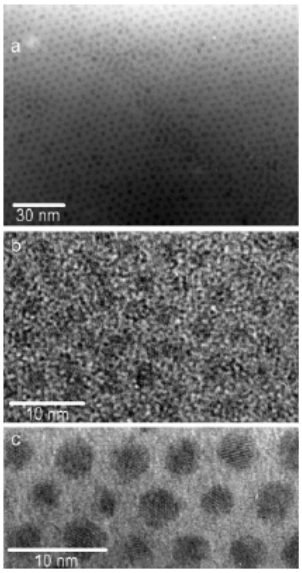

Figure 3. TEM images of $CdS_{0.8}Se_{0.2}$ (a), $CdS_{0.4}Se_{0.6}$ (b), and $CdS_{0.2}Se_{0.8}$ (c) show a highly crystalline, spherical, primarily zinc-blende structure with a few wurtzite stacking faults. Size dispersity is low, allowing the nanocrystals to array on the TEM grid.

The average size distribution of the samples was measured using TEM images was 11.5% (standard deviation); this number is likely slightly larger than the true distribution due to the method of measuring.

Optical Properties and Bowing Constant. Figure 4a shows typical UV−vis absorption and PL spectra for the alloy nanocrystals. The spectra appear similar to those of CdS and CdSe nanocrystals. Absorption spectra are characterized by several distinct peaks, an indication of good size distribution. The spacing and intensity of these peaks show some variation (e.g., see Figure 5b), indicating potentially intriguing electronic structure in the alloys. The PLE spectra of the nanocrystals confirm that the cause is not inhomogeneity in the samples (e.g., Figure 4b). PL spectra are characterized by two peaks: a higher-energy, narrow (30−38 nm fwhm) peak assigned to band edge emission and a lower-energy, broad peak assigned to "deep trap" emission, caused by trapping of the photoexcited hole to unpassivated surface anion orbitals.[49−51] The band edge emission is red-shifted from the band edge absorption peak by 5−30 nm, with smaller nanocrystals showing larger shifts. Likewise, the relative intensity of deep trap emission varies from none in large nanocrystals to a peak intensity on the order of the intensity of the band edge emission for small nanocrystals; this behavior is similar to CdSe nanocrystals synthesized in tri-*n*-octylphosphine oxide (TOPO).[49]

The behavior of alloys is characterized by Végard's Law, which states that, while lattice constant changes linearly with composition, as seen in Figure 2, other physical properties such

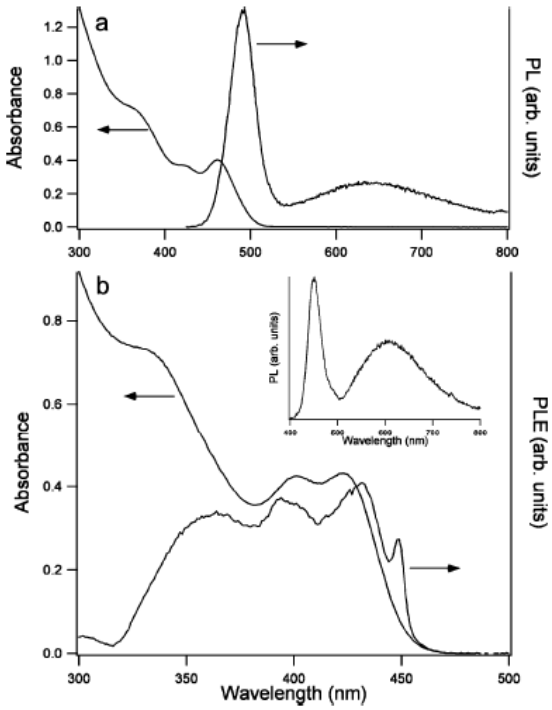

Figure 4. (a) Absorbance and PL spectra of 35 Å $CdS_{0.53}Se_{0.47}$ nanocrystals. These spectra typify the optical properties of the alloy nanocrystals. (b) Absorbance and PLE spectra of 24 Å $CdS_{0.70}Se_{0.30}$ nanocrystals. The PLE spectrum, taken at the maximum of the band edge emission (450 nm), agrees closely with the absorption spectrum close to the band edge, an indication that the sample is homogeneous. The inset shows the PL spectrum for this sample. The PL spectra in (a) and (b) were taken with an excitation wavelength of 367 nm.

as band gap often vary nonlinearly.[52] To first approximation, the variation is quadratic:

$$E_g(CdS_xSe_{1-x}) = xE_g(CdS) + (1-x)E_g(CdSe) - bx(1-x) \quad (1)$$

where the bowing constant, b, describes the extent of nonlinearity. The sources of nonlinearity are threefold: (i) the changing lattice constant alters the band structure; (ii) the atoms in the alloy have different electronegativities, deforming the electron distribution; and (iii) anion−cation bond lengths and angles must relax in order to accommodate the differently sized constituents.[53,54] In the case of nanocrystals of *any* composition, quantum confinement also dictates a size dependence:[55]

$$E_g(d) = E_g(\infty) + \frac{a}{d} + \frac{c}{d^2} \quad (2)$$

where d is the nanocrystal diameter and a and c are empirical fit parameters.[56] The dependence of band gap on size and on composition are demonstrated in Figure 5. Substituting eq 2

(48) Murray, C. B.; Kagan, C. R.; Bawendi, M. G. *Annu. Rev. Mater. Sci.* **2000**, *30*, 545−610.
(49) Underwood, D. F.; Kippeny, T.; Rosenthal, S. J. *J. Phys. Chem. B* **2001**, *105*, 436−443.
(50) Katari, J. E. B.; Colvin, V. L.; Alivisatos, A. P. *J. Phys. Chem.* **1994**, *98*, 4109−4117.
(51) Shiang, J. J.; Kadavanich, A. V.; Grubbs, R. K.; Alivisatos, A. P. *J. Phys. Chem.* **1995**, *99*, 17417−17422.
(52) Végard, L. *Z. Phys.* **1921**, *5*, 17−26.
(53) Bernard, J. E.; Zunger, A. *Phys. Rev. B* **1987**, *36*, 3199−3228.
(54) Böer, K. W. *Survey of Semiconductor Physics: Electrons and Other Particles in Bulk Semiconductors*; Van Nostrand Reinhold: New York, 1990.
(55) Brus, L. E. *J. Chem. Phys.* **1984**, *80*, 4403−4409.

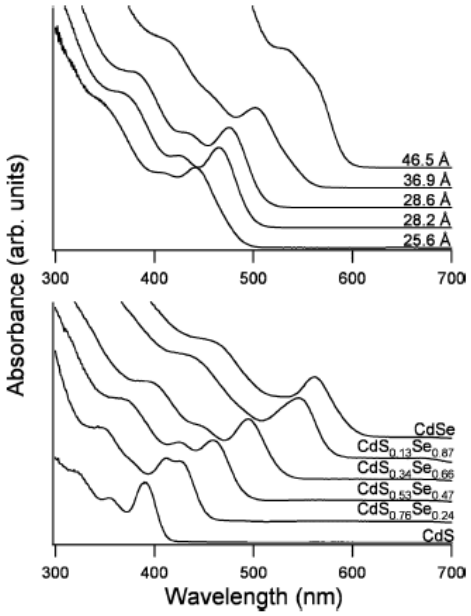

Figure 5. Linear UV−visible absorption spectra demonstrating dependence of band gap on size and composition: (top) size dependence of ~$CdS_{0.4}Se_{0.6}$ nanocrystals; (bottom) composition dependence of ~30 Å nanocrystals.

into eq 1, we find that the dependence of band gap on size and composition is given by

$$E_g(x,d) = x\left[E_g(\mathrm{CdS},\infty) + \frac{a_1}{d} + \frac{c_1}{d^2}\right] + (1-x)\left[E_g(\mathrm{CdSe},\infty) + \frac{a_2}{d} + \frac{c_2}{d^2}\right] - b(d)x(1-x) \quad (3)$$

In this expression, the bowing constant is expressed as a function of the nanocrystal diameter. The size dependence is included for a number of reasons. First, lattice spacing is known to decrease slightly with decreasing nanocrystal diameter, a function of surface tension.[58] Second, surface reconstruction can affect cation−anion bond lengths, as well as electron distribution.[59−61] Third, ligand effects can also alter cation−anion bond lengths and charge distribution.[60] Combined, these effects could significantly impact the bowing constant, particularly at small diameters. It is noted that, in eq 3, any nonlinearity in the change in the parameters a and c between their CdS and CdSe values is contained within the bowing constant; if these values vary with composition in a manner different than the bulk band gap (E_g(CdS,∞) and E_g(CdSe,∞)), then the bowing constant should depend on size.

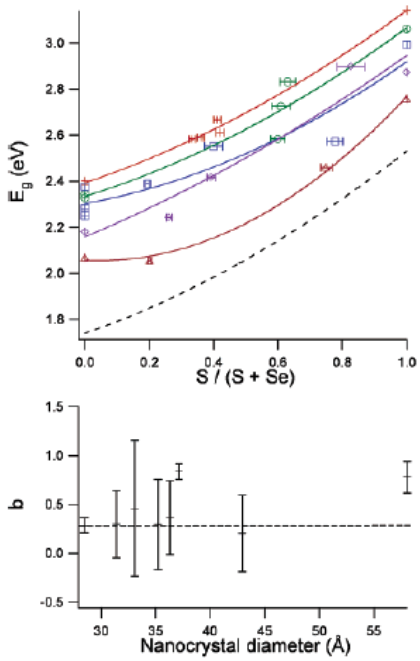

Figure 6. Bowing vs size for CdS_xSe_{1-x} nanocrystals. (top) Band gap as a function of composition for 28 (+), 31 (○), 36 (□), 43 (◇), and 58 Å (△) nanocrystals. Curves show the bowing, which remains relatively constant and closely follows the bulk bowing behavior (dashed line from eq 1; E_g(CdS,∞) = 2.53 eV,[64] E_g(CdSe,∞) = 1.74 eV,[64] b = 0.3[58,65,66]). Values for CdS and CdSe nanocrystals were either measured in this work, extrapolated from Yu et al.,[60] or calculated from a fit to the data of Yu et al. (Table 1). For clarity, only five sizes are shown. (bottom) Bowing constant as a function of nanocrystal diameter. The dashed line indicates the bowing constant, 0.29, obtained by fitting all data to eq 3. From this graph, it is evident that the bowing constant remains constant (within the uncertainty of the data) over the range of the experiment.

Figure 6 shows the dependence of bowing constant on size. Results show that, within the uncertainty and range of this work, the bowing constant is in fact insensitive to diameter, in agreement with previous work on $CdSe_xTe_{1-x}$.[32] This suggests that the small change in lattice constant with size is not enough to significantly impact the band structure. More intriguingly, it suggests that the surface and surrounding environment (ligands and solvent), which are known to impact strongly the optical and electronic behavior of nanocrystals,[55,62−67] do not affect nanocrystal band gap bowing beyond their effects on the size dependence of the band gap. As size decreases and the surface-to-volume ratio increases, surface effects play an increasingly important role in nanocrystal behavior, distorting bonding, and electronic structure, which might affect bowing for the reasons mentioned above. Finally, the fact that the bowing in these nanocrystals is identical to bulk values suggests that any structural anomalies and compositional fluctuations, both of

(56) In Brus' original work,[55] the parameters a and c have physical meaning based on bulk material properties such as effective mass and dielectric constant; however, due to the failure of the effective mass approximation at small diameters,[55, 57] we have found that a much better fit is attained when a and c are allowed to float.

(57) Kippeny, T.; Swafford, L. A.; Rosenthal, S. J. *J. Chem. Ed.* **2002**, *79*, 1094−1100.
(58) Tolbert, S. H.; Alivisatos, A. P. *J. Chem. Phys.* **1995**, *102*, 4642−4656.
(59) Bawendi, M. G.; Kortan, A. R.; Steigerwald, M. L.; Brus, L. E. *J. Chem. Phys.* **1989**, *91*, 7282−7290.
(60) McGinley, C.; Riedler, M.; Moller, T.; Borchert, H.; Haubold, S.; Haase, M.; Weller, H. *Phys. Rev. B* **2002**, *65*, 245308.
(61) Rabani, E. *J. Chem. Phys.* **2001**, *115*, 1493−1497.
(62) Wang, L. W.; Zunger, A. *Phys. Rev. B* **1996**, *53*, 9579−9582.
(63) Guyot-Sionnest, P.; Wehrenberg, B.; Yu, D. *J. Chem. Phys.* **2005**, *123*, 074709.
(64) Kalyuzhny, G.; Murray, R. W. *J. Phys. Chem. B* **2005**, *109*, 7012−7021.
(65) Myung, N.; Bae, Y.; Bard, A. J. *Nano Lett.* **2003**, *3*, 747−749.
(66) Califano, M.; Franceschetti, A.; Zunger, A. *Nano Lett.* **2005**, *5*, 2360−2364.
(67) Kippeny, T. C.; Bowers, M. J., II; McBride, J. R.; Rosenthal, S. J. Submitted for publication.

Table 1. Fitting Parameters for Calculation of Bowing Constant

	a_{CdS} (eV–Å)	c_{CdS} (eV–Å^2)	a_{CdSe} (eV–Å)	c_{CdSe} (eV–Å^2)	B
fixed[a]	8.4 ± 2.1	245 ± 34	19.6 ± 0.8	−28.8 ± 7.5	0.31 ± 0.10
floated[b]	7.9 ± 2.7	252 ± 44	19.5 ± 0.8	−28.0 ± 7.0	0.29 ± 0.16

[a] a and c were calculated by fitting CdS and CdSe data from Yu et al.,[70] as well as our data to eq 2, with $E_g(\infty)$ fixed at 2.53[74] and 1.74 eV,[74] respectively. These values were then substituted into eq 3 to obtain the bowing constant. [b] The bulk band gaps of 2.53[74] and 1.74 eV[74] for CdS and CdSe, respectively, were substituted into eq 3 to obtain the bowing constant, as well as a and c.

which are known to contribute to the bowing phenomenon,[53,68,69] are not severe enough to affect the optoelectronic behavior of the nanocrystals, so that they can indeed be considered homogeneous.

With this information, the band gaps, compositions, and diameters of 36 alloy samples ranging in diameter from 20 to 80 Å were combined with band gap and size data for CdS and CdSe from Yu et al.[70] and fit to eq 3 in two ways, summarized in Table 1. First, all data for CdS and CdSe were fit to eq 2 to obtain a and c for the two materials.[71] These values for a and c were then substituted into eq 3 along with the bulk band gaps, yielding a bowing constant of 0.31 ± 0.10. Next, the fit was repeated, but a and c were allowed to float, yielding a bowing constant of 0.29 ± 0.16. These values are in good agreement; moreover, they agree well with the bulk bowing constant, which has been reported as 0.3[68,75,76] or less than 0,[69,77,78] presumably due to differences in synthetic and analytical techniques; others have suggested that the work showing negative bowing constants was performed on thin films whose actual composition and homogeneity may be suspect.[75] In addition, the values for a and c obtained from eq 3 when they were allowed to float agree well with their values from fits to pure CdS and CdSe.

That the observed bowing constant in the nanocrystals agrees with the bulk value and that the bowing constant, a, and c were approximately identical regardless of how the data were fit suggests that a and c are linear combinations of the binary constituents. Consequently, we may simplify eq 3 to

$$E_g(x,d) = E_g(x,\infty) + \frac{a_x}{d} + \frac{c_x}{d^2} \tag{4}$$

where $E_g(x,\infty)$ is given by eq 1 and a_x and c_x are the linear combinations

$$a_x = xa_1 + (1-x)a_2$$
$$c_x = xc_1 + (1-x)c_2 \tag{5}$$

Equation 4 is a more elegant form of eq 3 because it shows the traditional dependence of band gap on size for nanocrystals (e.g., eq 2); moreover, it demonstrates that the bowing constant is independent of both size and the empirical parameters, a and c.

Regardless of the degree of bowing, these results demonstrate that, by varying the composition of the nanocrystals, we have introduced an additional means of tuning their properties. Multiple wavelengths can be generated by a single size, which could be useful when size requirements are specific, such as in biological imaging, where small nanocrystals are desirable. In addition, by using alloys, we can easily achieve band gaps (and other properties) which otherwise would be difficult to achieve. For example, in the case of CdS and CdSe, making nanocrystals with a band gap of 2.6 eV (480 nm) is normally difficult; CdS nanocrystals would need to be very large (>100 Å), often resulting in a large size dispersity, while CdSe nanocrystals would conversely be very small (21 Å), difficult to synthesize accurately due to the speed of most reactions, difficult to image by TEM, and less stable than medium and large nanocrystals. $CdS_{0.8}Se_{0.2}$, however, produces the same band gap with a nanocrystal diameter of 32 Å, which is an ideal size from the standpoint of synthesis, imaging, and stability. We anticipate that for these and other reasons, alloys will play an increasingly important role in nanoengineering.

Growth Kinetics and Effect of TBP. In order to synthesize homogeneous CdS_xSe_{1-x} nanocrystals, sulfur and selenium must be added at the same rate to the growing nanocrystals. While the exact mechanisms of nanocrystal nucleation and growth are not known,[37,79–81] and the kinetics are debated,[34,80] it is reasonable to assume that the reactivities of cadmium monomer toward the two anions on the nanocrystal surface should not be markedly different, given that sulfur and selenium are isoelectronic and have very similar Lewis basicities. If the reactivities were very different, it is likely that a homogeneous alloy would be difficult if not impossible to achieve. Assuming that the rate of addition of cadmium to the growing nanocrystal is largely independent of the anion species to which it binds, and assuming that the rates of addition of sulfur and selenium obey first-order kinetics with respect to anion concentration, then the ratio of these rates is proportional to the ratio of the concentrations of sulfur and selenium:

$$\frac{\frac{d[AS\text{-}S]}{dt}}{\frac{d[AS\text{-}Se]}{dt}} = \frac{k_1[AS][S]}{k_2[AS][Se]} = \frac{k_1}{k_2}\frac{[S]}{[Se]} \tag{6}$$

Here AS is an available site for anion bonding and k_1 and k_2 are rate constants. This model of growth kinetics suggests two means of balancing these rates. For the rates to remain identical throughout nanocrystal growth, either the concentrations of sulfur and selenium must not change significantly during growth or k_1 and k_2 must be identical.

(68) Naumov, A.; Permogorov, S.; Reznitsky, A.; Verbin, S.; Klochikhin, A. *J. Cryst. Growth* **1990**, *101*, 713−717.
(69) Kumar, V.; Sharma, T. P. *J. Phys. Chem. Solids* **1998**, *59*, 1321−1325.
(70) Yu, W. W.; Qu, L. H.; Guo, W. Z.; Peng, X. G. *Chem. Mater.* **2003**, *15*, 2854−2860.
(71) No distinction was made between wurtzite and zinc-blende nanocrystals in the case of CdS and CdSe; because of the negligible differences in band gap and lattice constant for the bulk materials in the two conformations,[72−74] it was assumed that the size dependence of the band gap was likewise similar.
(72) Trindade, T.; O' Brien, P.; Pickett, N. L. *Chem. Mater.* **2001**, *13*, 3843−3858.
(73) Kadavanich, A. V. The Structure and Morphology of Semiconductor Nanocrystals. Ph.D. Thesis, Chemistry Department, University of California, Berkeley, 1997.
(74) Landolt, H. *Landolt-Börnstein: Numerical Data and Fimctional Relationships in Science and Technology*; Madelung, O., Ed.; Springer: New York, 1982; Vol. III-17b.
(75) Wei, S.-H.; Zhang, Z. B.; Zunger, A. *J. Appl. Phys.* **2000**, *87*, 1304−1311.
(76) Goede, O.; Hennig, D.; John, L. *Phys. Status Solidi B* **1979**, *96*, 671−681.
(77) Mane, R. S.; Lokhande, C. D. *Thin Solid Films* **1997**, *304*, 56−60.
(78) Kainthla, R. C.; Pandya, D. K.; Chopra, K. L. *J. Electrochem. Soc.* **1982**, *129*, 99−102.
(79) Peng, Z. A.; Peng, X. G. *J. Am. Chem. Soc.* **2001**, *123*, 1389−1395.
(80) Bullen, C. R.; Mulvaney, P. *Nano Lett.* **2004**, *4*, 2303−2307.
(81) Peng, Z. A.; Peng, X. G. *J. Am. Chem. Soc.* **2001**, *123*, 183−184.

The first approach was used successfully by Bailey and Nie[32] in the synthesis of $CdSe_xTe_{1-x}$ nanocrystals. By employing a cadmium-limited reaction, in which there was a large excess of anion precursor relative to cadmium, they limited the number of sites available for anion binding to the extent that selenium and tellurium concentrations remained essentially constant throughout the reaction, so the rate constants were immaterial. Indeed, when they increased the amount of cadmium, they grew gradient alloys because the rate constants were unequal. In initial attempts to produce homogeneous CdS_xSe_{1-x}, two different synthetic schemes were applied—a dimethylcadmium-based synthesis devised by Kippeny et al.[67] and the cadmium oxide synthesis presented here in the experimental section. Unfortunately, neither synthesis was successfully adapted to produce high-quality nanocrystals under cadmium-limited conditions. These results are in agreement with other research showing that cadmium oxide must be kept in excess of anion concentration.[80,81]

The second approach to equalizing the reaction rates of sulfur and selenium was the equalization of the rate constants or the tuning of the reactivities of the anion precursors. Studies have shown that the rate of nanocrystal growth is sensitive not only to precursor species but to ligand concentrations as well.[34,47,80,81] Fortunately, in the synthesis presented in the Experimental Section, a means of tuning the reactivities of the anion precursors was available in the amount of TBP used in the selenium precursor. Early on, it was noted that sulfur binds strongly to TBP, so as to inhibit CdS nucleation and growth. Since in the synthesis of the alloyed nanocrystals the anion precursors must be mixed in advance of the reaction, excess TBP in the selenium precursor could react with sulfur, changing the reactivity of the sulfur. To explore the effects of TBP on alloy homogeneity, nanocrystals were synthesized with selenium precursor solutions of 2.5%, 3.0%, and 8.3% by volume of TBP. Small aliquots of the nanocrystal solution were removed from the reaction vessel periodically so that RBS could be used to monitor the changing composition of the nanocrystals during growth.

Figure 7 shows the composition of alloy nanocrystals with a precursor sulfur fraction of 0.4 as a function of growth time. The same trends were seen for all compositions. As seen previously, nanocrystals made with 2.5% TBP precursor were spherical and had a sulfur concentration that was nearly constant throughout their growth, an indication of homogeneous alloying. Nanocrystals produced using 3.0% TBP precursor remained spherical, but the sulfur concentration increased slightly with time, indicating a gradient structure. We explain the increasing sulfur concentration on the basis of the excess TBP. Prior to injection, the sulfur and selenium precursors were mixed, allowing any TBP not bound to selenium to bind to sulfur instead. When injected into the reaction vessel, the bound sulfur reacted much slower than selenium or unbound sulfur, causing initial sulfur concentrations that were lower than might be expected. Then, as available selenium depleted, sulfur was increasingly the only anion available for nanocrystal growth, causing the sulfur concentration on the exterior of the nanocrystal to increase, resulting in the observed gradient structure. The optical behavior of these nanocrystals also differed from those produced by the 2.5% precursor. Fluorescent quantum yields for the 3.0% TBP nanocrystals were higher, on the order of 0.30, as compared to yields of <0.01 for the 2.5% TBP

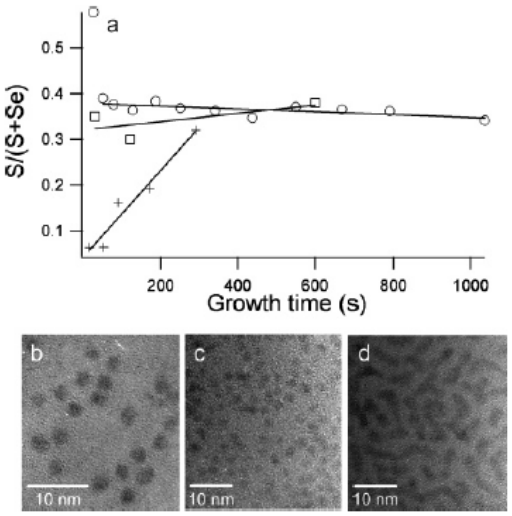

Figure 7. (top) Alloy composition as a function of growth time for $CdS_{0.4}Se_{0.6}$ grown using Se precursor solutions that were 2.5% (○), 3.0% (□), and 8.3% (+) TBP by volume. The 8.3% precursor shows a strong increase in sulfur with growth, indicating the formation of gradient alloys. The 3.0% precursor shows a slight increase in sulfur, and the 2.5% precursor a slight decrease. It is noted that the nanocrystals produced using the 2.5% TBP precursor were synthesized with the use of growth solution, unlike the 3.0% and 8.3% nanocrystals; the 2.5% nanocrystals are therefore much larger. (bottom) TEM images of nanocrystals synthesized using 2.5% (b), 3.0% (c), and 8.3% (d) TBP solutions. Lower amounts of TBP produce spherical nanocrystals, while higher amounts produce irregularly shaped nanorods.

nanocrystals and for pure CdS and CdSe. This is easily explained by the gradient structure; if the exterior had a higher concentration of sulfur, then electrons and holes in excited nanocrystals would be energetically confined to the center of the nanocrystal, enhancing fluorescence in the same manner as a core/shell structure. Moreover, a limited study on the band gaps of these nanocrystals yielded a bowing constant of 0.37 ± 0.23. Although this value agrees with the bowing constant of the 2.5% TBP nanocrystals within the uncertainty of the data, if the small increase is in fact real, then the 3.0% TBP nanocrystals behaved like homogeneous nanocrystals that were slightly smaller and slightly more selenium-rich, as could be expected from a gradient structure.

To explore further the effect of TBP on alloy growth, the TBP concentration was increased to 8.3%. With TBP in such excess, the gradient effect was greatly enhanced; the concentration of sulfur in the nanocrystals was initially almost nonexistent and increased dramatically with growth time. TEM images show that nanocrystals produced by this route were rodlike, suggesting that free TBP promotes growth along the *c* axis. Since they preferentially grew in a single direction and since previous work has shown that nanocrystals grow almost exclusively from the unpassivated anion-terminated face,[79,82] the gradient also likely propagated solely in this direction; certainly the quantum yield of these nanocrystals was no greater than the 3.0% TBP nanocrystals, indicating that the selenium-rich portion of these nanocrystals is no more shielded from the exterior than the 3.0% TBP nanocrystals. Although the 8.3% TBP nanocrystals were the wrong structure and composition for this study and were

(82) McBride, J. R.; Kippeny, T. C.; Pennycook, S. J.; Rosenthal, S. J. *Nano Lett.* **2004**, *4*, 1279−1283.

therefore quickly abandoned, they nonetheless remain an intriguing structure with potential applications in nanoelectronic devices. The one-dimensional gradient may generate gradient energy bands that could funnel charges unidirectionally; similar structures can be found in bulk semiconductor devices. Thus, simply by altering the amount of TBP in the reaction, it is possible to create homogeneous alloys, highly fluorescent gradient alloys, and unidirectionally gradient alloys.

Conclusions

We report for the first time the synthesis of homogeneously alloyed, zinc-blende CdS_xSe_{1-x} nanocrystals in all proportions. The band gap of these nanocrystals can be tuned by size or by composition, enabling the selection of more than one property (e.g., size and color) for specific applications. The dependence of the band gap on alloy composition is found to be slightly nonlinear, with a bowing constant of 0.29, in close agreement with bulk values; the bowing is not measurably size-dependent. In addition, the amount of TBP used in the reaction alters the morphology of the resultant nanocrystals, generating anything from homogeneous, spherical nanocrystals to one-dimensional, gradient nanorods, which may have applications in nanoelectronic devices.

Acknowledgment. The authors gratefully acknowledge Dr. Anthony Hmelo for training in the use of the RBS spectrometer and Dr. Charles Lukehart for training and use of the XRD spectrometer. L.A.W. was supported by a Stephen H. Cook fellowship. T.L.W. was supported by a National Science Foundation IGERT fellowship (DMR-0333392). Funding for this work was provided by the Department of Energy (DEFG0202ER45957) and the National Institutes of Health (RO1 EB003728).

JA063939E

REFERENCES

(1) Summary for Policymakers: Emissions Scenarios, Intergovernmental Panel on Climate Change, 2000.

(2) Lewis, N. S.; Crabtree, G.; Nozik, A. J.; Wasielewski, M. R.; Alivisatos, P.; Basic Energy Sciences, U. S. D. o. E., Ed. 2005.

(3) Office of Energy Efficiency and Renewable Energy, U. S. D. o. E.; Office of Energy Efficiency and Renewable Energy, U. S. D., Ed. 2005.

(4) Shockley, W.; Queisser, H. J. *Journal of Applied Physics* **1961**, *32*, 510-519.

(5) Oregan, B.; Gratzel, M. *Nature* **1991**, *353*, 737-740.

(6) Swafford, L. A.; Rosenthal, S. J. In *Molecular Nanoelectronics*; Reed, M. A., Lee, T., Eds.; American Scientific Publishers: 2003.

(7) Ellingson, R. J.; Beard, M. C.; Johnson, J. C.; Yu, P. R.; Micic, O. I.; Nozik, A. J.; Shabaev, A.; Efros, A. L. *Nano Letters* **2005**, *5*, 865-871.

(8) Ivanov, S. A.; Nanda, J.; Piryatinski, A.; Achermann, M.; Balet, L. P.; Bezel, I. V.; Anikeeva, P. O.; Tretiak, S.; Klimov, V. I. *J. Phys. Chem. B* **2004**, *108*, 10625-10630.

(9) Cui, Y.; Bjork, M. T.; Liddle, J. A.; Sonnichsen, C.; Boussert, B.; Alivisatos, A. P. *Nano Letters* **2004**, *4*, 1093-1098.

(10) Mor, G. K.; Shankar, K.; Paulose, M.; Varghese, O. K.; Grimes, C. A. *Nano Letters* **2006**, *6*, 215-218.

(11) Murray, C. B.; Norris, D. J.; Bawendi, M. G. *Journal Of The American Chemical Society* **1993**, *115*, 8706-8715.

(12) Ho, W. K.; Yu, J. C. *Journal of Molecular Catalysis a-Chemical* **2006**, *247*, 268-274.

(13) Rosenthal, S. J.; D.O.E., Ed.; Office of Science: 2004.

(14) Zukalova, M.; Zukal, A.; Kavan, L.; Nazeeruddin, M. K.; Liska, P.; Gratzel, M. *Nano Letters* **2005**, *5*, 1789-1792.

(15) Carreon, M. A.; Guliants, V. V. *European Journal of Inorganic Chemistry* **2005**, 27-43.

(16) Wang, P.; Wang, L.; Ma, B.; Li, B.; Qiu, Y. *J. Phys. Chem. B* **2006**, *110*, 14406-14409.

(17) Blanton, S. A.; Leheny, R. L.; Hines, M. A.; GuyotSionnest, P. *Physical Review Letters* **1997**, *79*, 865-868.

(18) Zhang, S.; Cyr, P. W.; McDonald, S. A.; Konstantatos, G.; Sargent, E. H. *Applied Physics Letters* **2005**, *87*.

(19) Swafford, L. A.; Weigand, L. A.; Bowers II, M. J.; McBride, J. R.; Rapaport, J. L.; Watt, T. L.; Dixit, S. K.; Feldman, L. C.; Rosenthal, S. J. *Journal of the American Chemical Society* **2006**, *128*.

(20) Gunes, S.; Neugebauer, H.; Sariciftci, N. S.; Roither, H.; Kovalenko, M.; Pillwein, G.; Heiss, W. *Advanced Functional Materials* **2006**, *16*, 1095-1099.

(21) Nozik, A. J. *Physica E-Low-Dimensional Systems & Nanostructures* **2002**, *14*, 115-120.

(22) Califano, M.; Zunger, A.; Franceschetti, A. *Nano Letters* **2004**, *4*, 525-531.

(23) Schaller, R. D.; Klimov, V. I. *Physical Review Letters* **2004**, *92*, -.

(24) Peter, L. M.; Riley, D. J.; Tull, E. J.; Wijayantha, K. G. U. *Chemical Communications* **2002**, 1030-1031.

(25) Wijayantha, K. G. U.; Peter, L. M.; Otley, L. C. *Solar Energy Materials and Solar Cells* **2004**, *83*, 363-369.

(26) Robel, I.; Subramanian, V.; Kuno, M.; Kamat, P. V. *Journal Of The American Chemical Society* **2006**, *128*, 2385-2393.

(27) Rosenthal, S. J.; D.O.E., Ed.; Office of Science: 2007.

(28) Mahajan, S. V.; Kavich, D. W.; Redigolo, M. L.; Dickerson, J. H. *Journal Of Materials Science* **2006**, *41*, 8160-8165.

(29) Lee, Y. H.; Kuo, C. W.; Shih, C. J.; Hung, I. M.; Fung, K. Z.; Wen, S. B.; Wang, M. C. *Materials Science And Engineering A-Structural Materials Properties Microstructure And Processing* **2007**, *445*, 347-354.

(30) Wong, E. M.; Searson, P. C. *Applied Physics Letters* **1999**, *74*, 2939-2941.

(31) Islam, M. A.; Herman, I. P. *Applied Physics Letters* **2002**, *80*, 3823-3825.

(32) Islam, M. A.; Xia, Y. Q.; Steigerwald, M. L.; Yin, M.; Liu, Z.; O'Brien, S.; Levicky, R.; Herman, I. P. *Nano Letters* **2003**, *3*, 1603-1606.

(33) Islam, M. A.; Xia, Y. Q.; Telesca, D. A.; Steigerwald, M. L.; Herman, I. P. *Chemistry Of Materials* **2004**, *16*, 49-54.

(34) Zhang, Q. L.; Xu, T.; Butterfield, D.; Misner, M. J.; Ryu, D. Y.; Emrick, T.; Russell, T. P. *Nano Letters* **2005**, *5*, 357-361.

(35) Shim, M.; Guyot-Sionnest, P. *Journal Of Chemical Physics* **1999**, *111*, 6955-6964.

(36) Erwin, M. M.; McBride, J.; Kadavanich, A. V.; Rosenthal, S. J. *Thin Solid Films* **2002**, *409*, 198-205.

(37) McBride, J. R.; Kippeny, T. C.; Pennycook, S. J.; Rosenthal, S. J. *Nano Letters* **2004**, *4*, 1279-1283.

(38) Nellist, P. D.; Chisholm, M. F.; Dellby, N.; Krivanek, O. L.; Murfitt, M. F.; Szilagyi, Z. S.; Lupini, A. R.; Borisevich, A.; Sides, W. H.; Pennycook, S. J. *Science* **2004**, *305*, 1741-1741.

(39) McBride, J. R., Vanderbilt University, 2005.

(40) McBride, J.; Treadway, J.; Feldman, L. C.; Pennycook, S. J.; Rosenthal, S. J. *Nano Letters* **2006**, *6*, 1496-1501.

(41) Rosenthal, S. J.; McBride, J.; Pennycook, S. J.; Feldman, L. C. *Surface Science Reports* **2007**, *62*, 111-157.

(42) Goh, C.; Coakley, K. M.; McGehee, M. D. *Nano Letters* **2005**, *5*, 1545-1549.

(43) Kresge, C. T.; Leonowicz, M. E.; Roth, W. J.; Vartuli, J. C.; Beck, J. S. *Nature* **1992**, *359*, 710-712.

(44) Beck, J. S.; Vartuli, J. C.; Roth, W. J.; Leonowicz, M. E.; Kresge, C. T.; Schmitt, K. D.; Chu, C. T. W.; Olson, D. H.; Sheppard, E. W.; McCullen, S. B.; Higgins, J. B.; Schlenker, J. L. *Journal Of The American Chemical Society* **1992**, *114*, 10834-10843.

(45) Yang, P. D.; Zhao, D. Y.; Margolese, D. I.; Chmelka, B. F.; Stucky, G. D. *Nature* **1998**, *396*, 152-155.

(46) Alberius, P. C. A.; Frindell, K. L.; Hayward, R. C.; Kramer, E. J.; Stucky, G. D.; Chmelka, B. F. *Chemistry Of Materials* **2002**, *14*, 3284-3294.

(47) Choi, S. Y.; Mamak, M.; Speakman, S.; Chopra, N.; Ozin, G. A. *Small* **2005**, *1*, 226-232.

(48) Bosc, F.; Ayral, A.; Albouy, P. A.; Datas, L.; Guizard, C. *Chemistry of Materials* **2004**, *16*, 2208-2214.

(49) Crepaldi, E. L.; Soler-Illia, G. J. D. A.; Grosso, D.; Sanchez, M. *New Journal of Chemistry* **2003**, *27*, 9-13.

(50) Li, D. L.; Zhou, H. S.; Hibino, M.; Honma, I. *Journal Of Materials Research* **2003**, *18*, 2743-2746.

(51) Choi, S. Y.; Mamak, M.; Coombs, N.; Chopra, N.; Ozin, G. A. *Advanced Functional Materials* **2004**, *14*, 335-344.

(52) Li, D. L.; Zhou, H. S.; Honma, I. *Nature Materials* **2004**, *3*, 65-72.

(53) Coakley, K. M.; Liu, Y. X.; Goh, C.; McGehee, M. D. *Mrs Bulletin* **2005**, *30*, 37-40.

(54) Coakley, K. M.; Liu, Y. X.; McGehee, M. D.; Frindell, K. L.; Stucky, G. D. *Advanced Functional Materials* **2003**, *13*, 301-306.

(55) Bartl, M. H.; Puls, S. P.; Tang, J.; Lichtenegger, H. C.; Stucky, G. D. *Angewandte Chemie-International Edition* **2004**, *43*, 3037-3040.

(56) Coakley, K. M.; McGehee, M. D. *Chemistry Of Materials* **2004**, *16*, 4533-4542.

(57) Guo, Y. G.; Hu, J. S.; Liang, H. P.; Wan, L. J.; Bai, C. L. *Advanced Functional Materials* **2005**, *15*, 196-202.

(58) Hsu, M. C.; Leu, I. C.; Sun, Y. M.; Hon, M. H. *Journal Of Crystal Growth* **2005**, *285*, 642-648.

(59) Wang, H.; Yip, C. T.; Cheung, K. Y.; Djurisic, A. B.; Xie, M. H.; Leung, Y. H.; Chan, W. K. *Applied Physics Letters* **2006**, *89*.

(60) Kang, S. H.; Kim, J. Y.; Kim, Y.; Kim, H. S.; Sung, Y. E. *Journal Of Physical Chemistry C* **2007**, *111*, 9614-9623.

(61) Zhu, K.; Neale, N. R.; Miedaner, A.; Frank, A. J. *Nano Letters* **2007**, *7*, 69-74.

(62) Zhu, K.; Vinzant, T. B.; Neale, N. R.; Frank, A. J. *Nano Letters* **2007**, *7*, 3739-3746.

(63) Paulose, M.; Shankar, K.; Yoriya, S.; Prakasam, H. E.; Varghese, O. K.; Mor, G. K.; Latempa, T. A.; Fitzgerald, A.; Grimes, C. A. *J. Phys. Chem. B* **2006**.

(64) Paulose, M.; Shankar, K.; Varghese, O. K.; Mor, G. K.; Grimes, C. A. *Journal of Physics D-Applied Physics* **2006**, *39*, 2498-2503.

(65) Paulose, M.; Shankar, K.; Varghese, O. K.; Mor, G. K.; Hardin, B.; Grimes, C. A. *Nanotechnology* **2006**, *17*, 1446-1448.

(66) Varghese, C. K.; Paulose, M.; Shankar, K.; Mor, G. K.; Grimes, C. A. *Journal of Nanoscience and Nanotechnology* **2005**, *5*, 1158-1165.

(67) Chen, S. G.; Paulose, M.; Ruan, C.; Mor, G. K.; Varghese, O. K.; Kouzoudis, D.; Grimes, C. A. *Journal of Photochemistry and Photobiology a-Chemistry* **2006**, *177*, 177-184.

(68) Williams, D. B.; Carter, C. B. *Transmission Electron Microscopy*; Plenum Press: New York, 1996.

(69) Santiago, R.; Rendon, L.; Reza-San German, C.; Pal, U. *Journal Of Nanoscience And Nanotechnology* **2005**, *5*, 1172-1176.

(70) Klie, R. F.; Zhu, Y. *Micron* **2005**, *36*, 219-231.

(71) Yu, Z. H.; Guo, L.; Du, H.; Krauss, T.; Silcox, J. *Nano Letters* **2005**, *5*, 565-570.

(72) Kadavanich, A. V.; Kippeny, T. C.; Erwin, M. M.; Pennycook, S. J.; Rosenthal, S. J. *Journal Of Physical Chemistry B* **2001**, *105*, 361-369.

(73) Erwin, M. M.; Kadavanich, A. V.; McBride, J.; Kippeny, T.; Pennycook, S.; Rosenthal, S. J. *European Physical Journal D* **2001**, *16*, 275-277.

(74) Pennycook, S. J.; Jesson, D. E. *Acta Metallurgica Et Materialia* **1992**, *40*, S149-S159.

(75) Lupini, A. R., personal communication.

(76) Nellist, P. D.; Pennycook, S. J. *Science* **1996**, *274*, 413-415.

(77) Krivanek, O. L.; Nellist, P. D.; Dellby, N.; Murfitt, M. F.; Szilagyi, Z. *Ultramicroscopy* **2003**, *96*, 229-237.

(78) Krivanek, O. L.; Dellby, N.; Lupini, A. R. *Ultramicroscopy* **1999**, *78*, 1-11.

(79) Haider, M.; Uhlemann, S.; Zach, J. *Ultramicroscopy* **2000**, *81*, 163-175.

(80) Haider, M.; Muller, H.; Uhlemann, S.; Zach, J.; Loebau, U.; Hoeschen, R. *Ultramicroscopy* **2008**, *108*, 167-178.

(81) Krivanek, O. L.; Corbin, G. J.; Dellby, N.; Elston, B. F.; Keyse, R. J.; Murfitt, M. F.; Own, C. S.; Szilagyi, Z. S.; Woodruff, J. W. *Ultramicroscopy* **2008**, *108*, 179-195.

(82) Shao, Z.; Beck, V.; Crewe, A. V. *Journal Of Applied Physics* **1988**, *64*, 1646-1651.

(83) Dellby, N.; Krivanek, O. L.; Nellist, P. D.; Batson, P. E.; Lupini, A. R. *Journal Of Electron Microscopy* **2001**, *50*, 177-185.

(84) Nellist, P. D.; Dellby, N.; Krivanek, O. L.; Murfitt, M. F.; Szilagyi, Z.; Lupini, A. R.; Pennycook, S. J. *Electron Microscopy And Analysis 2003* **2004**, 159-164.

(85) Rose, H. *Optik* **1990**, *84*, 91-107.

(86) Muller, H.; Uhlemann, S.; Hartel, P.; Haider, M. *Microscopy And Microanalysis* **2006**, *12*, 442-455.

(87) Borchert, H.; Shevchenko, E. V.; Robert, A.; Mekis, I.; Kornowski, A.; Grubel, G.; Weller, H. *Langmuir* **2005**, *21*, 1931-1936.

(88) Swafford, L. A., Vanderbilt University, 2006.

(89) Masuda, H.; Yamada, H.; Satoh, M.; Asoh, H.; Nakao, M.; Tamamura, T. *Applied Physics Letters* **1997**, *71*, 2770-2772.

(90) Masuda, H.; Fukuda, K. *Science* **1995**, *268*, 1466-1468.

(91) Masuda, H.; Satoh, M. *Japanese Journal Of Applied Physics Part 2-Letters* **1996**, *35*, L126-L129.

(92) Yun, H. S.; Miyazawa, K.; Honma, I.; Zhou, H. S.; Kuwabara, M. *Materials Science & Engineering C-Biomimetic And Supramolecular Systems* **2003**, *23*, 487-494.

(93) Arslan, I.; Browning, N. D. *Microscopy Research and Technique* **2006**, *69*, 330-342.

(94) Smith, N., personal communication.

(95) Bowers, M. J.; McBride, J. R.; Rosenthal, S. J. *Journal Of The American Chemical Society* **2005**, *127*, 15378-15379.

(96) Schreuder, M. A.; Gosnell, J. D.; Smith, N. J.; Warnement, M. R.; Weiss, S. M.; Rosenthal, S. J. *Journal of Materials Chemistry* **2008**, *18*, 970-975.

(97) Kasuya, A.; Sivamohan, R.; Barnakov, Y. A.; Dmitruk, I. M.; Nirasawa, T.; Romanyuk, V. R.; Kumar, V.; Mamykin, S. V.; Tohji, K.; Jeyadevan, B.; Shinoda, K.; Kudo, T.; Terasaki, O.; Liu, Z.; Belosludov, R. V.; Sundararajan, V.; Kawazoe, Y. *Nature Materials* **2004**, *3*, 99-102.

(98) Jose, R.; Zhanpeisov, N. U.; Fukumura, H.; Baba, Y.; Ishikawa, M. *Journal Of The American Chemical Society* **2006**, *128*, 629-636.

(99) Yu, W. W.; Qu, L. H.; Guo, W. Z.; Peng, X. G. *Chemistry Of Materials* **2003**, *15*, 2854-2860.

(100) Batson, P. E. *Nature* **1993**, *366*, 727-728.

(101) Browning, N. D.; Chisholm, M. F.; Pennycook, S. J. *Nature* **1993**, *366*, 143-146.

(102) Muller, D. A.; Tzou, Y.; Raj, R.; Silcox, J. *Nature* **1993**, *366*, 725-727.

(103) Egerton, R. F. *Electron Energy-Loss Spectroscopy in the Electron Microscope*; 2nd ed.; Plenum Press: New York, 1996.

(104) Klie, R. F.; Arslan, I.; Browning, N. D. *Journal of Electron Spectroscopy and Related Phenomena* **2005**, *143*, 105-115.

(105) Iddir, H.; Disko, M. M.; Ogut, S.; Browning, N. D. *Micron* **2005**, *36*, 233-241.

(106) Varela, M.; Lupini, A. R.; van Benthem, K.; Borisevich, A. Y.; Chisholm, M. F.; Shibata, N.; Abe, E.; Pennycook, S. J. *Annual Review of Materials Research* **2005**, *35*, 539-569.

(107) Prabhumirashi, P.; Dravid, V. P.; Lupini, A. R.; Chisholm, M. F.; Pennycook, S. J. *Applied Physics Letters* **2005**, *87*, -.

(108) Griffin, K. A.; Varela, M.; Pennycook, S. J.; Pakhomov, A. B.; Krishnan, K. M. *Journal of Applied Physics* **2006**, *99*, -.

(109) Sapra, S.; Nanda, J.; Pietryga, J. M.; Hollingsworth, J. A.; Sarma, D. D. *J. Phys. Chem. B* **2006**, *110*, 15244-15250.

(110) Davidson, S. M. *Journal Of Microscopy-Oxford* **1977**, *110*, 177-204.

(111) Holt, D. B.; Raza, B.; Wojcik, A. *Materials Science And Engineering B-Solid State Materials For Advanced Technology* **1996**, *42*, 14-23.

(112) Scheer, R.; Wilhelm, M.; Lewerenz, H. J.; Schock, H. W.; Stolt, L. *Solar Energy Materials And Solar Cells* **1997**, *49*, 299-309.

(113) Galloway, S. A.; Edwards, P. R.; Durose, K. *Solar Energy Materials And Solar Cells* **1999**, *57*, 61-74.

(114) Mazzer, M.; Grunbaum, E.; Barnham, K. W. J.; Barnes, J.; Griffin, P. R.; Holt, D. B.; Hutchison, J. L.; Norman, A. G.; David, J. P. R.; Roberts, J. S.; Grey, R. *Materials Science And Engineering B-Solid State Materials For Advanced Technology* **1996**, *42*, 43-51.

(115) Jesse, S.; Guillorn, M. A.; Ivanov, I. N.; Puretzky, A. A.; Howe, J. Y.; Britt, P. F.; Geohegan, D. B. *Applied Physics Letters* **2006**, *89*.